EÖTVÖS LORÁND UNIVERSITY

FACULTY OF SCIENCE

Geochemical investigation of geological formations from the perspective of hydrogen storage potential

by

Orsolya Gelencsér

Ph.D. thesis

Lithosphere Fluid Research Lab

Ph.D. program for Environmental Earth Sciences at the Doctoral School of Environmental Sciences

Head of the doctorate school: Tamás Turányi, D.Sc.

Program director: Zoltán Szalai, Ph.D.

Supervisors

Zsuzsanna Szabó-Krausz, Ph.D.
Research fellow, Lithosphere Fluid Research Lab, Institute of Geography and Earth Sciences, Eötvös Loránd University

György Falus, Ph.D.
Head of division, Directorate of Geology, Supervisory Authority for Regulatory Affairs Hungary

Consultants

Csaba Szabó, Ph.D.
Lithosphere Fluid Research Lab, Institute of Geography and Earth Sciences, Eötvös Loránd University

Dániel Breitner, Ph.D.
Green Ventures Ltd. Hungary

Attila Sulyok, Ph.D.
HUN-REN Centre for Energy Research, Hungarian Research Network

DOI: 10.15476/ELTE.2024.342

Budapest

Acknowledgements

I am thankful to the “big four” who have guided me through this PhD journey: To **György Falus**, whose open-minded attitude and extensive experience in rock-water-gas interaction has greatly enriched the quality of my work. To **Zsuzsanna Szabó-Krausz** for setting me on the path of geochemical modeling, lab management and paper writing. To **Dániel Breitner**, who brought the perspectives of economics and industry into my research, making outcomes more practical and applicable. And to **Csaba Szabó** for all his support in a wide sense. I am also thankful for the opportunity to learn the XPS method under the guidance of **Attila Sulyok,** whose contributions enriched both my academic journey and personal growth.

I am thankful to **László T. Mika** and **Csaba Árvai** for their indispensable help in experimental work and lab building. Many thanks to **Tibor Németh** for his assistance in XRD and for the fruitful discussions throughout my scientific career. My sincere thanks go to **Enikő Bali** for hosting me in Iceland and to **Guðmundur H. Guðfinnsson** for their help in EMPA measurements.

Thanks to my colleagues at O&GD Central Ltd. **Péter Tóth, Levente Szabó** and **Dave LeClair** for their practical advice during the research. I am thankful to **Andrea F. Marján** for her excellent administrative work, kindness and help during financial management of the PhD.

I am proud to be an **LRG** member where I experienced the cohesion which gave a lot of happy memories that brought us through all difficulties. Thanks to **Ákos Kővágó, Dóra Cseresznyés** and **Laura Horváth** for helping me in lab building maintenance and experimental work. Special thanks to my closest friends, Tejbegreizen group and girls from Badacsony for their all-round support.

Credit goes to my Family, who have been constantly supporting during my education.

This study was financially supported by:

- the PhD fellowship of Hungary (2020-2024);
- the O&GD Central Ltd. (2020-2024);
- Project no. 971238 has been implemented with the support provided by the Ministry of Culture and Innovation of Hungary from the National Research, Development and Innovation Fund, financed under the KDP-2020 funding scheme.
- Proof-of-Concept grant by the Innovation Centre of Eötvös Loránd University (2023);
- ÚNKP-21-3 New National Excellence Program of the Ministry for Innovation and Technology from the source of the National Research, Development and Innovation Fund. (2021);
- American Association of Petroleum Geologists Foundation Grants-in-Aid Program (2021).

Content

List of figures

List of tables

1. Introduction and goals

1.1. Role of hydrogen and its subsurface storage in the energy transition

Recent global challenges promote the birth of new technologies in various fields including environmental sciences. One of the greatest challenges is climate change which is a point of discussion among disciplines and generates considerable debate. The Sixth Assessment Report (Chen *et al.* 2021) of Intergovernmental Panel on Climate Change (IPCC) aims to assess the most recent scientific understanding of the climate system and climate change. It states that the scale of recent changes across the climate system is unprecedented and that human influence on the warming of atmosphere, ocean and land is unequivocal. Another challenge is the continuously increasing global energy demand due to population growth and economic development. World energy consumption rebounded by 5% after the COVID-19 pandemic due to the economic recovery and further growth of energy demand is foreseen for the next decades (Chanthakett *et al.* 2023). These global challenges are pressing the development and implementation of new sustainable technologies.

Transformation of the global energy sector from fossil-based to renewable energy sources is generally called the energy transition, a process that is shaping the beginning of the 21st century. Reducing industrial CO_2 emission to mitigate climate change requires drastic structural changes across various industrial sectors. In contrast with conventional hydrocarbon-based energy production the major renewable energy production is intermittent since its vast majority comes from solar and wind sources (Simon *et al.* 2015). The current technical and organizational structures of the power supply systems are not suitable to fully cope with large amount of renewable energy, with its portion is continuously growing (Guo *et al.* 2023). The power-to-gas technology, which converts surplus electrical energy into gas storage, is one of the available methods aimed to balance the gap between production and consumption (Lehner *et al.* 2014), hence the infrastructure development combined with innovative energy storage methods bring a new era in technological innovations.

The first attempt to store energy in the subsurface dates back to 1915, a partially depleted gas field served as natural gas storage site in Ontario Canada (Foh *et al.* 1979). Since this pioneer attempt, geological storage is extensively used in oil, natural gas and compressed air industries (Lord *et al.* 2014). The expansion of gas-fired electricity generation has made high-deliverability storage

facilities more valuable. Today, underground gas storage plays strategic role for seasonal and peak-shaving purposes. It is a sizable financial asset ensuring continuity of delivery in case of disruption in supply chain (Lord *et al.* 2014). This demonstrates that storing energy (carriers) underground is substantial for efficient resource management and energy security.

The first mention of hydrogen in large-scale economical aspect can be traced back to 1973, when the oil crisis enhanced the search for an alternative energy source such as hydrogen produced from coal or nuclear-produced electricity. However later the oil prices moderated and the intentions waned (IEA 2019). Recently, the main interest in hydrogen-based economy originates from the worldwide concern about climate change that manifested in policy actions aimed to decrease the use of fossil fuels. The future energy system of this concept is planned to be based on hydrogen (or at least it can be a significant part of the energy mix), because it can play significant role in power storage (of renewables), with strengthening importance due to development of renewable energy sources, hard-to-decarbonize industries (steel, fertilizers, high value chemicals), heavy duty transportation (marine and aviation) and generation, and even in building heating (Cihlar *et al.* 2021). In brief, hydrogen is a potential energy vector which could play a central role in future energy systems (Pfeiffer and Bauer 2015). Within this context, the European Union, including Hungary, faces a pivotal moment in reshaping its energy system to drive the transition toward sustainable and circular economy. The conversion of excess renewable electricity to hydrogen and its seasonal storage in the subsurface is widely recognized as the most promising solution to optimize and decarbonize the energy system (Figure 1) (Heinemann *et al.* 2021; Miocic *et al.* 2022).

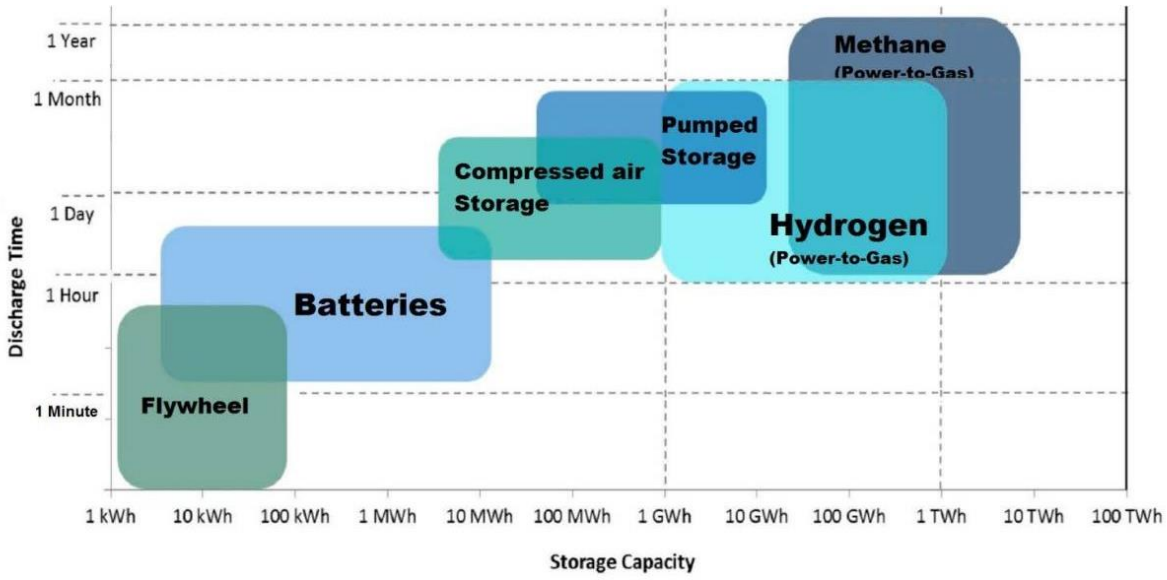

Figure 1. *Energy storage practices in function of storage capacity and discharge time. Source: The Case for Hydrogen. White Paper, 2015*

Therefore, the role of geologic formations in the energy transition is unequivocal, since they are the storage objects for both methane and hydrogen. Despite the 'low-carbon' energy policies in place, it is expected that natural gas will continue to play an important role in the energy mix, due to lower CO_2 emissions with respect to other fossil fuels as well as decades of experience in underground storage. That is why the dynamics of transition from natural gas storage to hydrogen storage is not clear. The report of Frontier Economics (2024) predicts that the duality between natural gas and hydrogen storage may persist for several years in order to sustain high levels of (energy) security.

Growing tendency can be seen worldwide in solar energy share of the energy mix along with wind energy. For example, in the last 4 years, the solar energy production in Hungary has tripled from 2 GWh to 6 GWh and significant further growth (up to 12 GWh) is expected to 2030 (NECP 2023). Despite these remarkable advancements of supply side (Figure 2), the world economy lacks large-scale hydrogen storage facilities, yet growing capacity would be desirable to ensuring the safe, economical, and reliable operation of extensive hydrogen production assets and meeting the demands of industrial customers (Cihlar *et al.* 2021).

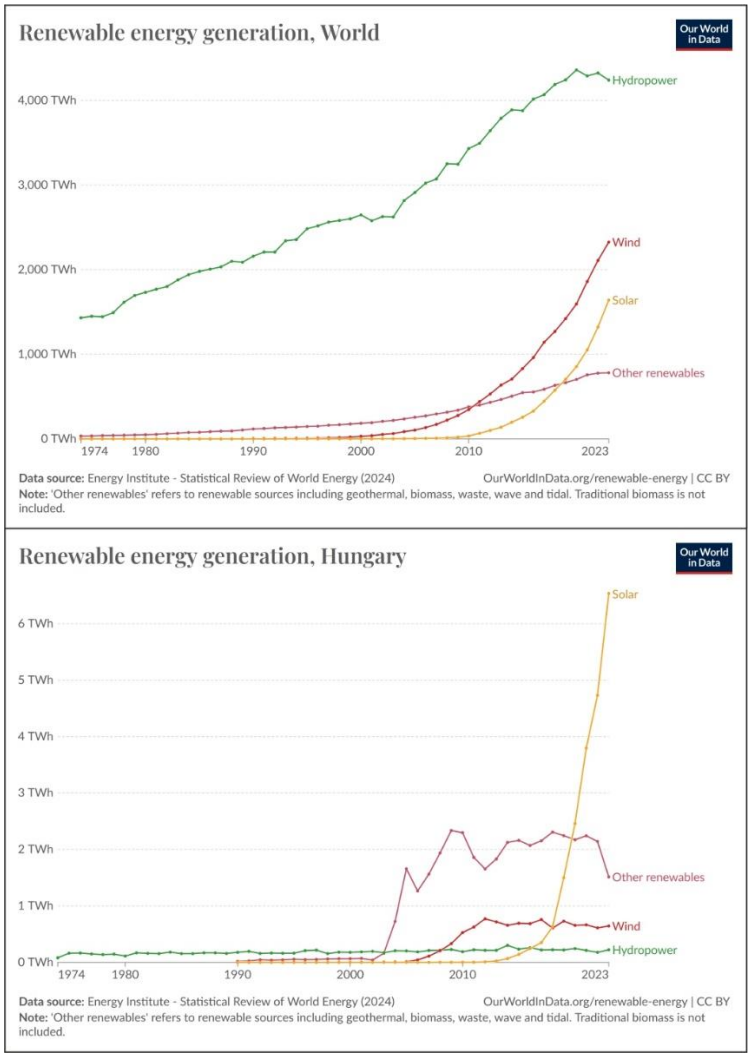

Figure 2. *Renewable energy generation through the time worldwide (top) and in Hungary (bottom). Data source: Energy Institute – Statistical Review of World Energy (2024) (ourworldindata.org/renewable-energy)*

The European Union is committed to expanding the underground storage capacities as a mean to reinforce system flexibility (COM(2023) 182). The first step will be the increase of natural gas storage capacity, and the long-term goal includes deployment of the large-scale underground hydrogen storage converted from excess renewable electricity (Miocic *et al.* 2022). Although, only a few European countries are currently resilient to short-term disruptions in natural gas supply (e.g., political conflicts, natural disasters) due to their gas storage capacity (Miocic *et al.* 2022), the majority lack sufficient storage capacity to meet the high consumption demands for heating

during winter. Hungary belongs to the more resilient countries as it has significant natural gas storage capacity and developed supply infrastructure. The National Hydrogen Strategy of Hungary stated that the achievement of the energy and climate goals of the EU is highly supported and improvements in seasonal (large-scale) energy storage is among the key elements of the strategy (Hungary's National Hydorgen Strategy, 2021).

The potential geological storage formations are the depleted gas reservoirs, rock salt formations and saline aquifers (Carden and Paterson 1979; Ozarslan 2012; Tarkowski 2017). Taking a closer view at our region, the Hungarian part of the Pannonian basin is a petroleum province with thick (3-6 km) infill of Neogene sediments, and its stratigraphic features indicate potential in subsurface gas storage (Király *et al.* 2010). Several natural gas storage sites already exist in depleted gas reservoirs which are hosted in porous sandstone. Beside siliciclastic sedimentary rocks, Transylvanian basin, the easternmost subbasin of the Pannonian basin, is characterized by significant rock salt occurrences, and it is the nearest significant halite dominated evaporite formation to Hungary. Salt mining in Transylvanian basin has a long history as this formation played a key role for centuries as a source of raw material (e.g., Draskóczy 2014). Diapir structures of rock salt with thicknesses spanning several kilometers, offer significant potential for cavern storage. Therefore, these salt formations should be considered as promising research objects from the aspect of hydrogen storage.

1.2. Hydrogen storage in subsurface

The underground storage sites are inherently bound to geological formations having a consistent set of physical characteristics. Although site selection methods are still immature due to the complexity and immature nature of the technology, there are guiding principles such as injection and withdrawal rates. Underground hydrogen storage (UHS) is planned to be used for two main purposes: 1/ for base load storage which involves withdrawal once or twice a year, and 2/ peak load storage, where withdrawal occurs many times over a short period to meet short-term demand. Peak load demands are typically met by salt caverns, mining caverns, whereas base load demands are met by depleted oil/gas reservoirs (Zivar *et al.* 2021; Thiyagarajan *et al.* 2022). In this chapter, the storage types are elaborated upon their geological characteristics. Other important aspects, however, are beyond the scope of this research, such as technological, environmental, legal and economic considerations.

1.2.1. Depleted natural gas fields

The repurposing of depleted hydrocarbon reservoirs has been in the mind of oil and gas industry for long time and several successful implementations took place for natural gas storage and more recently for carbon capture and storage (CCS) (Shahriar *et al.* 2024). Among the hydrocarbon reservoirs, depleted oil reservoirs are considered less favorable for UHS compared to the *depleted gas fields* (DGF), due to the elevated risks of the undesirable processes, such as the mixing of hydrogen with residual hydrocarbons due to the higher solubility of H_2 with oil and higher chemical and biological reactivity (Emmel *et al.* 2023). Additionally, DGF for UHS is more advantageous in contrast to an unexploited or undisturbed geological formation, since the reservoir is a proven geological trap consisting of a porous rock and having particular petrophysical properties of the reservoir rock (i.e. porosity, permeability) important for reasonable gas injectivity and withdrawal (Carden and Paterson 1979; Foh *et al.* 1979; Heinemann *et al.* 2018). The DGF reservoirs are predominantly composed of siliciclastic sedimentary rocks, such as sandstone, and have considerable depth allowing to keep a particular reservoir pressure which usually falls between 30 and 380 bar (Cavanagh *et al.* 2023). For buoyant fluids to be trapped within a reservoir, it is required to be overlain by a low-permeability and non-fractured caprock which keeps the H_2 in the reservoir and does not allow the gas to migrate beyond its limits (Hibbard and Gilfillan 2024). Examples are traps bounded by unconformities, facies change, anticlines and faults (Gunter *et al.* 2004).

The DGFs are considered as having the largest energy storage capacity in the European strategies e.g., 1000 TWh that is attributed to porous reservoirs in Europe by the Hydrogen Underground Storage in Porous Reservoirs (HyUSPRe) project (Cavanagh *et al.* 2023). The long-term repurposing of DGF infrastructure may be an economically more efficient and quicker solution compared to the building of solely new hydrogen dedicated infrastructure. DGFs have the advantage that surface and subsurface facilities developed for gas exploitation can further be repurposed, and the cushion gas necessity is usually less in depleted gas fields (Kanaani *et al.* 2022) compared to other storage options, i.e., saline aquifers. Their adaptation to the needs of underground hydrogen storage allows costs to be reduced. Further testing of safety under real operational conditions would promote quicker public acceptance while the development of innovative retrofitting solutions would make repurposing even more economically viable.

Nevertheless, certain geological criteria should be met for depleted hydrocarbon reservoir to maintain recovery efficiency. For instance, the rock-forming minerals should be chemically insensitive to high-pressure hydrogen (Carden and Paterson 1979; Yekta *et al.* 2018). Above all, a comprehensive evaluation of all processes involved in the conversion is outmost importance. This should cover both geological and technical aspects, including factors related to wells (such as casing types, and the steel and cement used), surface installations, and other relevant components (Tarkowski 2019).

However, on a commercial scale there is still very limited knowledge and experience converting DGF to UHS. Examples of recent pioneer field-scale UHS projects include one by the Austrian company RAG Ltd., (Bauer 2017) and one commencing this year in Hungary (Akvamarin project) (Farkas *et al.* 2024), but these projects are far from the real-life applications. Similar level of development of underground hydrogen storage can be observed in other continents (Cavanagh *et al.* 2023).

1.2.2. Salt caverns

Rock salt is a promising candidate for UHS due to its extremely low porosity (<0.5%) (Lowenstein and Spencer 1990; De Las Cuevas 1997; Ghanbarzadeh *et al.* 2015), permeability (< 10^{-21} m^2) (Peach and Spiers 1996) and chemical inertia towards hydrogen (Carden and Paterson 1979; Caglayan *et al.* 2020). This rock type is made up of a suite of minerals (e.g., halite, gypsum, anhydrite) formed from the evaporation of seawater (Schreiber and El Tabakh 2000). The extraction of salt by either classical mining procedures or water leaching to create caverns is a regularly used technique (Allen *et al.* 1982). This existing knowledge can be easily transferred to the case of hydrogen storage due to the similarities in cavern design, construction and operation (Ozarslan 2012). Gas storage in salt caverns has the advantage that short-term fluctuations in gas consumption can be fulfilled compared to porous rock reservoirs, as they enable a high rate of gas injection and withdrawal, up to 10-12 cycles a year (Lankof and Tarkowski 2020). Therefore, this geological storage type is the most acceptable alternative for storing peak gas reserves (Tarkowski 2019).

Salt caverns have been used for high-purity hydrogen storage by the chemical industry in the UK since the 1970's (Teesside) and in the US since the 1980's (US Gulf Coast and The Chevron

Phillips Clemens Terminal, Texas), as well as in Yakshunovskoe, Russia (Panfilov 2010; Crotogino *et al.* 2018; Dopffel *et al.* 2021).

The technical construction of salt caverns depends on several factors, such as, type of salt deposit (bedded or domal) (Lankof and Tarkowski 2020), depth of the designed cavern, mineralogy of the rock salt and technology of mining process (Cyran 2020; Małachowska *et al.* 2022). The general criteria of underground energy storage for salt domes, exploited by water leaching, were summarized by Allen et al. (1982): 1) structurally competent salt at a proper depth with sufficient thickness, and without excess of interbedded insoluble materials, 2) adequate supply of fresh water for leaching the salt, and 3) economically and environmentally acceptable means for brine disposal.

Understanding the rheology of rock salt during long-term deformation is of great significance in salt engineering, designing, operation, and abandonment of underground storage caverns (Adamuszek *et al.* 2021). Rock salt deforms by creep and cavities in the formation can decline over time (Kruck *et al.* 2013). The stability of a cavern can be ensured by preliminary microstructural study and years of experience. Linear creep laws account for pressure solution and have been applied and tuned in numerical simulations of cavern convergence and subsidence (Breunese *et al.* 2003).

A disadvantage of this storage type on one hand is its availability; evaporite formations are rare around the world compared to porous rock reservoirs (Figure 3) (Zivar *et al.* 2021). Although the halite (NaCl), a typical evaporite mineral, is generally considered as a nonsensitive mineral to hydrogen, other evaporite minerals, such as anhydrite ($CaSO_4$) could be involved in reactions that can potentially result in generation of H_2S (Hemme and van Berk 2017; Flesch *et al.* 2018). The experimental study of Felsch *et al.* (2018) also demonstrated that anhydrite occurring in the polymineralic Triassic and Permian sandstones, can dissolve after H_2 treatment.

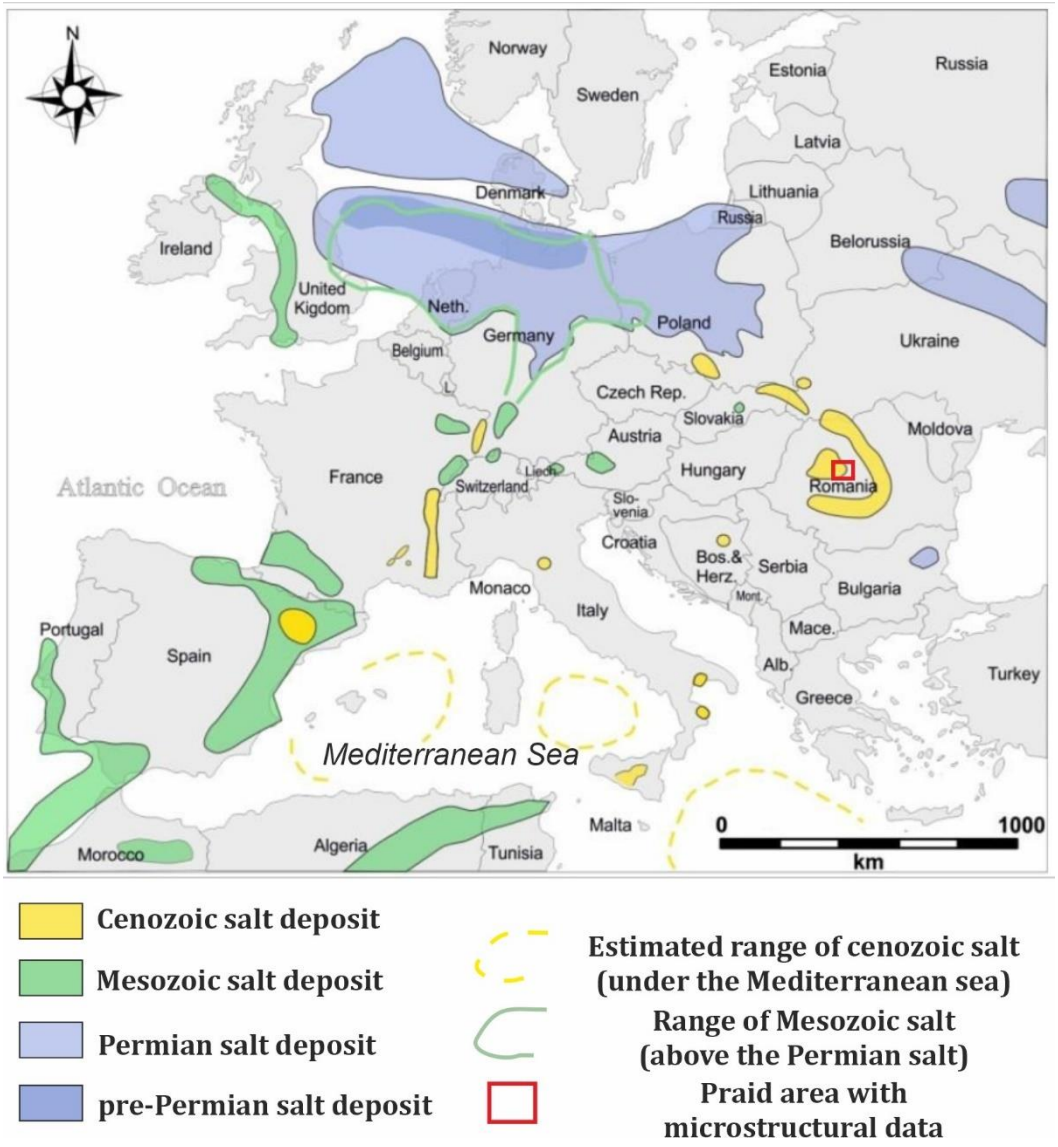

Figure 3. *Location of evaporite deposits with their ages around Europe. Praid area (Romania) is highlighted within red box. Map modified after Gillhaus and Horváth (2008) and Kruck et al. (2013)*

1.2.3. Saline aquifers and other storage types

Saline aquifers are usually situated in porous rocks overlain by less permeable caprock(s) (mudstone or evaporite), thus they have share many features with hydrocarbon reservoirs. A notable characteristic of saline aquifers is that the formation brine is not suitable for drinking water. Besides the high dissolved ion content, they may contain gases (CH_4, CO_2) as well. Beynes (France) is an example for aquifer gas storage where town gas was stored, but hydrogen storage in

saline aquifers is far less understood than storage in depleted reservoirs of hydrocarbon fields since they are generally poorly studied (Table 1). *Engineered rock caverns* are planned to be realized in hard, tight and stable rock formations (Crotogino *et al.* 2018; Matos *et al.* 2019). Another option for hydrogen storage can be the reutilization of *abandoned mine shafts*. These latter two options should be considered particularly in areas where other storage options are limited by geological factors (Masoudi *et al.* 2024). However, several additional technical questions can arise with the use of engineered barriers, such as cement, resin or other materials as their relationship with high-pressure hydrogen has not been thoroughly investigated (Miocic *et al.* 2023).

Table 1. Operating underground storage sites of hydrogen (with bold) and natural gas/hydrogen mixtures and their properties grouped by their rock type. Compiled from (Ebrahimiyekta 2017; Miocic *et al.* 2023; Hematpur *et al.* 2023).

Rock type	Name	Since (year)	Country	Depth (m)	Volume (m^3)	Operating conditions (bar)	H_2 (%)	T (°C)	Microbial activity reported
salt caverns	**Teesside** (ICI)	1972	UK	400	7×10^4	45	95	27	no
	Clemens (ConocoPhillips)	1983	USA	1000	5.8×10^5	70-137	95	-	no
	Moss Bluff (Praxair)	2007	USA	822	5.7×10^5	55-152	95	-	no
	Spindletop (Air Liquide)	2017	USA	1340	9.1×10^5	68-202	95	-	no
depleted gas fields	Kiel	1971	Germany	1330	3.2×10^4	80-100	62	-	no
	Bad Lauchstädt (Uniper)	2025	Germany	820	5×10^7	150	95	-	
	Etrez - STOPIL-H2	2010	France	-	5.7×10^5	60-240	-	-	no
	Lehen-002	2017	Austria	1022	1.2×10^5	30-78	10	40	
	HyChico (Diadema)	2010-2018	Argentina	815	7.5×10^5	26.5	10	50	yes
	Yakshunovskoe Field		Russia	-					
saline aquifer	Beynes	1956-1972	France	430	3.3×10^8	-	50	-	yes
	Ketzin	1964	Germany	250		-	62	35	yes
	Kasimov	-	Russia		1.8×10^6	-			
	Lobodice	1989	Czech Republic	450	1×10^8	90	54	35	yes

1.3. Geochemical reactions as one of the major concerns about underground hydrogen storage

The utilization of geological formations should always be considered in geochemical context. Geologic formations potentially considered for UHS usually contain several mineral phases, saline water, and residual gas, which makes the system highly complex, even without considering the effect of biological activity at lower temperature (under 100 °C) (Dopffel *et al.* 2021). Among the geological uncertainties of UHS in sandstones, the understanding of rock-water and hydrogen interactions is particularly important. A part of the injected H_2 is expected to dissolve into the pore fluid thus changing the thermodynamic equilibrium conditions in the pore space (Hashemi *et al.* 2021). The dissolution of minerals into pore water can lead to an increase in the porosity of the rock matrix, but at the simultaneously, new minerals can precipitate that can also clog the pores and have additional negative consequences for the permeability of the rock (Amid *et al.* 2016). Overall, the porosity and permeability values of the reservoirs are important parameters which should be preserved to appropriately design a hydrogen storage system (Hashemi *et al.* 2021). Siliciclastic sedimentary rocks predominantly consist of silicates, namely quartz, feldspars and clay minerals. Among the silicate minerals, K-feldspar could be more sensitive to pH changes (e.g., (Yuan *et al.* 2019) and its dissolution could result in precipitation of secondary mineral phases (Zhu and Lu 2009). Carbonate minerals (e.g., calcite, dolomite) often act as cementing agents or occur as grains (even as fossils) in these rocks in various amounts (Kantorowicz *et al.* 1987; McBride *et al.* 1995). Calcite is one of the main sources of carbonate anion (CO_3^{2-}) in porewater, which due to its buffering effect, usually governs the groundwater chemistry (Baumann *et al.* 1985). Pyrite (FeS_2) is a common accessory mineral in sedimentary environments (Hall 1986) and its redox sensitive behavior is well known from the literature. In the presence of hydrogen, pyrite can be reduced to pyrrhotite (FeS_x) and hydrogen sulfide (H_2S) can be formed (Truche *et al.* 2010) which is a major concern in the context of UHS.

Although a major component of the Earth's crust (e.g., McCollom and Bach 2009), hydrogen, and its effects on sedimentary rocks have not been thoroughly studied primarily due to technical issues (Zgonnik 2020). The understanding of geochemical interactions between hydrogen, pore water, and the rock forming minerals during UHS is a huge priority of applied geochemistry (Flesch *et al.* 2018; Yekta *et al.* 2018). Papers in this topic have multiplied in recent years and a significant part of these studies is based on geochemical modeling (Hassannayebi *et al.* 2019; Bo *et al.* 2021)

which is a cost effective and easy way to predict geochemical reactions in space and time. Although geochemical modeling has a long and successful history in solving environmental issues and CCS-related studies, in the context of UHS, geochemical modeling softwares (such as PHREEQC and TOUGHREACT) are highly unreliable when considering high-pressure hydrogen and could result inaccurate models (Gelencsér *et al.* 2023; Vialle and Wolff-Boenisch 2024). Therefore, experimental control combined with various analytical methods is strongly needed to address the geochemical effect of hydrogen on the geologic storage site in siliciclastic sedimentary systems.

1.4. Goals of the PhD project

This PhD work focuses on the geochemical aspects of UHS with particular regard to the Pannonian basin. In cooperation with the company O&GD Central Ltd., a producing, but soon to be depleted, gas reservoir was chosen for detailed study. Its reservoir rock is a widespread, characteristic Upper Miocene sandstone formation which could potentially become a major hydrogen storage formation in the Carpathian-Pannonian region.

The major objective of this study is to identify possible abiotic reactions in the rock-porewater-hydrogen system with the detailed investigation of mineral-hydrogen interaction and their extent in aqueous environment. The thesis covers the complex experimental and modeling study of three common rock-forming minerals of the studied sandstone, namely calcite, K-feldspar and pyrite (Figure 4). Additionally, the Middle Miocene evaporite formation of the Transylvanian basin was also investigated with respect to salt cavern mining and hydrogen storage perspective. In this case the existing petrographic and geochemical data were compared to the cavern mining criteria.

Since UHS is still not widespread on the world, there is no well-established method for the study to estimate hydrogen reactivity under subsurface storage conditions. The research started with the definition of a workflow to understand the behavior of the rock-forming minerals under high pressure hydrogen. Experiments with single mineral phases serve as starting points for understanding the complex rock-water-gas systems. Geochemical modeling was used along with experimental work to compare results. Both experiments and modeling work were supported by various analytical techniques. Besides the routinely used methods in Earth Science, such as (X-ray diffraction, scanning electron microscopy, inductively coupled plasma optical emission spectroscopy), X-ray photoelectron spectroscopy (XPS) was used for studying changes on mineral

surfaces during experiments. The latter one is a widely used technique by physical scientists since the 1980's but it is much less known in the wide geochemistry. However, this PhD research is also a demonstration of its effectiveness in the field of applied geochemistry.

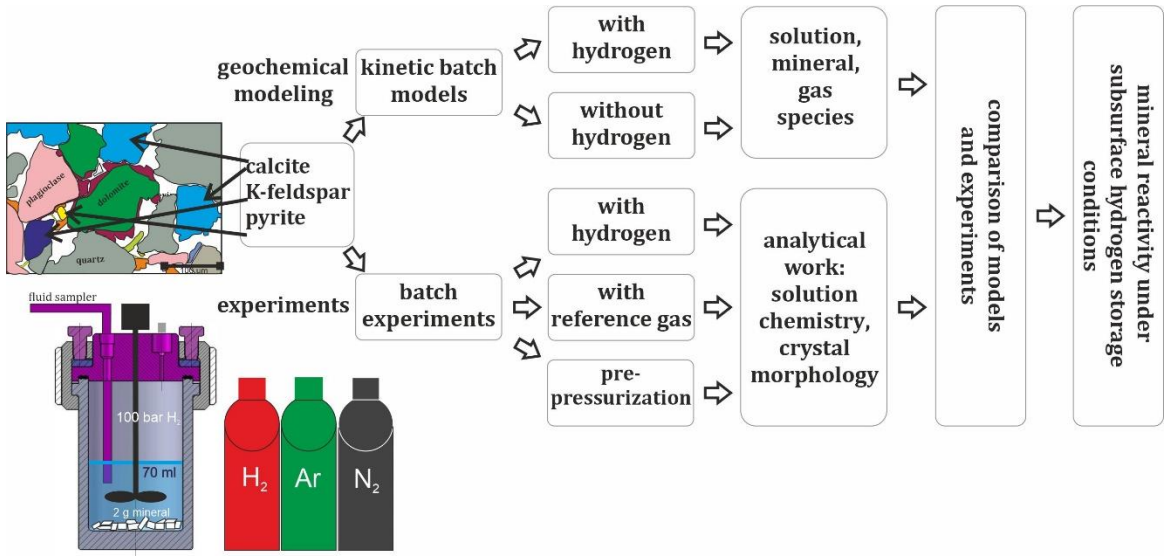

Figure 4*. The flowchart of the doctoral study. Rock-forming minerals were investigated with two different approaches. Laboratory experiments combined with geochemical modeling were used to understand mineral reactivity in aqueous environment under the pressure and temperature of underground hydrogen storage. Several analytical techniques were applied to detect changes in solid and liquid phases.*

2. Geological background

2.1. Pannonian basin evolution (central part)

The Pannonian basin (PB) system is located from Vienna basin (Central Europe) to the Carpathian Foredeep (Eastern Europe) and surrounded by mountain chains of the Alps-Carpathians-Dinarides. The basement of the PB is complex and originates from the Mesozoic Tethys and its closure (rise of Alpine-Carpathian orogen) (Sztanó *et al.* 2013).

As for the geodynamic considerations, the PB was formed during the Miocene when the roll-back of a subducting plate in the Carpathian embayment (Royden *et al.* 1982; Royden 1988, 1993) promoted stretching of a thickened orogenic area. The lateral motions of ALCAPA and Tisza-Dacia, mega units were accompanied with large-scale translations (Horváth *et al.* 2006b) and

rotations and reached 150-200 km (Ustaszewski *et al.* 2014; Balázs *et al.* 2018). This Early–Middle Miocene synrift extension caused lithosphere thinning and moderate subsidence because the feeding areas were located at a great distance (Tari *et al.* 2023). Then around 9 Ma, neotectonic inversion has become the dominant process (e.g., Horváth and Cloetingh 1996; Ruszkiczay-Rüdiger *et al.* 2020) driven by the northward motion and counterclockwise rotation of the Adriatic microplate, with respect to Eurasia (Porkoláb *et al.* 2023). The inversion was observed as basin-scale (50-100 km) uplift and erosion and local scale (5-20 km) inversion associated with late traps in basin fill via reactivation of preexisting normal faults. (Tari *et al.* 2023). As a consequence of thinned lithosphere, the elevated heat flow enhanced the maturation of Miocene source rocks of hydrocarbons (Badics and Vető 2012). During the post rift phase, rapid subsidence resulted in km thick basin fill successions (Juhász 1994).

The Early and Middle Miocene sediments of the PB started to accumulate when the Central-Paratethys Sea still had marine connections. Simultaneously with the formation of the basin system, the uplift of the surrounding mountain chains (first Alps, then later Carpathian arc) and their erosion provided a significant volume of sediments to fill up the basin system (Kuhlemann *et al.* 2001). By the time of the Sarmatian, sea connections had narrowed, and in addition to strong fluctuations in salinity (hypersaline and brackish) water conditions could develop (Rögl 1998) and the basin became an endorheic lacustrine system (Kázmér 1990; Sztanó *et al.* 2013), similar to modern Caspian Sea. During the Late Miocene and Early Pliocene, rivers (e.g., paleo Danube) dominantly from NW, N and NE continued the filling of the basin system with their sediments building a morphological shelf. As the shelf widened, the Lake Pannon filled up by turbidite lobes (Szolnok Formation), slope deposits (Algyő Formation) and stacked deltaic lobes (Újfalu Formation) (Sztanó *et al.* 2013), reflecting the transition from lacustrine to alluvial depositional settings and creating one of the thickest Neogene non-marine depositional sequences in Europe (Magyar *et al.* 2013). The subbasins are distinguished as Danube basin, Zala subbasin, Dráva subbasin, Makó trough, Békés basin, Jászság subbasin, Derecske trough (Figure 5).

As a conclusion, the majority of gas fields in the PB are associated with basement highs between the subbasins developed due to synrift extension. the Late Miocene siliciclastic sediments, particularly the turbiditic sandstones are characterized with high porosity and permeability, making them ideal reservoir rocks whereas slope deposits usually consist of silty, clayey marls with low porosity and permeability. Moreover, the overlying Újfalu Formation is mixed regarding

to the grainsize but a common feature is the presence of huminitic clay with low permeability (Saftić *et al.* 2003). The third essential part of the hydrocarbon plays are the structural traps which were usually generated by the above-mentioned postrift inversion (Tari *et al.* 2023).

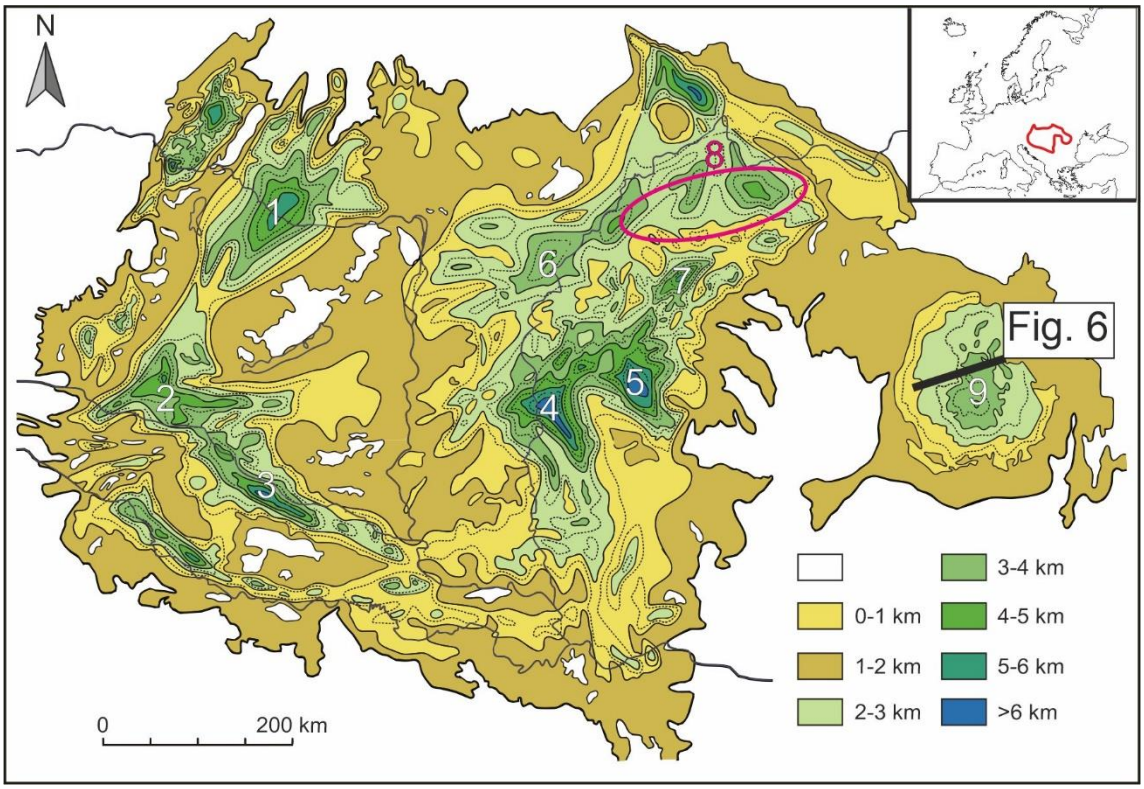

Figure 5. *Depth of pre-Neogene basement in the Pannonian Basin system (modified after Horváth and Royden 1981 and Kovács 2018). The deeper areas are subbasins with thick sedimentary infill: 1. Danube basin, 2. Zala subbasin, 3. Dráva subbasin, 4. Makó trough, 5. Békés basin, 6 Jászság subbasin, 7. Derecske trough, 8. Nyírség area with buried volcanic structures, 9. Transylvanian basin. The black line indicates cross section in Figure 6.*

2.2. Transylvanian basin

The Transylvanian basin (TB), the easternmost subbasin of PB system is bordered by the Apuseni Mts. from the west, the Eastern Carpathians from north and east and the Southern Carpathians from south. The basement of the Transylvanian basin formed as a result of suturing of Tisza and Dacia tectonic blocks during the Cretaceous (e.g., Csontos *et al.* 1992; Schmid *et al.* 2008). The TB started to fill up from the late Cretaceous and its deposition history is strongly related to the

evolution of the bordering Carpathian orogen (Krézsek and Filipescu 2005). The most significant differences from the broader PB area are the followings: the greater thickness of the continental lithosphere (Szafián *et al.* 1999), the lower heat flux (45 mW/m^2) (Lenkey *et al.* 2001), and the lack of extensional structures starting from the Miocene (Krézsek and Filipescu 2005; Krézsek and Bally 2006; Tiliță *et al.* 2018) in the TB. The differences are also observed in the sedimentary record. In the Middle Miocene (Badenian), unlike in the PB, significant amount of evaporite (original thickness is interpreted to be up to 300 m) deposited in the Transylvanian basin (Figure 3) due to the restricted connection to the rest of the Central Paratethys sea (Rögl 1998; Krézsek and Filipescu 2005; Peryt 2006). The evaporites consist of gypsum on the basin margins (Ghergari *et al.* 1991), and halite interbedded with thin shales (Krézsek *et al.* 2010) in the basin center. Noteworthy to mention that there are some boreholes transecting evaporites (mainly sulfates) in the PB as well (e.g., Báldi *et al.* 2017) however, they do not have sufficient thickness for hydrogen storage consideration.

The basin inversion in the late Miocene resulted in general uplift of the Transylvanian basin (Krézsek and Bally 2006; Tiliță *et al.* 2015) accompanied with massive deformation. The basin evolution and its subsequent inversion was roughly coeval with onset of back-arc calk-alkaline volcanism (Mason *et al.* 1998). Due to the post-salt tectonic activity the evaporite body is strongly deformed and crops out at the basin margins (Szakács and Krézsek 2006). Salt structures (diapirs) follow two lineaments and form two diapiric alignments near the eastern and western edges of the Transylvanian basin, respectively (Figure) (Krézsek and Bally 2006; Bukowski 2013).

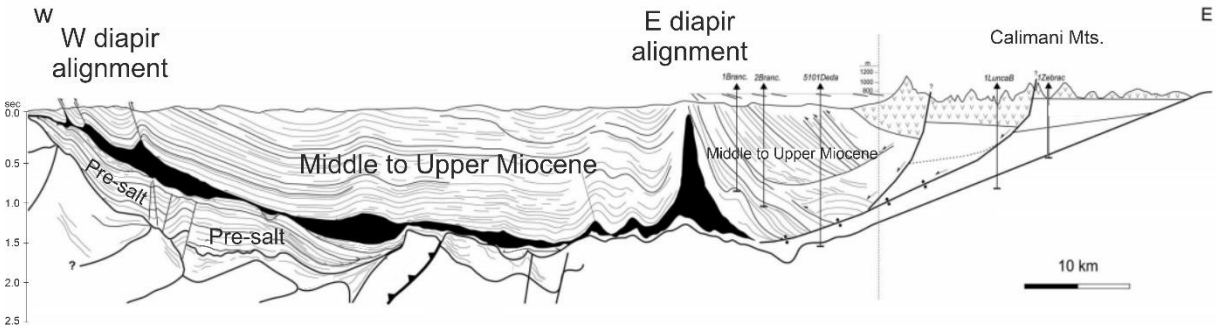

Figure 6. *Seismic interpretation of a W-E section of the Transylvanian basin (TB). For the location, refer to Figure. 5. Black body represents the situation of the middle Miocene (Badenian) rock salt. The western and eastern diapir alignments appearing along the basin margins are indicated on the section. Figure modified after Krézsek and Bally (2006).*

3. Samples and sample preparation

3.1. Öcsöd site parameters and selected core samples and cuttings in the Pannonian basin

The study area is located near Öcsöd village between the Kunság basin and Öcsöd–Martfű structural height (Figure 7), a recently subsiding sub-basin of the Great Hungarian Plain (Southeast Hungary). Samples originate from two wells, namely from Öcsöd-1 and OGD-Öcsöd-K-2, and they were collected with the support of O&GD Central Ltd.

Öcsöd-1 was drilled in 1974 by the Hungarian Oil and Gas Trust (OKGT) with the aim of tectonic exploration of the basement. The OGD-Öcsöd-K-2 was drilled in 2015 to test an amplitude anomaly in late Miocene sandstone reservoir appeared in 3D seismic survey on the Öcsöd–Martfű structural height. After successful test, the well was completed as a gas producer. The reservoir has an extension of ~1300 m in SW-NE and ~600 m in NW-SE direction, respectively. The reservoir is located between depths of 2104 - 2120 m MD (2020-2036 m TVD). The porosity of the net reservoir is 17% in average, the highest initial formation pressure is 207 bar, and the maximum formation temperature is 125 °C based on well testing data. Core samples from Öcsöd-1 and drill cutting samples from 3 intervals from OGD-Öcsöd-K-2 were selected for further detailed analyses (Figure 8).

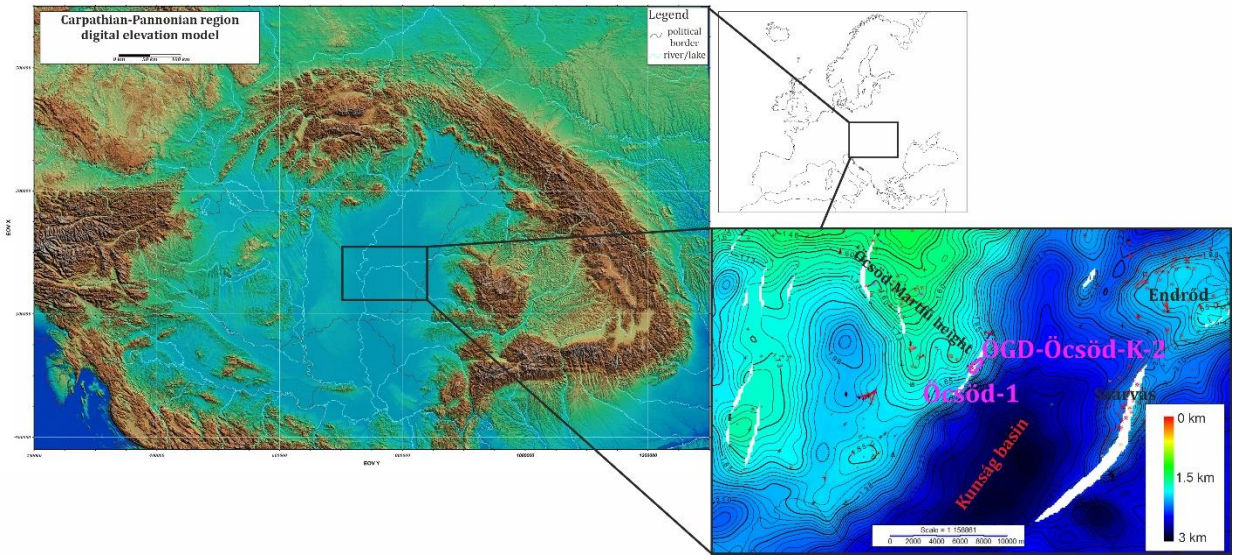

Figure 7. *Location of the study area. Neogene basement map (bottom right) shows the position of the reservoir (in magenta), subject of this study. The studied wells are located between Öcsöd–*

Martfű height and the Kunság basin, Great Hungarian Plain. Endrőd site is located northeast of Öcsöd site. Digital elevation model is modified after Horváth et al. (2006a).

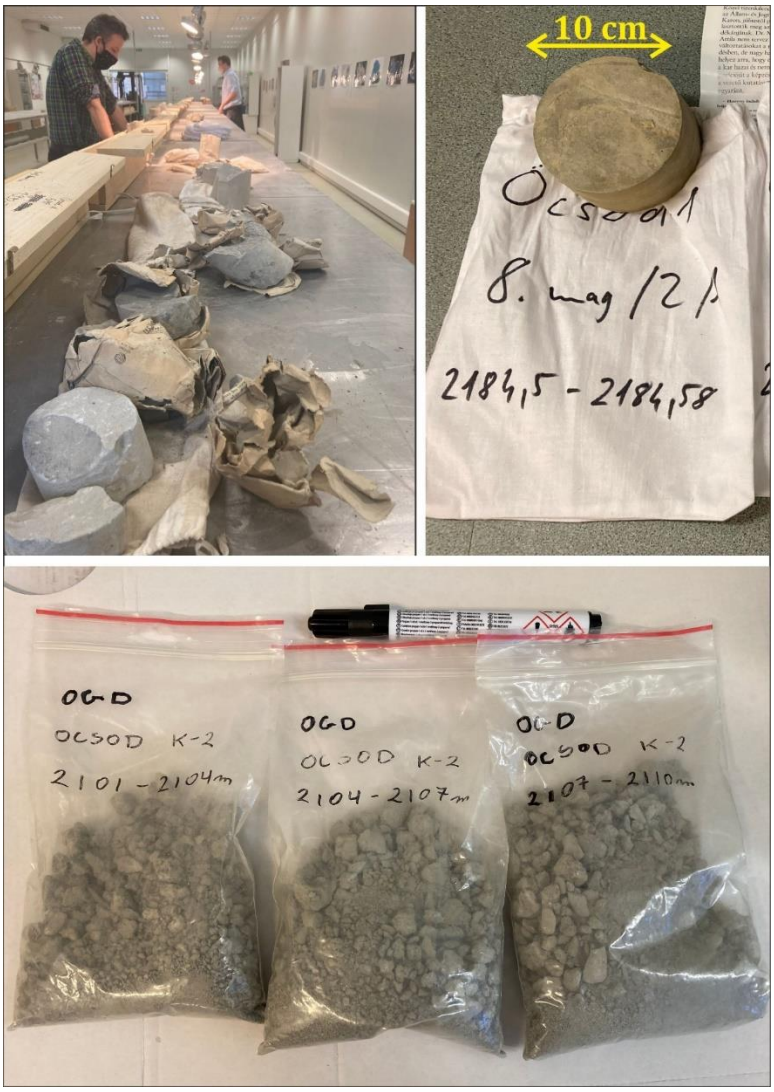

***Figure 8**. Photos from rock samples used in this study. The upper left picture was taken during core inspection of Öcsöd-1 borehole. The upper right photo shows the selected core sample representative of reservoir rock. The bottom picture was taken of the cutting samples from OGD-Öcsöd-K-2 borehole.*

3.2. Sample preparation from Öcsöd-1 and OGD-Öcsöd-K-2 wells

Sample preparation of rock samples was carried out in the Lithosphere Fluid Research Lab (LRG), Eötvös Loránd University (ELTE), Budapest. For petrographic observations, SEM and EMPA

analysis, core sample was cut to make appropriate size rock slab with flat surface. Then the sample was mounted in two-components epoxy resin and dried for 24 hours at room temperature. Polished surface was achieved manually, using Buehler diamond grinding discs (60, 45, 1, 0.5 µm), silicon carbide papers (P600, P800, P1000) and polishing cloth (VerduTex). Once sufficiently polished sample surfaces were acquired, they were cleaned, dried and mounted on glass slides with Loctite Super Bond instant glue. Thin sections were dried for 24 hours at room temperature. Then the non-mounted part of the samples was cut using a Buehler Isomet low speed saw to create thin (2-3 mm) slabs for further thinning. Final polishing was completed using the same material as described above.

Cuttings were handpicked under stereo microscope with focus for sandstone fragments, which are representative of the reservoir rock. The selected cuttings were embedded into epoxy resin. After drying, the mounted samples were grinded and polished at one side.

For XRD analysis, 1 g of cuttings sample was grinded and powdered to grain size of ~1 µm. The powdered samples were loaded to the sample holder of the X-Ray diffraction device.

3.3. Materials used in experiments and their preparation

The experiments were carried out using natural minerals. Calcite (Iceland spar) (BE24569, BE40764, BE40763), K-feldspar (BE40767) and pyrite (BE40766) were used as model substrates provided by the Mineralogical Collection of Natural History Museum, ELTE. Prior to experimental work, their homogeneity and chemical composition of the natural samples were analyzed by various methods (e.g., petrographic microscope, XRD, SEM, ICP-OES). The single crystals were crushed by hammer and powdered in agate mortar. For XRD analysis, 1 g of sample (selected mineral) was grinded and powdered to grain size of ~1 µm. The powdered samples were loaded to the sample holder of the X-Ray diffraction device.

Grains for the experiments were selected with a particle size between 100 and 200 µm using wet sieving. In the case of pyrite, smaller grainsize was applied (63-125 µm). A few pieces of coarse sized pyrite (2-3 mm) were also included in the experiment to assure proper target for X-ray photoelectron spectroscopy (XPS) measurements. The pyrite powder was washed with 0.5 M HCl for 10 min and cleaned in ultrasonic bath for 45 s, similarly to the preparation method of Truche *et al.* (2010). Then, the powder was washed with distilled water and dried under a vent hood. After drying, pyrite grains were checked under stereo microscope to avoid contamination on the surface.

The cleaning procedure was performed immediately before the experiment to minimize surface oxidation.

Untreated, cleaned and experimentally treated (H_2, N_2) pyrite grains (2-3 mm in size) were handpicked and fixed on carbon tape for XPS analyses. The pyrite grains were fixed to the sample holder with carbon tape topping near flat surface, ensuring sufficient near plain area and lateral condition facing toward the analyzer. The H_2-treated grains were also prepared for SEM-EDX analyses.

Double distilled water was used for both experiments. The solution samples of experiments were filtered through a 0.2 µm syringe filter and mixed with ca. 5 mL of 1 wt.% HNO_3 solution for stabilization. The samples were sealed and stored in scintillation vials for later analysis.

Gases were provided by Linde Ltd. and Siad Ltd. with the following purities: H_2 5.0, N_2 5.0 and 4.6, Ar 4.6.

4. Methods

4.1. Petrography with polarized light microscopy

Petrographic analysis was carried out on representative polished thick and thin sections. Optical microscopy was applied on individual mineral grains to observe differences among H_2-treated, reference gases (N_2 and Ar) treated, and untreated pyrite and calcite grains. For this purpose, stereo (Nikon SMZ 800) and petrographic (Nikon Eclipse LV100POL) microscopes were used. Photomicrographs were taken with a Nikon DS-Fi1 digital camera that is attached to the Nikon microscope using a NIS Elements AR 2.20 digital imaging software in the LRG, ELTE Budapest Hungary.

4.2. X-ray powder diffraction (XRD)

The X-ray powder diffraction (XRD) measurements were performed on powdered rock and mineral samples at the Department of Mineralogy, ELTE, using a Siemens D5000 diffractometer, for structural determination of the minerals. The instrument was operated with the following conditions: 45 kV, 35 mA, Cu Kα-radiation, graphite monochromator, 0.05° 2Θ step, and 2 sec detecting time. In the case of core samples, Siroquant software with Rietveld refinement method was used to determine the mineral content quantitatively in weight% (wt.%). In the cuttings, the mineral composition has been determined semi-quantitatively and excluded the phases possibly present in the drilling mud (e.g., barite, sylvite).

4.3. Scanning electron microscopy with energy dispersive X-ray spectroscopy (SEM-EDX)

To obtain the major element composition of the minerals used in the experiments and of the rock samples and cuttings, a Hitachi TM4000Plus scanning electron microscope, equipped with Oxford AZtec One 30 mm^2 SDD energy dispersive spectrometer was used at the Center for Research and Industrial Relations, ELTE, Budapest, Hungary. The accelerating voltage was 15 kV and the beam current was 200 pA during the measurements.

4.4. Electron microprobe analysis (EMPA)

Major element analyses of the rock-forming minerals (feldspars and carbonates) from cuttings of OGD-Öcsöd-K-2 were conducted using a JEOL JXA-8230 SuperProbe at the Institute of Earth Sciences, University of Iceland. The microprobe is equipped with five wavelength-dispersive spectrometers (WDS) and an energy-dispersive spectrometer (EDS). A total of 38 K-feldspar (from 9 rock cuttings), 69 plagioclase (from 15 cuttings) and 164 carbonate (from 17 cuttings) measurements were carried out. The analyses were acquired using a 15 keV accelerating voltage and a probe current of 10 nA and 5 nA for feldspars and carbonates, respectively. The K-feldspar and carbonate were analysed with a defocussed beam of 10 µm diameter and plagioclase with 5 µm beam. Measured elements were Si, Ti, Al, Fe, Mn, Mg, Ca, Na and K in feldspars, but Fe, Mn, Mg and Ca in carbonates with 20-40 s peak counting time. For the carbonate, plagioclase and K-feldspar analyses, natural standards were used (Appendix 10.7). Precision and accuracy were estimated by repeat measurements of secondary standards before and after each session. Data reduction was made with the CITZAF software (Armstrong 1991) for all analyses.

4.5. Inductively coupled plasma optical emission spectroscopy (ICP-OES)

For chemical composition analysis of the solution and mineral samples (calcite, feldspar) inductively coupled plasma - optical emission spectrometry (ICP-OES) was used. The instrument was a HORIBA Jobin Yvon® ULTIMA 2C of an accredited laboratory in the Supervisory Authority of Regulatory Affairs Hungary. The measurements were carried out according to the MSZ EN ISO 11885:2009 standard. This method is applicable for the determination of dissolved elements, elements bound to particles ("particulate") and total content of elements in different types of waters. The measured concentration values are given as mg/L for solution samples. The

relative error (10%, 20% and 50%) of the concentrations is dependent on the concentration range, with higher errors at concentrations closer to the detection limit (Table A.10.4).

4.6. X-ray photoelectron spectroscopy (XPS)

The X-ray photoelectron spectroscopy (XPS), also formerly known as electron spectroscopy for chemical analysis (ESCA), is a technique for analyzing the material surface. Surface composition, oxidation state and chemical bonding information can be obtained with this technique (Bancroft *et al.* 1979). In brief, the analysis is accomplished by irradiating the sample with an X-rays source (e.g., Al Kα of 1486.6 eV) and analyzing the kinetic energies of the photoelectrons detected. The incident X-rays interact with atoms of the sample resulting in photoelectron emission from the surface region, namely upper few nm. The kinetic energy (E_K) of the emitted electrons given by Eq (1) (Seah 1983):

$$E_K = h\nu - E_B \qquad \text{(Eq.1)}$$

where $h\nu$ is the photon energy (energy of the incident X-ray), E_B is the binding energy of the electron under investigation. In practice, the kinetic energies are detected, and the outcome is a plot of number of photoelectrons versus binding energy. Additional advantages of this technique include its non-destructive nature and the easy sample preparation (e.g., coating, grinding and flat surface are not needed).

Angular resolved measurements (ARXPS) can provide the chemical species distribution as a function of depth. This technique enables analysis and quantification of thin overlayers or contaminants on a surface. Based on Seah (1983), the signal from the overlayer A covering the substrate B is given by:

$$I_A = I_A^{\infty}\left[1 - e^{-\frac{d_A}{\lambda_A(E_A)\cos\theta}}\right] \qquad \text{(Eq.2)}$$

where I_A^{∞} is the intensity of the XPS signal from pure A, d_A is the thickness (nm) of the overlayer, $\lambda_A(E_A)$ is the inelastic mean free path of the characteristic XPS electrons of energy E_A from element A in matrix A and θ is the angle of emission of the electron measured from the surface normal (Figure 9).

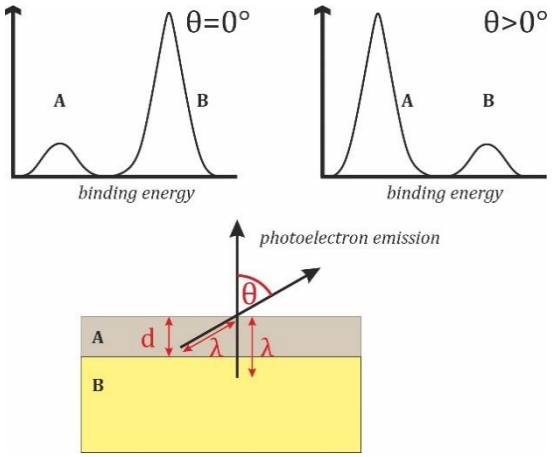

Figure 9. *Illustration of the angle resolved XPS analysis of a thin overlayer A on a substrate B. The schematic spectra shows that XPS data collected at surface normal (θ=0°) have a dominant peak from the material B, whereas at near grazing angle (θ>0°) the peak of overlayer material A emerges.*

The XPS analysis was carried out at Research Institute for Technical Physics and Materials Science, HUN-REN Centre for Energy Research, Hungarian Research Network using an Escalab Xi+ (produced by Thermo Fisher) equipment including both the common spectra detection and ARXPS. It operates at a base vacuum level 2×10^{-10} mbar. The XPS spectra were obtained with 0.6 eV energy resolution using monochromatized Al Kα source focused onto area with 0.5 mm diameter. The samples had enough surface area to enable more independent (not overlapping) measurements on the same pyrite grain. The ARXPS spectra were detected with 0.3 mm spot size. The sample holder was tilted by 10º steps covering the 0º-60º range regarding the top face normal relative to the analyzer axis.

Compositional changes on the surface of pyrite grains due to exposition to nitrogen and hydrogen under reservoir conditions were determined by XPS analysis (Table 2). Detected peaks were Fe 2p 3/2 (707 eV), S 2p (162eV), O 1s (532 eV), N 1s (400eV) and C 1s (284 eV). Further trace components of the pyrite grains, like Ca and Si, were also detected although were not considered in the evaluation since their trace concentration did not influence the observed reactions and conclusions.

The measured spectrum was evaluated by determining the peak intensities. Decomposition of complex peak shapes (in case of Fe and S) were carried out with peak fitting algorithm using the built-in software (Avantage) of Escalab equipment. Peak intensity was quantified by the area of

the peak. Simple way composition was calculated by assuming homogeneous target of XPS analysis.

Table 2. List of pyrite samples which were used to XPS analyses.

ID	Description	Conditions
PPR	untreated pyrite	long time (6 months) exposed to the atmosphere
PCl	cleaned pyrite	0.5 M HCl, ultrasonic
PH2	H_2-treated pyrite grains	Pyrite + water + H_2 (105 °C, 100 bar)
PN2	N_2-treated pyrite grains	Pyrite + water + N_2 (105 °C, 100 bar)

4.7. Experiments

4.7.1. Regular experimental setup

The mineral–distilled water–H_2 batch experiments were performed in 160 mL Hastelloy Steel High-pressure Parr® reactors. The first experiments took place at the Department of Chemical and Environmental Process Engineering, University of Technology and Economics, Budapest. Later, in 2022, as a part of this PhD project a high pressure and temperature laboratory was built up at the ELTE-LRG dedicated to the underground hydrogen storage related experiments.

The experimental setup follows a similar procedure with each mineral. In a typical experiment 2 g mineral and 70 mL of distilled water were placed into the reactor. That was followed by its pressurization up to 80 bar for both the H_2 and reference gas (N_2, Ar) containing experiments. The reaction mixture was then heated up to 105 °C and the total system pressure was set up to 100 bar. Stirring was continuous by a four-bladed turbine stirrer with an RPM of 345 min^{-1}. At given reaction times (3, 24, 78 hours), ca. 2 mL of solution samples were taken via dip tube into the sample holders for off-line analysis to detect the changes of ion concentration in the solutions. The amount of the solution sampled was small enough to preserve the original mineral-water ratio (1:35), yet sufficient for chemical concentration measurements with ICP-OES. The main parameters of experiments discussed in this study are summarized in Table 3.

Table 3. Experimental details of regular experiments grouped by minerals (Cc – calcite, Kf – K-feldspar, Cpv – pyrite) including the used minerals, gases (H_2 – hydrogen, N_2 – nitrogen, Ar – argon), and solution sampling date (year, month, day) and the mass (g) of collected aliquots for ICP-OES measurement. dw: distilled water sample.

ID	Mineral	Gas	sampling date	stabilizing solution (g)	sampled mass (g)
Cc_1_1	calcite (Cc)	H_2	2021.08.31.	5.1725	0.3133
Cc_1_2			2021.09.01.	5.2862	0.4898
Cc_1_3			2021.09.03.	4.9288	1.3690
Cc_2_1	calcite (Cc)	N_2	2021.09.14.	5.2326	1.0177
Cc_2_2			2021.09.15.	5.0317	1.6060
Cc_2_3			2021.09.17.	5.1321	1.7268
Cc_2_4			2021.09.14.	dw	
Cc_3_1	calcite (Cc)	H_2	2021.10.05.	5.0860	1.2654
Cc_3_2			2021.10.06.	5.1000	1.8079
Cc_3_3			2021.10.08.	5.1259	1.7608
Cc_3_4			2021.10.05.	dw	
Cc_4_1	calcite (Cc)	N_2	2021.10.12.	5.0050	1.7126
Cc_4_2			2021.10.13.	5.1419	1.4909
Cc_4_3			2021.10.15.	5.0344	1.8912
Cc_4_4			2021.10.12.	dw	
Cc_5_1	calcite (Cc)	H_2	2022.03.07.	5.0599	1.6070
Cc_5_2			2022.03.08.	5.0806	1.5647
Cc_5_3			2022.03.10.	4.9631	1.8144
Cc_5_4			2022.03.07.	dw	
Kf_1_1	K-feldspar (Kf)	H_2	2021.09.28.	4.9811	1.1826
Kf_1_2			2021.09.30.	5.1496	1.6888
Kf_1_3			2021.10.01.	5.1045	1.6123
Kf_1_4			2021.09.28.	dw	
Kf_2_1	K-feldspar (Kf)	H_2	2021.11.23.	4.9645	1.4625
Kf_2_2			2021.11.24.	4.9837	1.4853
Kf_2_3			2021.11.26.	5.1395	1.5545
Kf_2_4			2021.11.23.	dw	
Kf_4_1	K-feldspar (Kf)	N_2	2022.01.17.	5.0779	2.1184
Kf_4_2			2022.01.18.	5.0802	1.6008
Kf_4_3			2022.01.20.	4.9200	2.2730
Kf_4_4			2022.01.17.	dw	
Kf_5_1	K-feldspar (Kf)	N_2	2022.06.27.	5.0418	2.0929
Kf_5_2			2022.06.29.	4.9503	2.206
Kf_5_3			2022.06.30	5.1299	2.2505
Kf_5_4			2022.06.27.	dw	

Kf_6_1	K-feldspar (Kf)	N_2	2023.06.05.	4.9953	3.9618
Kf_6_2			2023.06.06.	4.9973	2.0417
Kf_6_3			2023.06.08.	4.997	0.9809
Kf_6_4			2023.06.05.	dw	
Cpv_1_1	calcite-pyrite 10 wt.%	H_2	2023.02.21.	5.0131	3.4065
Cpv_1_2			2023.02.22.	5.0171	2.8924
Cpv_1_3			2023.02.24	5.0121	2.4924
Cpv_1_4			2023.02.21.	dw	
Cpv_2_1	calcite-pyrite 5 wt.%	H_2	2023.02.28.	4.9814	3.0693
Cpv_2_2			2023.03.01.	5.0077	3.0567
Cpv_2_3			2023.03.03.	5.0814	2.8990
Cpv_2_4			2023.02.28.	dw	
Cpv_3_1	calcite-pyrite 10 wt.%	N_2	2023.04.18.	5.0114	2.4837
Cpv_3_2			2023.04.19.	5.0019	2.9024
Cpv_3_3			2023.04.21.	5.0959	3.0355
Cpv_3_4			2023.04.18.	dw	
Cpv_4_1	calcite-pyrite 1 wt.%	H_2	2023.05.09.	5.1028	2.8530
Cpv_4_2			2023.05.10.	5.0171	3.0555
Cpv_4_3			2023.05.12.	5.0994	3.0390
Cpv_4_4			2023.05.09.	dw	
Cpv_5_1	calcite-pyrite 5 wt.%	H_2	2023.09.12.	5.2963	2.6090
Cpv_5_2			2023.09.13	4.9419	2.4765
Cpv_5_3			2023.09.15	5.0531	2.9773
Cpv_5_4			2023.09.12.	dw	
Cpv_6_1	calcite-pyrite 10 wt.%	Ar	2023.11.07	5.0021	2.7653
Cpv_6_2			2023.11.08	5.0234	2.9926
Cpv_6_3			2023.11.10	5.0742	2.8994
Cpv_6_4			2023.11.07	dw	

4.7.2. Pre-pressurization experimental setup

"Pre-pressurization" experiments were also carried out to study the effect of mineral dissolution under ambient temperature and pressure conditions, which should not be counted to the effect of pressurized gases and elevated temperature. For this purpose, the same amount of mineral and distilled water was mixed in the reactor vessel for 10 minutes under ambient temperature and pressure conditions to track the effect of mineral immersion in the water before batch experiments similarly to procedure of Stillings *et al.* (1995). The initial and final pH and chemical composition of the solutions were measured. The chemical concentrations obtained from these pre-pressurization experiments served as input data for the geochemical models mentioned above.

4.8. Geochemical modeling

Geochemical modeling was carried out using the PHREEQC ver. 3 geochemical software (Parkhurst and Appelo 2013) designed for simulating geochemical reactions in aqueous media. It integrates thermodynamic equilibrium and kinetic reactions for rock-water-gas interactions.

The kinetic models consider dissolution and precipitation rates of solid phases, assuming that chemical reactions may not reach equilibrium within the timescale of interest. This approach is useful to analyze the effects of temperature, pressure, concentrations of compounds on the reaction rate over time. This method is useful in understanding reaction kinetics and its results are comparable with short-term laboratory experiments.

The equilibrium models assume that all geochemical reactions reach equilibrium instantaneously. Typical applications for this concept are the modeling of long-term effect of gas injection (e.g., H_2, CO_2) into porous media. The focus is on the final state of the system, disregarding the time required for reactions to proceed. Equilibrium modeling was used for reservoir rock-fluid and hydrogen simulations to predict long-term effect of hydrogen on the reservoir.

4.8.1. Kinetic model scenarios

Kinetic batch models were applied in parallel with experimental work to predict the chemical behavior of single mineral phases.

To investigate **calcite** reactivity under subsurface hydrogen storage conditions, calculations were performed using both the original `phreeqc.dat` thermodynamic database, and subsequently, a modified `phreeqc.dat` thermodynamic database was created. The following geochemical simulations were performed as representatives for calcite batch experiments:

- Cc_Model #1: As a first step, a thermodynamic batch model was run to simulate the equilibrium between water, calcite, and air at atmospheric conditions. The results of this model represent the initial state of the experiments before heating and pressurization.
- Cc_Model #2: Using the output from Model #1 as initial solution composition, a kinetic batch model was run to follow the calcite dissolution in water at 105 °C and 100 bar H_2 pressure.
- Cc_Model #3: Since geochemical reactions are taking place under aqueous conditions even without the presence of any injected gas, a reference model was built with the same input data as Model #2, except the addition of H_2. This model is comparable with the N_2 experiments and

helps to differentiate between processes related to the increase of pressure and temperature only and H_2 injection induced geochemical effects.

In the case of kinetic **feldspar** models, unmodified data file `phreeqc.dat` was used for the gas−water−mineral reactions at subsurface reservoir temperature and pressure. With input solution composition using the chemical results of pre-pressurization experiment, kinetic models were run to follow the K-feldspar dissolution in water at 105 °C and 100 bar H_2 similar to experimental conditions. Time steps were selected to follow the experimental solution sampling times.

Calculations of kinetic **calcite**−**pyrite** models were performed using `phreeqc.dat` database with modification described above for calcite. Kinetic models were run to follow the pyrite and calcite dissolution in water at 105 °C and 100 bar H_2 identical to experimental conditions. The initial solution composition was based on the chemical results of pre-pressurization experiment. The time steps were set from 0 to 76 hours in accordance with the sampling times of the experiments. To achieve closer fit with the experimental data, kinetic dissolution rates of calcite and pyrite were manually adjusted.

4.8.2. Equilibrium model scenario

Equilibrium modeling was applied to simulate the long-term effect of H_2 gas injection. For this purpose, the modified `phreeqc.dat` database was used. The mineral composition applied in the models is based on X-ray diffraction (XRD) measurements of core sample from Öcsöd-1 well and an estimated 20% porosity for the reservoir. Pressure and average temperature values were obtained from OGD-Öcsöd-K-2 well. Mineral composition of rock obtained from XRD and petrographic observation were converted into mol/kg×water units (mol/kgW) (Table 4) using the Eq. (5). Porewater composition was obtained from En-É-10 well from Endrőd site (Figure 7). The mineral phases and porewater were equilibrated with 200 bar hydrogen at 105 °C to study the changes in mineral composition (dissolution and precipitation of minerals) of the potential hydrogen storage reservoir.

4.8.3. Model input data

Database

Calculations were performed using both the original `phreeqc.dat` thermodynamic database, which is a plain-text ASCII file containing thermodynamic data in a code-specific format. Subsequently, a modified `phreeqc.dat` thermodynamic database was created where the equations connected to the potentially non-realistic reactions forming CH_4 were blocked as it is discussed later (Gelencsér *et al.* 2023). To avoid CH_4 formation in the model, it was necessary to block both Eq. 3 and Eq. 4. The specific lines in the database, referred to as equations, are as follows:

$$CH_4 = CH_4 \quad \text{(Eq.3)}$$

$$CO_3^{-2} + 10\,H^+ + 8e^- = CH_4 + 3H_2O \quad \text{(Eq.4)}$$

Mineral composition (EQUILIBRIUM PHASES, KINETICS)

The mineral composition applied in the bulk rock models is based on XRD and petrographic data. The mineral composition relative to pore water was given in mol/kgW units using the following Eq.5 defined by (Szabó *et al.* 2017).

$$C_{mineral}\left[\frac{mol}{kgW}\right] = \frac{10 * wt\%_{mineral} * \rho_{rock}\left[\frac{g}{cm^3}\right] * vol\%_{rock}}{M_{mineral}\left[\frac{g}{mol}\right] * vol\%_{water}} \quad \text{(Eq.5)}$$

where $c_{mineral}$ is the amount of mineral in mol/kgW, $wt\%_{mineral}$ is the weight percent (wt.%) of mineral (measured by XRD) normalized to 100%, ρ_{rock} is the density of rock (g/cm^3) calculated as the weighted average of mineral densities, $vol\%_{rock}$ is the proportion of rock in the bulk rock volume (100−porosity) (%), $M_{mineral}$ is the molar mass of the mineral (g/mol) and $vol\%_{water}$ is the volume filled with water (porosity) (%).

Table 4. List of minerals (primary and secondary solid phases) and they initial amount (in wt.%) defined in the geochemical model applied for Öcsöd reservoir hydrogen injection simulation.

Mineral	Formula	wt.%
quartz	SiO_2	49.2
albite	$NaAlSi_3O_8$	10
muscovite	$KAl_2Si_3AlO_{10}(OH)_2$	5.1
calcite	$CaCO_3$	12.5
ankerite	$Ca(Fe,Mg,Mn)(CO_3)$	11.5
dolomite	$CaMg(CO_3)_2$	0.3
kaolinite	$Al_2Si_2O_5(OH)4$	2.3
illite	$(KAl)_2(Si,Al)_4O_{10}[(OH)_2(H_2O)]$	3.9
chlorite	$(Mg,Fe)_3(Si,Al)_4O_{10}(OH)_2 \cdot (Mg,Fe)_3(OH)_6$	4.2
pyrite	FeS_2	1
pyrrhotite	FeS	0

Table 5. Equilibrium constants and relevant chemical reactions used in geochemical models.

Mineral Phase	**Reaction**	**Log K**
Calcite	$CaCO_3 = CO_3^{2-} + Ca^{2+}$	−8.480
K-feldspar	$KAlSi_3O_8 + 8\ H_2O = K^+ + Al(OH)_4^- + 3\ H_4SiO_4$	−20.573
Albite	$NaAlSi_3O_8 + 8\ H_2O = Na^+ + Al(OH)_4^- + 3\ H_4SiO_4$	−18.002
Gibbsite	$Al(OH)_3 + 3\ H^+ = Al^{3+} + 3\ H_2O$	5.800
Pyrite	$FeS_2 + 2\ H^+ + 2\ e^- = Fe^{2+} + 2\ HS^-$	−18.479
Pyrrhotite	$FeS + H^+ = Fe^{2+} + HS^-$	−3.915

Solution composition (SOLUTION)

The parameters, defined in SOLUTION data block of the bulk rock equilibrium model, are listed in Table 6. Due to the lack of reliable pore fluid chemistry data from OGD-Öcsöd-K-2 and Öcsöd-1 wells, well data from Endrőd site (En-É-10) (Figure 7) was used which has been used for geochemical modeling for CO_2 injection simulation (Table 6) (Szabó *et al.* 2018).

Table 6. Solution input parameters for bulk rock equilibrium model. Solution composition is obtained from Endrőd site (En-É-10).

Parameters	**Value**
pressure (bar)	273
temperature (°C)	135
pH	8.3
ionic strength (mol/kgW)	0.557
Na^{+}(mg/L)	10300
K^{+}(mg/L)	1530
Mg^{2+}(mg/L)	51
Ca^{2+}(mg/L)	79
$Fe^{2+/3+}$(mg/L)	0.23
Cl^{-}(mg/L)	16900
NH^{4+}(mg/L)	184
HCO^{3-}(mg/L)	1958
SO_4^{2-}(mg/L)	1592
dissolved SiO_2(mg/L)	148
Al^{3+}(mg/L)	0.05

Kinetic rates of mineral reactions (RATES)

A general form of the rate equation for many minerals, for acid, neutral and base/carbonate-catalyzed mechanism is presented explicitly in Eq.7 (Palandri and Kharaka 2004).

$$r = \begin{bmatrix} k_{acid} e^{-\frac{E_{acid}}{R}\left(\frac{1}{T}-\frac{1}{298.15K}\right)} a_{H^+}^{n_1} \\ +k_{neutral} e^{-\frac{E_{neut}}{R}\left(\frac{1}{T}-\frac{1}{298.15K}\right)} \\ +k_{carb} e^{-\frac{E_{carb}}{R}\left(\frac{1}{T}-\frac{1}{298.15K}\right)} a_{CO3^-}^{n_3} \end{bmatrix} RSA(1-\Omega) \qquad \text{(Eq.7)}$$

where r is the rate in unit of mol/s, RSA is the reactive surface area (m^2/g), E is the activation energy (J/mol), T is the temperature (K), R is the gas constant, k_{ad} is a constant factor by which the overall rate constant is adjusted: positive for catalysts and negative for inhibitors, a is the activity of species H^+ (acid mechanism) or HCO_3^- (carbonate mechanism), n is the power term. The saturation index (Ω) of the mineral, defined as $\Omega=Q/K$, where Q is the activity product and K is

the equilibrium constant. The kinetic rate parameters used for this study were primarily based on the compilation of Palandri and Kharaka (2004). The kinetic rate parameters of calcite and pyrite were also modified in the calcite−pyrite models (Table 7).

Table 7. Table of kinetic rate parameters and specific surface area (SSA in m^2/g) of minerals and relevant chemical reactions used in kinetic geochemical models to simulate experiments. The kinetic rate constant (logk) is expressed in m^{-2} s^{-1}, the Arrhenius activation energy (Ea) is in kJ mol^{-1}, and *n* is the reaction order.

Exp. ID	Mineral	acid			neutral			carbonate/base			SSA
		logk	Ea	n	logk	Ea	n	logk	Ea	n	
Cc	Calcite	−0.30	14.4	1.000	−6.81	23.5	-	−4.48	35.4	1.0	0.1
Kf	K-feldspar	−10.06	51.7	0.500	−12.41	38.0	-	−21.20	94.1	−0.823	0.09
	Albite	−10.16	65.0	0.457	−12.56	69.8	-	−15.60	71.0	−0.572	0.15
	Gibbsite	−7.65	47.5	0.992	−11.50	61.2	-	−16.65	80.1	-0.784	1.0
Cpv	Calcite	−6.50	14.4	1.000	−8.50	23.5	-	−8.5	35.4	1.000	0.01
	Pyrite	−7.13	56.9	−0.500	−4.55	56.9	0.500	-	-	-	0.2
	Pyrrhotite	−8.04	50.8	−0.597	-	-	-	-	-	-	20

5. Results and discussion

In this chapter the results and their discussion are arranged by the given topics. A significant part of the PhD work is based on experimental and geochemical modeling study of the individual reservoir rock forming minerals. Therefore, the results and discussions are grouped by minerals for better understanding. The sequence of subchapters follows the time as the experimental work evolved, which is followed by the discussion of the obtained results on complex real-life reservoir rock of Öcsöd site. The final subchapter gives an overview of the potential geologic formation of the Pannonian basin system with the implication of the results of this study and the literature.

5.1. Investigation of calcite reactivity under subsurface hydrogen storage condition

5.1.1. Results of calcite experiments and geochemical modeling

The results of the Ca^{2+} content measurements in solution, which represent the dissolution of calcite in distilled water with injected H_2 and N_2 under 100 bar at 105 °C, are shown in Figure 10 and 11. The concentration changes are very similar in each run showing a slight but consistent increase in Ca^{2+} throughout the experimental period. It is important to highlight that no significant differences between the results were obtained using either H_2 or N_2 as a reference inert gas. The solution samples collected after 3 hours show an average concentration of 12.7 ±1.27 mg/L in H_2 experiments and 11.17 ±1.12 mg/L Ca^{2+} in N_2 environment, respectively. The solutions collected right before the depressurization (after ~78 hours), have Ca^{2+} concentration of 30.3 ±3.03 mg/L in H_2, and 30.7 ±3.07 mg/L in N_2 experiments (Figure 10).

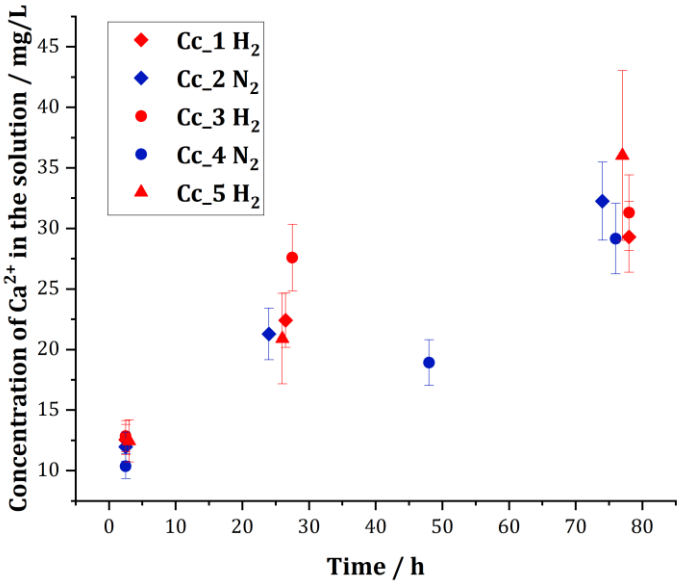

Figure 10. *Measured Ca concentration (mg/L) of solution samples in calcite (Cc) experiments of this study. The red and blue symbols indicate the Ca concentrations with H_2 and N_2, respectively.*

As for the morphological observation, using stereo microscope and SEM, the H_2-treated calcite grains are translucent, have intact edges and flat cleavage planes and show no differences compared to the untreated grains (Figure 11). Noteworthy, both morphological observations and chemical data established that no enhanced dissolution of calcite occurs in H_2 treated samples compared to N_2 treated ones, indicating that reaction Eq. 4., which could lead to CH_4 formation, is not expected in these conditions.

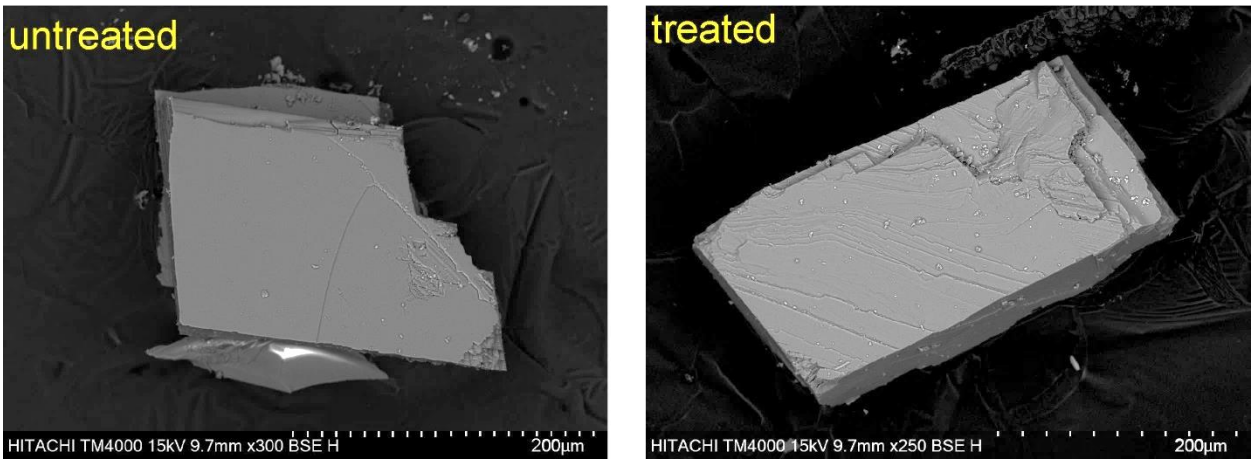

Figure 11. *Scanning electron microscopic images of calcite grains. Selected untreated calcite grain is on the left and treated grain after H_2 exposure is shown on the right. Both grains are translucent, with intact edges and flat cleavage planes.*

Geochemical modeling results show that Model #2 run with the original `phreeqc.dat` database predicts that significant calcite dissolution takes place under H_2 pressure. After 27 h, the modeled Ca^{2+} concentration in solution reaches a plateau at around 69 000 mg/L (Figure 12, Table 8). Model #2, run with the modified database with blocked reaction given by Eq. 3 and 4, resulted in a 9 mg/L Ca^{2+} concentration (Figure 3, Table 9), indicating rapid calcite saturation in the reaction mixture. In Model #3, in the absence of H_2, the Ca^{2+}concentration is again predicted to be 9 mg/L, regardless of time and the database used (Table 9).

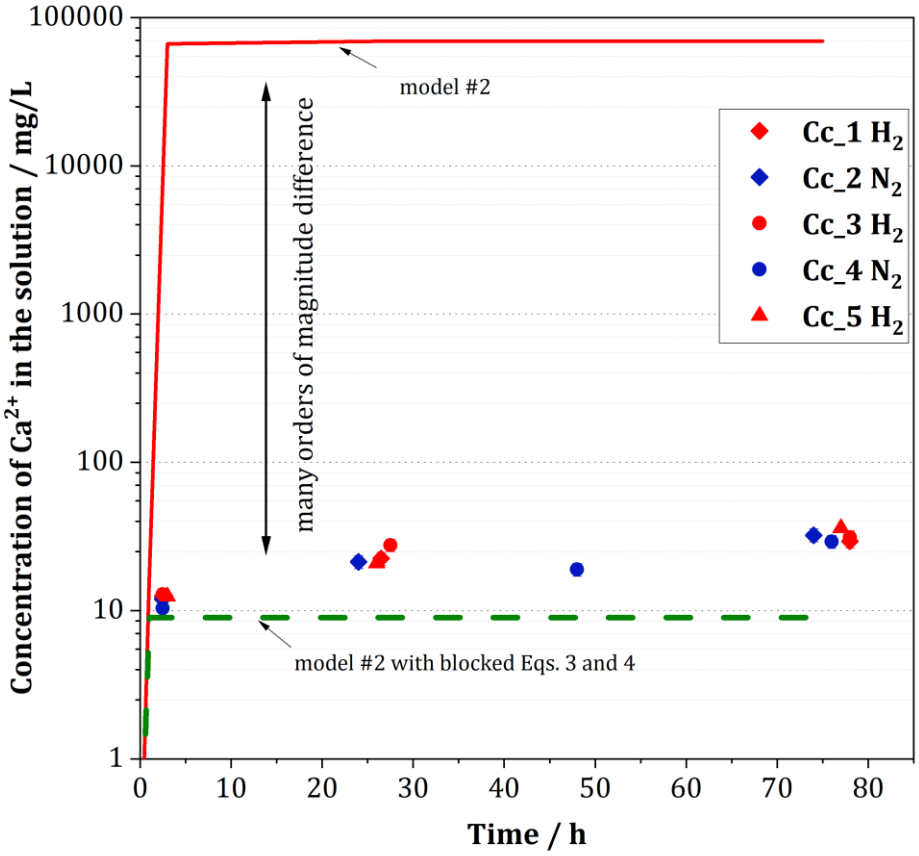

Figure 12. *Comparison of experimental and modeling data (Model #2) of Ca^{2+} concentration (mg/L) in solution as a function of time (h). The symbols with red and blue color represent the concentrations of calcite (Cc) experiments with H_2 and N_2, respectively. Red line indicates the model #2 results with default database (`phreeqc.dat`). Green dashed line shows the model #2 results with modified database (with blocked reactions in Eq. 3 and 4).*

Table 8. Measured Ca^{2+} and Mg^{2+}concentrations in solution samples of the experiments with ICP-OES technique. dw: distilled water

experiment ID	time of sampling (h)	Ca^{2+} (mg/L)	*error ± (Ca^{2+})*	Mg^{2+} (mg/L)	*error ± (Mg^{2+})*
Cc_1	2.5	12.56	*1.3*	0.97	*0.10*
	25.5	22.41	*2.24*	0.30	*0.03*
	78	29.30	*2.93*	0.16	*0.02*
Cc_2	3	11.98	*1.2*	0.09	*0.02*
	24	21.29	*2.13*	0.09	*0.02*
	77	32.25	*3.23*	0.14	*0.01*
	dw	<0.03		<0.02	
Cc_3	3	12.85	*1.29*	0.13	*0.01*
	25.5	27.59	*2.76*	0.21	*0.02*
	78	31.29	*3.13*	0.24	*0.02*
	dw	<0.03		<0.02	
Cc_4	3	10.36	*1.036*	0.07	*0.01*
	48	18.91	*1.90*	0.11	*0.01*
	77	29.15	*2.92*	0.16	*0.02*
	dw	<0.03		<0.02	
Cc_5	3	12.45	*1.25*	0.28	*0.03*
	26	20.9	*2.09*	0.29	*0.03*
	77	36.01	*3.60*	0.33	*0.03*
	dw	<0.03		<0.02	

Table 9. Variation in Ca^{2+}concentration (mg/L) in the solutions of models #2 and #3 in time (sec). Results are shown for both original and modified databases, where Eq. 3 and Eq. 4 are blocked. In models where H_2 was not used, the same Ca^{2+}concentration is predicted.

Time (h)	Database			
	Model #2 (with H_2)		Model #3 (without H_2)	
	default database	modified database	default database	modified database
0	8.69	8.69	8.69	8.69
0.0003	15.60	8.95	9.01	9.01
3	66604.8	8.96	9.01	9.01
27	69126.2	8.96	9.01	9.01
75	69126.2	8.96	9.01	9.01
151	69126.2	8.96	9.01	9.01
229	69126.2	8.96	9.01	9.01
507	69126.2	8.96	9.01	9.01

5.1.2. Evaluation and discussion of experimental results

The dissolution of carbonate minerals in water, including calcite, has received considerable attention in the scientific literature. Although experimental data are amply available about the dissolution kinetics of calcite, significant uncertainty in the absolute value of the dissolution rate under different pressures could be observed (e.g., Plummer *et al.* 1978; Arvidson *et al.* 2003). Additionally, there is a lack of research conducted in temperature and pressure conditions (105 °C, ~100 bar), at which the PhD study was performed. Therefore, relative dissolution rates were considered and results of H_2 experiments were compared to N_2 experiments.

The ICP-OES results indicate a non-significant, or at most a very small increase in calcite dissolution induced by H_2, compared to the outcomes of N_2 experiments (Figure 10). Despite the contradictions in the literature referred previously, the SEM observation of H_2-treated calcite grains of this PhD study also confirms that no obvious dissolution process occurred. Since there were no precipitates detected on the samples, neither is recrystallization process expected (Figure 11). These results are consistent with those of solution analysis (Figure 10) and indicate that H_2 has no apparent effect on calcite dissolution compared to the reference (N_2) experiments at the tested pressures and temperatures.

5.1.3. Integration of experimental and geochemical model results of calcite

The calcite dissolution in model #2 with the non-modified, original `phreeqc.dat` thermodynamic database is significantly higher than that observed in the experiments (Table 9). In the geochemical modeling work of Bo *et al.* (2021) and Zheng *et al.* (2022) considerable H_2 loss is triggered in water–calcite–H_2 simulations due to H_2 induced carbonate dissolution (Bo *et al.* 2021; Zeng *et al.* 2022). Their results, as well as model #2 of this study, are based on calculations including CH_4 producing reactions. On the contrary, model #2 with a database modification (blocking Eqs. 3 and 4), resulted in predicted Ca^{2+} concentrations in the solutions at the same order of magnitude as in the experiments (Figure 12). This modification is in line with the kinetic models of the Underground Sun Storage report and Hassannayebi *et al.* (2019) since the methane/bicarbonate redox pair was blocked in their models (Bauer 2017; Hassannayebi *et al.* 2019), however in their work no experimental evidence was presented.

Equations 3 and 4 are responsible for the severe carbonate mineral dissolution in the original unrealistic model. These or similar reactions can be found in several recently used databases (e.g., `llnl.dat`, `ThermoChimie.dat`, `PHREEQC_ThermoddemV1.10_06Jun2017.txt`,

`thddem_aug09t4.dat`), not only the `phreeqc.dat` used in this PhD study. This reaction is known to proceed in the presence of a catalyst (e.g., Pd), which could not be expected in the UHS rocks and under realistic geological conditions studied (Lux *et al.* 2018; Vialle and Wolff-Boenisch 2024). Therefore, to obtain acceptable simulations, Eqs. 3 and 4 should be manually blocked in the used model database avoiding unrealistic results that could lead to incorrect conclusions for UHS.

Consequently, the numerical values (e.g., equilibrium constants of the reactions, change in enthalpy of the reactions and activity coefficients) are herein proposed to be adjusted in the model databases to provide better match with the abiotic geologic environments if manual modifications are aimed to be avoided.

5.2. Investigation of K-feldspar reactivity under subsurface hydrogen storage conditions

5.2.1. Results of K-feldspar experiments

The changes in solution composition of experiments dominantly indicate continuous dissolution of the K-feldspar (Figure 13). The solution samples collected after 3 h show variation in potassium concentration from 0.6 to 6.9 mg/L and from 0.7 to 1.4 mg/L in H_2- and N_2-treated runs, respectively. The K^+ content of solutions after 76 hours of H_2 exposure varies from 1.77 to 10.68 mg/L with an average of 6.2 mg/L whereas it can range between 1.77 and 8.12 mg/L with an average of 4.8 mg/L in the N_2 pressurized experiments. The concentration changes show a slight but consistent increase in the measured ions throughout most of the experiments. The average concentration of K^+ and Na^+ is higher in the H_2-treated samples while the average Si and Al concentrations are higher in N_2-treated sample solutions (Figure 13. Table 10). Some precipitates were observed by optical microscopy on K-feldspar surface which can be characterized as irregular translucent grains ranging from 1 to 5 µm in size (Figure 14.).

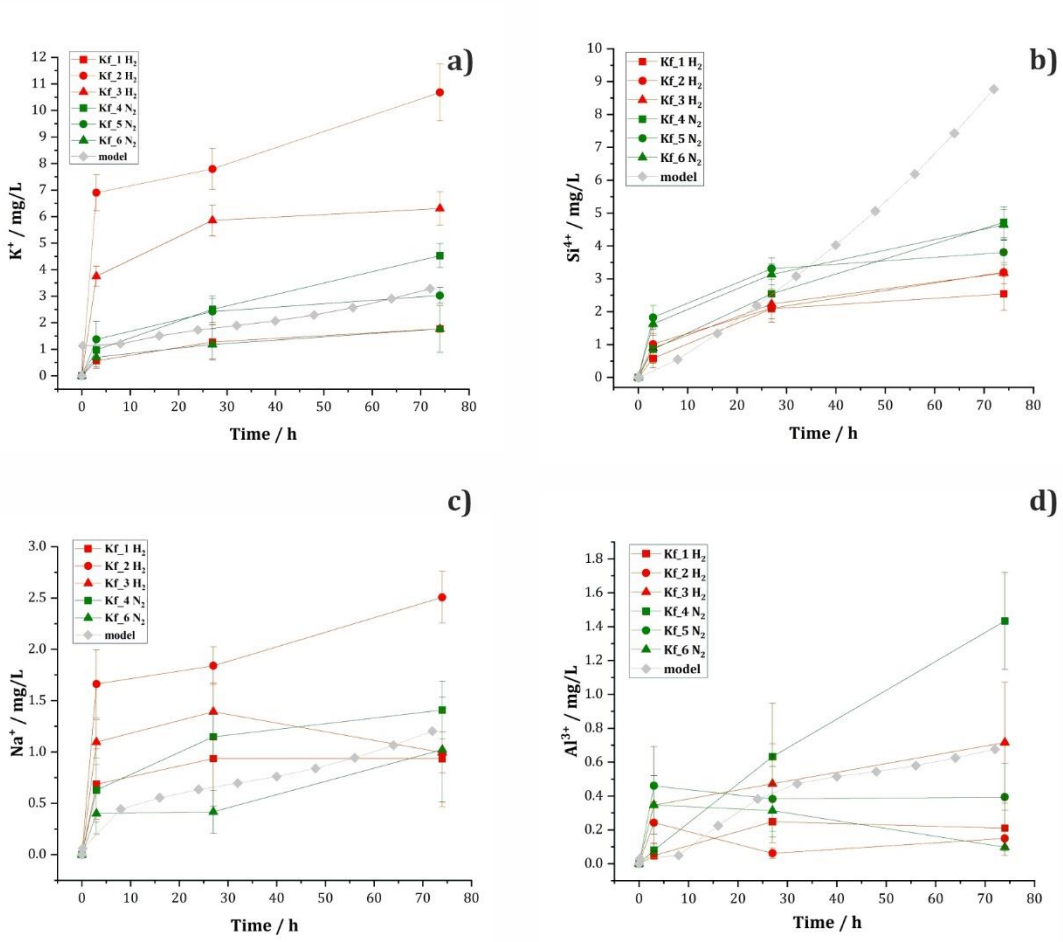

Figure 13. *Changes in solution composition in the experiments and in kinetic model (grey). The red and green symbols indicate the element concentrations (K, Na, Si Al) in the solution samples of the experiments with H_2 and N_2, respectively.*

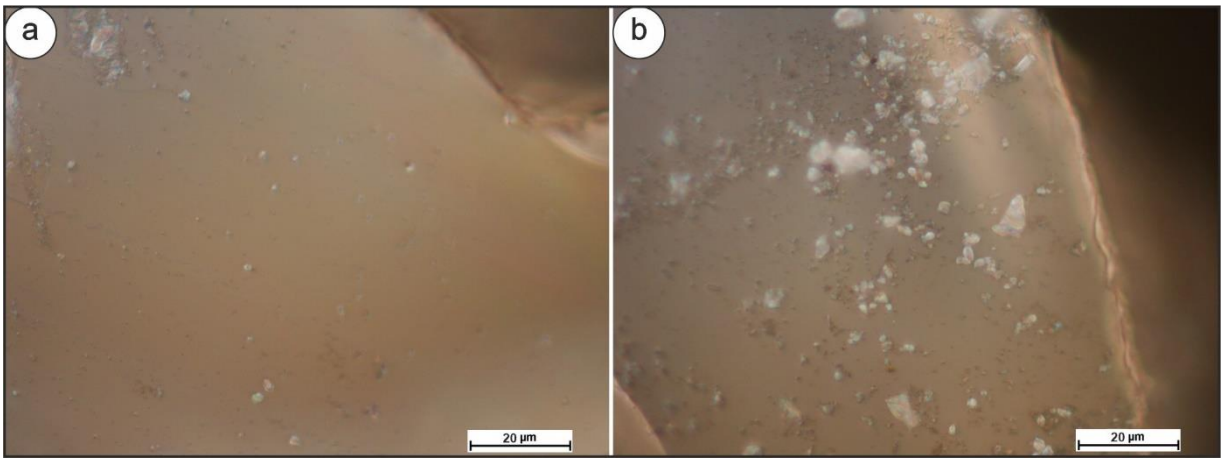

Figure 14. *Photomicrographs of K-feldspar grains before (a) and after (b) experiment. The treated K-feldspar surface is characterized by translucent precipitates having irregular shape.*

Table 10. Results of ICP-OES measurements on solution compositions of experiments with H_2 and N_2. The results are grouped by elements and concentrations with error (+/−) given in mg/L. Time of sampling from the beginning of the experiments are given in hours.

Element	Time	H2_1	*H2_1 (+/–)*	H2_2	*H2_2 (+/–)*	H2_3	*H2_3 (+/–)*	N2_1	*N2_1 (+/–)*	N2_2	*N2_2 (+/–)*	N2_3	*N2_3 (+/–)*
K	3	0.57	*0.28*	6.90	*0.69*	3.75	*0.38*	0.97	*0.49*	1.37	*0.69*	0.70	*0.35*
	27	1.28	*0.64*	7.79	*0.78*	5.85	*0.59*	2.51	*0.50*	2.42	*0.48*	1.18	*0.59*
	75	1.77	*0.88*	10.68	*1.10*	6.30	*0.63*	4.53	*0.45*	3.03	*0.30*	1.77	*0.88*
Na	3	0.69	*0.34*	1.66	*0.33*	1.10	*0.22*	0.63	*0.31*	0.78	*0.39*	0.40	*0.20*
	27	0.94	*0.47*	1.84	*0.18*	1.39	*0.28*	1.15	*0.23*	4.35	*0.43*	0.42	*0.21*
	75	0.93	*0.47*	2.51	*0.25*	1.00	*0.20*	1.41	*0.28*	0.88	*0.18*	1.02	*0.51*
Si	3	0.58	*0.29*	1.02	*0.51*	0.90	*0.45*	0.86	*0.43*	1.82	*0.36*	1.63	*0.16*
	27	2.09	*0.42*	2.10	*0.42*	2.23	*0.45*	2.55	*0.51*	3.31	*0.33*	3.13	*0.31*
	75	2.55	*0.51*	3.20	*0.64*	3.18	*0.32*	4.72	*0.47*	3.80	*0.38*	4.64	*0.46*
Al	3	0.05	*0.02*	0.24	*0.12*	0.35	*0.17*	0.08	*0.04*	0.46	*0.23*	0.35	*0.17*
	27	0.25	*0.12*	0.06	*0.03*	0.47	*0.24*	0.63	*0.32*	0.38	*0.19*	0.31	*0.16*
	75	0.21	*0.11*	0.15	*0.07*	0.72	*0.36*	1.43	*0.29*	0.39	*0.20*	0.10	*0.05*

Kinetic models predict a very similar K-feldspar dissolution path under both H_2 and N_2 pressure. The maximum difference (2.3 mg/L) appears at the end of the runs and in the Si concentration (Table 11). After 72 h, the modeled K concentration in solution reaches 3.3 mg/L and 3.9 mg/L in H_2-treated and N_2-treated runs, respectively (Figure 13, Table 11). The concentration of Si rises

the steepest among the tested ions. Overall, no significant differences between the H_2-treated and reference modeling results were obtained either. Comparing the runs with different gas types, there is no significant difference between the outcome of H_2-treated and N_2-treated runs, however the N_2-run resulted in increased concentrations of all investigated elements (K, Na, Si, Al) compared to H_2-run.

Table 11. Variation in elemental concentrations (K, Na, Si Al) in mg/L and pH of the solutions of geochemical model in time (h). Results are shown for both hydrogen and nitrogen modeling.

	time	pH	K	Na	Si	Al
Hydrogen	8	7.35	1.21	0.44	0.55	0.05
	16	7.47	1.51	0.55	1.33	0.23
	24	7.51	1.73	0.63	2.18	0.38
	32	7.55	1.90	0.70	3.08	0.47
	40	7.61	2.07	0.76	4.03	0.52
	48	7.68	2.29	0.84	5.06	0.54
	56	7.76	2.57	0.94	6.19	0.58
	64	7.83	2.91	1.06	7.43	0.62
	72	7.89	3.28	1.20	8.78	0.68
Nitrogen	8	7.35	1.31	0.48	0.77	0.10
	16	7.47	1.64	0.60	1.76	0.32
	24	7.51	1.87	0.69	2.81	0.48
	32	7.55	2.08	0.76	3.92	0.57
	40	7.61	2.33	0.85	5.12	0.63
	48	7.68	2.64	0.97	6.42	0.68
	56	7.76	3.03	1.11	7.85	0.75
	64	7.83	3.46	1.27	9.40	0.83
	72	7.89	3.94	1.44	11.08	0.91

5.2.2. Evaluation of experimental observations

A wealth of data gained from experimental, theoretical, and practical studies about the mechanisms of feldspar dissolution (e.g., Wollast and Chou 1992; Stillings and Brantley 1995), processes and kinetics (Wollast 1967), organic and inorganic reaction paths (Carothers and Kharaka 1978), have provided a solid base for understanding rock-water interactions (Yuan *et al.* 2019). However, there

is a lack of experimental studies about K-feldspar dissolution from the pressure and temperature conditions of subsurface hydrogen storage. Heinrich *et al.*(1978) carried out mineral-H_2 reactions with silicates, including feldspars. However, they did not use water in their experiments, which makes their work less comparative to underground hydrogen storage studies.

The results of this PhD show in H_2-treated experiments that K and Na have higher concentrations compared to the reference experiments whereas Si and Al have higher concentrations in N_2-bearing runs (Figure 13, Table 10). Kinetic studies have shown that the rate of dissolution of feldspars is promoted by hydrogen ions, and the rate of the dissolution increases as the hydrogen ion concentration increases (e.g., Wollast 1967; Shotyk and Nesbitt 1992).

The ICP-OES results (Table 10, Figure 13) indicate a subtle increase in K and Na dissolution induced by H_2, compared to the outcomes of N_2 experiments. Since some precipitates were detected on the treated K-feldspar samples (Figure 14) both with H_2 and N_2, a recrystallization process is expected, producing Al-bearing phase. Comparing the ratio of element concentrations in the solution of the experiments, it does not follow the stoichiometry of the K-feldspar revealing that additional process can take place but dissolution.

Since the geochemical models (both with H_2 and N_2) predict elevated Si concentrations in the solution compared to the experimental results, additional process is expected but stoichiometric dissolution of K-feldspar in the experiments. The dissolution rate is most likely controlled by the development and evolution of leached layer, built at the surface of the K-feldspar. Reactants and dissolution products can diffuse through this layer, but as the leached layer grows, the diffusion of the leachable species becomes decelerated, thus, the dissolution rate is slowing down. This phenomenon was first recognized by Correns and von Engelhardt (1938) and described later by several studies (Wollast 1967; Chou and Wollast 1984; Lasaga 1984). The process is termed as “preferential leaching-diffusion controlled mechanism” and is characterized by the parabolic curved concentrations of Al and Si versus time (Figure 15).

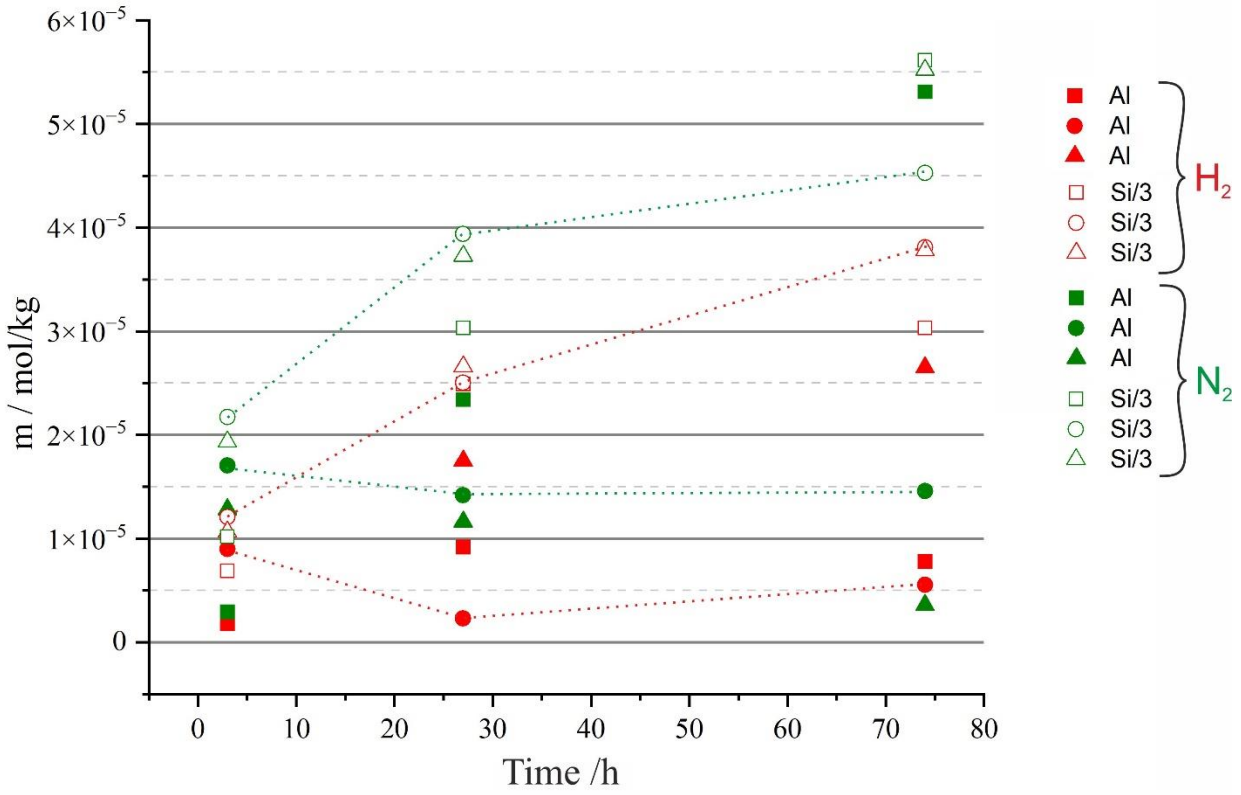

Figure 15. *Change in Si and Al element concentrations (in mol/kg) in the solution during experiments with hydrogen (red) and nitrogen (green). The filled symbols denote Al concentrations, while open symbols show Si/3 concentrations of experiments.*

However, Zhu (2005) proposed that the grounded K-feldspar powder has fresh surfaces but may also have defects which can cause non-stoichiometric alterations of the lattice. Furthermore, conclusions of this PhD study are impaired by the fact that the element concentrations, especially that of Na and Al, are close to the detection limit of the used analytical technique (Table 10, Table A.10.4.1).

Based on the experimental results of this PhD, the following steps are expected to take place according to Oelkers and Schott (1995) and Oelkers *et al.* (2008):

1) the relatively rapid exchange of hydrogen and alkali ions near the mineral surface that caused the augmented K and Na concentrations in H_2-treated experiments compared to the reference;

2) exchange reaction between three hydrogen atoms from the solution with one aluminum atom of the mineral structure, resulting in the breaking of Al−O bonds, coupled with the formation of a rate-controlling Si-rich precursor complex;
3) hydrolysis of Si−O bonds. The removal of Si still requires the breaking of Si−O bond and thus the overall K-feldspar dissolution rate is controlled by the decomposition of a silica-rich surface precursor in geochemical systems at far from equilibrium conditions.

5.2.3. Integration of experimental and geochemical modeling results for K-feldspar

The modeling results show less variation in ion concentrations (K, Na, Al, Si) than the experiments between the H_2 and reference runs (Table 10,11). However, the dissolved Al concentration of modeling calculations matches well with the experimental data with the allowing of gibbsite precipitation as a result of hydrogen treatment (Figure 13d, Table 10, 11). Therefore, the modeling predictions for solution concentrations curves are close to experimental averages, except in dissolved Si (Figure 13b), which concentration curve in the model do not become smoother, like in the experiments, rather tend to increase linearly. Although the gibbsite formation, as secondary mineral phase was proposed to precipitate in the models, the layered nature of K-feldspar dissolution mechanism was not considered, which could led to the observed difference in the Si concentrations between experimental and geochemical modeling results.
The N_2-bearing run has a slight increase in dissolved ions compared to H_2-bearing run. A plausible explanation of these discrepancy could originate from the thermodynamic database used in this modeling study. It is known that thermodynamic properties of minerals derived from calorimetric and phase equilibrium experiments rarely predict experimental solubility results accurately (Sverjensky *et al.* 1991). Zhu and Lu (2009) concluded that deriving proper rate laws from experiments is still difficult for feldspar-water systems, especially to describe the precipitation rates of secondary phases. However, the results of this PhD seem to be applicable for further, more intricate hydrogen storage simulations where bulk rock composition and formation water are considered.

5.2.4. Relevance of results on K-feldspar for underground hydrogen storage, the way forward to more complex systems

Feldspar alteration can result in various diagenetic mineral assemblages under different physicochemical conditions (Yuan *et al.* 2019). If a new reactive gas (like H_2, CO_2) intrudes into the pore space it can cause further feldspar-related chemical reactions (Henkel *et al.* 2014; Tutolo *et al.* 2015).

The low-temperature dissolution of natural K-feldspars in aqueous media is extremely slow (Lasaga 1984; Liu and Zhai 2021). However, chemical reaction time is sharply shortened (to a few hours or tens of hours) for K-feldspar under extreme hydrothermal conditions (Liu *et al.* 2015). The effect of H_2 on reservoir rocks containing K-feldspar has already been scrutinized experimentally and these authors concluded that no abiotic interactions occur with H_2 (Flesch *et al.* 2018; Yekta *et al.* 2018; Hassanpouryouzband *et al.* 2021). However, these experimental studies are based on whole rock samples, having complex mineralogical compositions, hence it is difficult to directly apply their conclusions.

K-feldspar promoted illitization in interbedded mudstones by supplying K is also observed in diagenetic environments (Yuan *et al.* 2019). Considering increased K and Na dissolution compared to N_2-treated samples of the experiments it can be assumed that H_2 addition into the solution will decrease, and the pH and the dissolution rate of feldspar will increase. An abundance of H^+ ions can accelerate reactions on the mineral surface. In polymineralic rock, under diagenetic conditions the K released from feldspar can enter illite structure which can cause pore clogging. Moreover, the experiments demonstrated that Al released from the K-feldspar immediately forms a solid phase and does not prefer the solution indicating that Al, dissolved from K-feldspar, is a source of aluminosilicate secondary phases, which can cause further pore clogging. Consequently, the newly forming aluminosilicates can reduce the porosity and permeability of the reservoir. The possible decline of these latter two parameters may adversely affect both the void space and the injectivity of the subsurface storage unit as well as hydrogen production/extraction for use.

5.3. Investigation of pyrite reactivity under subsurface hydrogen storage condition

5.3.1. Results of optical and SEM-EDX observations on pyrite surface

Pyrite grains show irregular conchoidal surface under reflected light as a result of the sample preparation. Photomicrographs of pyrite after different treatments are collected in Figure 16.

Grains exposed to atmosphere for several days have dark brown (oxidized) spots on their surface (Figure 16a). Those grains which are cleaned in HCl ultrasonically have the cleanest surfaces (Figure 16b). The N_2- and Ar-treated samples show some alteration which occurs in submicron-size reddish-dark spots (Figure 16d, e). The most conspicuous changes can be observed in the H_2-treated samples. Dark brown irregular patches occur as very fine masses on the pyrite surface (Figure 15c). These patches consist of submicron size crystals arranged in lines whereas sometimes individual submicron-size dots are also present. The degree of alteration changes with the orientation of crystal surface. The higher the share of pyrite in the experiments, the more intense alteration can be observed on the pyrite surfaces.

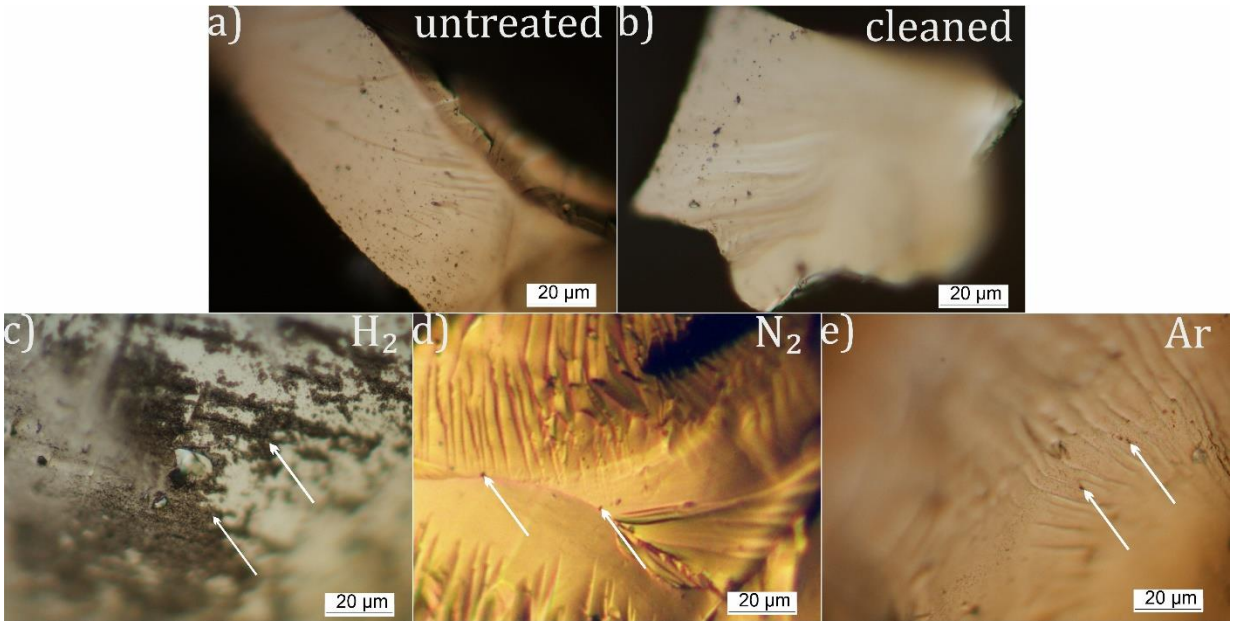

Figure 16. *Photomicrographs of pyrite samples after different treatments. Photos are taken under reflected light, 1N. a) Pyrite surface after 6-month atmospheric exposure. Dark brown spots are present on the pyrite surface. b) Pyrite surface after cleaning procedure. Dark brown spots are observable only in low amounts. c) Pyrite surface after calcite−pyrite (5 wt.%) experiment (Cpv_5) in H_2 atmosphere. Dark brown irregular patches can be observed on the pyrite surface. Pyrrhotite (arrows) occur as submicron size crystals arranged in lines or forming individual spots. d) Pyrite surface after calcite−pyrite (10 wt.%) being subjected to pressurized N_2 (Cpv_3) characterized by small amount of submicron-size, dark red spots (arrows). e) Pyrite surface after exposed to Ar (Cpv_6) is described by submicron-size dark red dark spots (arrows) similarly to d).*

The SEM-EDX measurements on the brown patches (Figure 17) referred to iron and sulfur composition with an average Fe/S atomic ratio of 0.88, whereas 0.52 was calculated on the clear pyrite surface (Table 12).

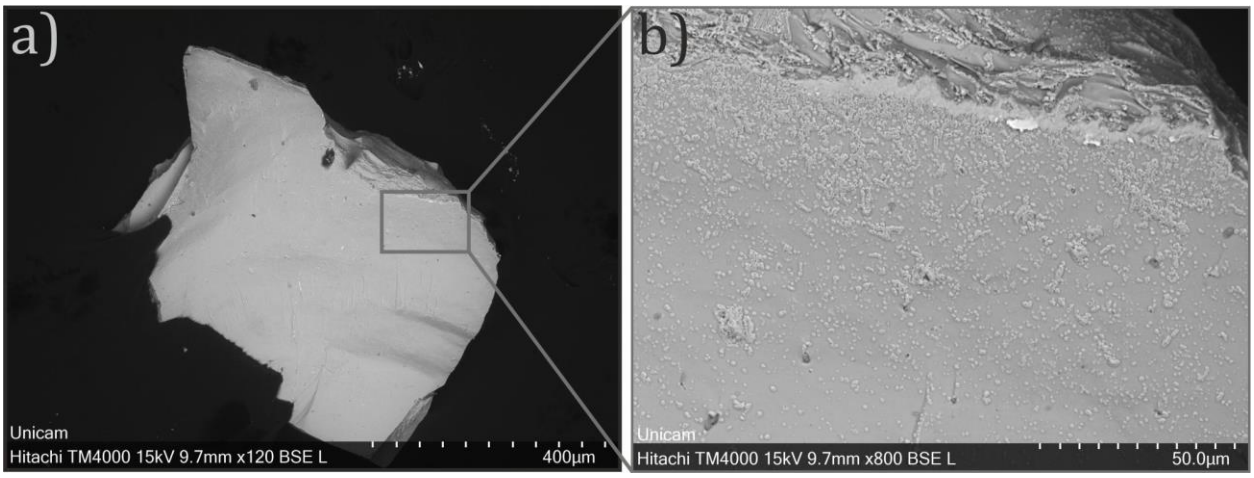

Figure 17. *Scanning electron microscopic images of pyrite grains taken with backscattered electrons. a) Pyrite grain of calcite−pyrite (5 wt.%) with H_2 experiment (Cpv_5). b) A close-up view of the pyrite grain surface with brighter patches indicating different Fe/S atomic ratio on the sample surface compared to the average pyrite Fe/S atomic ratio.*

Table 12. Results of scanning electron microscopy (SEM-EDX) analyses on H_2-treated pyrite surface expressed in at% from the calcite–pyrite (5 wt.%) experiment (Cpv_5).

point ID	Description	S at. %	Fe at. %	Fe/S
PyH_5_31	Pyrite	65.8	34.2	0.52
PyH_2_6	Pyrite	65.1	34.9	0.54
PyH_1_p1	Pyrite	66.5	33.5	0.50
PyH_5_30	Pyrrhotite	53.8	46.2	0.86
PyH_2_7	Pyrrhotite	51.5	48.5	0.94
PyH_2_9	Pyrrhotite	53.9	46.2	0.86
PyH_3_25	Pyrrhotite	53.4	46.6	0.87
PyH_3_26	Pyrrhotite	53.8	46.2	0.86

5.3.2. Results of XPS study

The results of XPS analysis are summarized in Figure 17 and 18 where binding energies of iron (Fe2*p*) and sulfur (S2*p*) are indicated. The consequence of long-time air exposure is remarked by the presence of FeO (visible Fe (II) contribution at 709 eV and oxygen content) and sulfate (SO_4) at the surface (visible at 168 eV) (Figure 17). Contrary to the observation of Nesbitt *et al.* (1998), Fe(III) contribution was negligible at grain surfaces in this study. Both FeO and SO_4 are significantly reduced after HCl cleaning, and the spectrum shows an essentially pure FeS_2 compound.

Comparing iron (Fe2p) and sulfur (S2p) peaks, measured on pyrite surface of HCl cleaned grain, H_2 treated grain and N_2 treated grain, 3 components can be distinguished in the Fe2p spectrum (Figure 19): 1) sharp peak at 707 eV reflecting FeS_2, 2) broad peak at 709 eV from Fe(II) (including sulfur-bonded Fe(II) and the Fe(II)-O), 3) broad peak from Fe(III) at 711 eV. The alteration of Fe2p peak concludes that both H_2 and N_2 treatments resulted in the increase of Fe(III) component (Figure 18b,c).

The S2p spectrum of untreated pyrite shows a major doublet with $2p_{3/2}$ and $2p_{1/2}$ components at 162.4 eV and 163.5 eV with a peak ratio of 2:1. In the case of cleaned pyrite, the sulfate (SO_4) peak is missing, however at 164.4 eV, a minor contribution of oxidized sulfur (SO_x) has appeared (Figure 17, 18a). The results of H_2 treatment are well marked by the S2p spectra with the emergence of monosulfide (S^{2-}) peak of pyrrhotite appearing at 161.25 eV (Nesbitt *et al.* 1998). In the case of N_2-treated pyrite samples, the S^{2-} contribution is minor, however the oxidized sulfur peak is more significant compared to H_2-treated samples (Figure 19c). An additional peak is observed at 168.5 eV reflecting the presence of sulfate species (Lara *et al.* 2015).

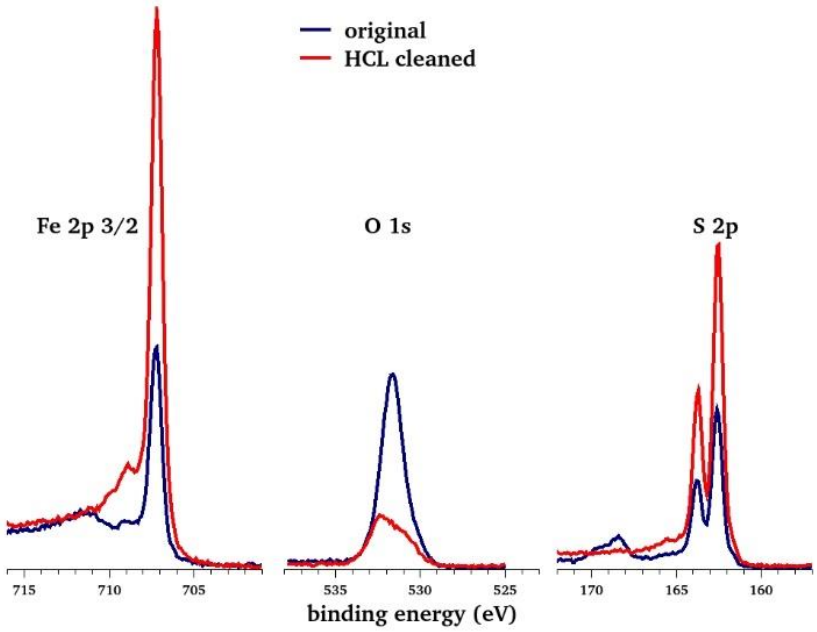

Figure 18. *X-ray photoelectron spectroscopy (XPS) spectra of pyrite stored under atmospheric condition (blue) and after cleaning (red) where binding energies of iron (Fe 2p) oxygen (O 1s) and sulfur (S 2p) are shown.*

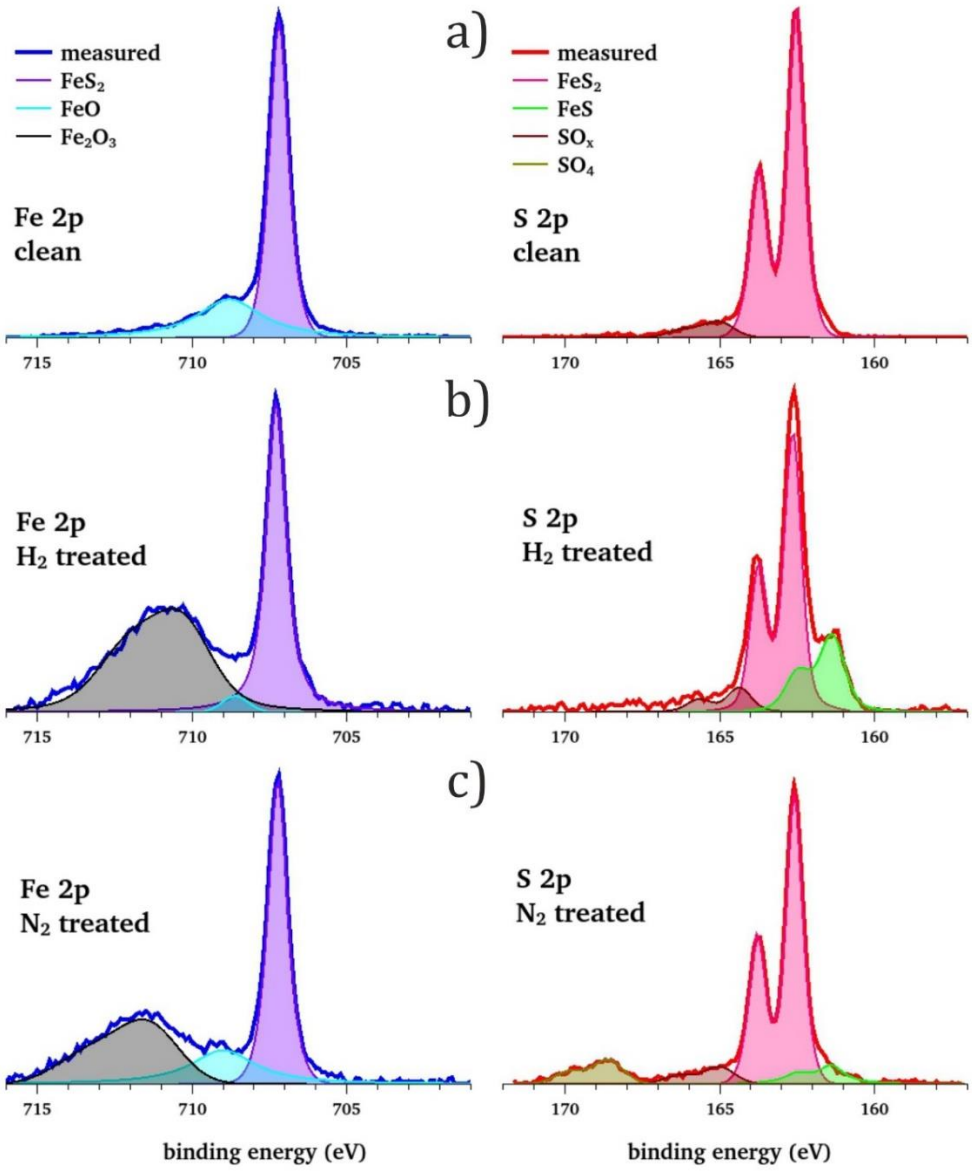

Figure 19. *X-ray photoelectron spectroscopy (XPS) spectra of pyrite surfaces for cleaned (a), H_2-treated (b) and N_2-treated (c) samples. Spectral peaks studied were those for Fe2p and S2p. Peak intensities are rescaled for optimal visibility.*

Angle resolved (ARXPS) measurements were carried out on H_2-treated pyrite samples to determine the location of pyrrhotite. The ARXPS spectra series were evaluated by set up of a model describing the in-depth distribution of components. The model included altered layer above the bulk pyrite crystal. The altered layer consisted of Fe_2O_3 and FeS compounds beside the pyrite (FeS_2). Both the thickness and the composition of the altered layer were estimated by fitting algorithm comparing the measured intensities to the ones yielded by the model. The results are

calculated from the Fe2p and S2p spectrum in a function of angle and give a simple impression about the in-depth composition of Fe and S species in at.% from the upper few nm of the sample. A simple analysis of the spectrum series detected at various angles shows a decrease in the pyrite-related S- and Fe signals at higher angles, whereas the pyrrhotite-related bonds are enhancing with tilting the sample to higher angles (Figure 20). Since high angle detection is more sensitive to the surface region, one can conclude that pyrrhotite is above the pyrite matrix. Model calculation of the pyrrhotite thickness was carried out for 3 observed data series and it resulted in 1.0 nm, 1.6 nm and 3.0 nm values. The relatively large uncertainty in the calculated thickness is attributed to the imperfections on the grain surfaces, which include several planes and macroscopic steps. With changing the angle, these surface irregularities can cause sheltering effect that spoils the ideal angular dependence. The calculation yielded an estimate for the pyrrhotite thickness of 2 +/−1 nm. Assuming a spherical pyrite grain with 50 μm diameter the amount of produced pyrrhotite is 0.02 wt.%.

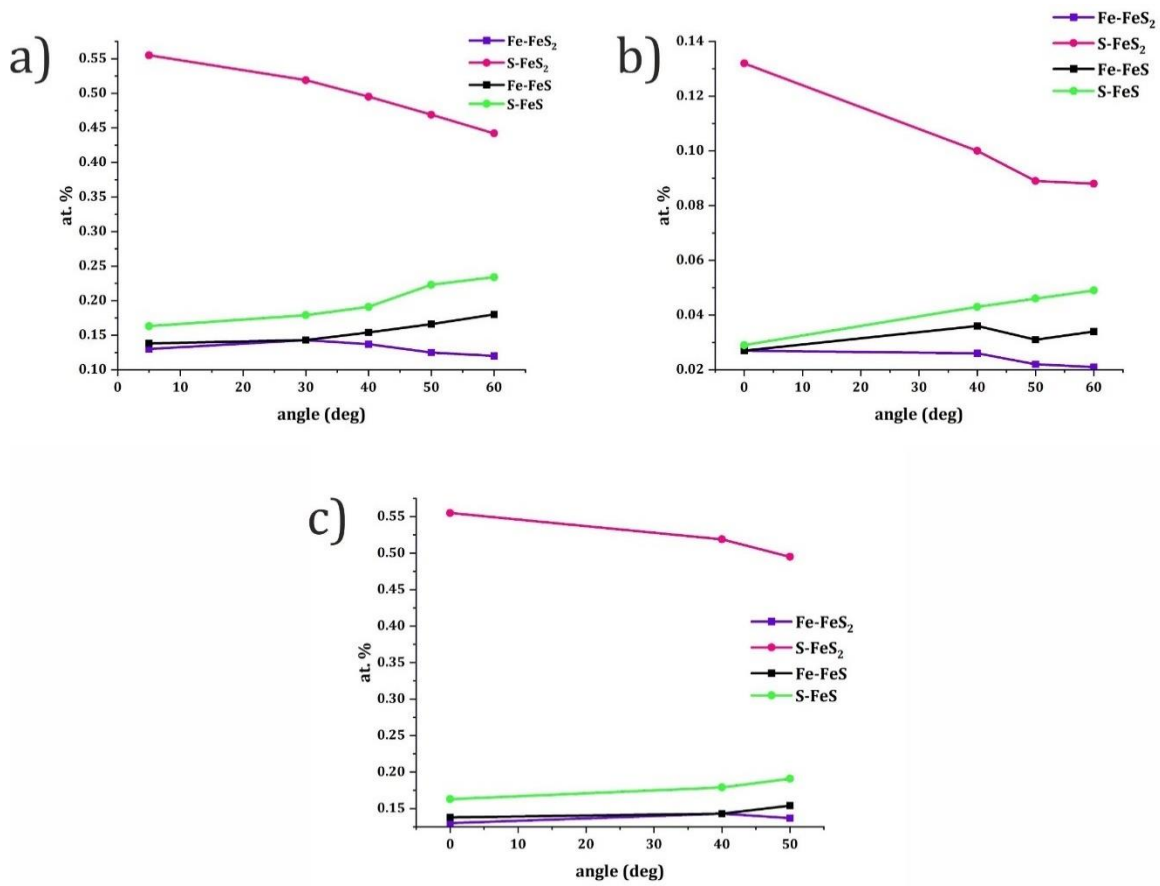

Figure 20. *Angular dependence of pyrite and pyrrhotite components on H_2-treated (Cpv_5 experiment) pyrite surface. Pyrite and pyrrhotite components of Fe and S normalized to concentration (at. %) plotted in the function of emission angle.*

5.3.3. Results of solution chemistry

The results of experiments performed with H_2 show that sulfur concentrations of the solutions are in accordance with the pyrite content. Experiments with 1 wt.% pyrite show the lowest S concentrations which reach the maximum around 24 hour (0.4 mg/L) then a slight decrease can be observed. In cases of 5 wt.% added pyrite, one experiment (Cpv_2) shows continuous but small increase in S concentration while other (Cpv_5) had a maximum at 24 hour (1.2 mg/L) then S started to decrease (Figure 21, Table 14) with the final concentration of 0.7 mg/L. At maximum added pyrite (10 wt.%, Cpv_1), the S curve followed the 5 wt.% pyrite experiment (Cpv_2) trend as it increased slowly but continuously until the end (1.3 mg/L after 75 h) of the experiment (Figure 21, Table 14). During sampling and after reactor opening a characteristic to H_2S smell was

observed evaporating from the solution after all H_2-treated experiments. However, the H_2S was never detected from the gas phase with $CuSO_4$-test.

The S concentrations in reference experiments was higher than with H_2. The N_2-treated experiment has a maximum concentration of S (1.6 mg/L) at 24 h and ended with 1.2 mg/L at 75 h (Figure 21, Table 13). Reference experiment conducted with Ar shows the highest concentration of S (1.8 mg/L) after 3 h and reached with continuous rise a concentration of 2.8 mg/L at 75 h (Table 13). There was no smell of H_2S from the gas phase or evaporating from the solution of the reference experiments.

The calcium concentration shows continuous increase in both cases (H_2, and reference experiments), however with 1 wt.% pyrite the Ca has a plateau after 24 h treatment. The reference experiment with N_2 exhibits similar concentrations to its H_2 pair. Contrastingly, in the Ar-bearing run, more than 2 times higher concentrations were detected (Figure 21).

Kinetic batch modeling results are visualized in Figure 21 and listed in Table 14 and 15. The final Ca concentration is 17.5 mg/L, whereas the sulfur is 5.7 mg/L. The dissolved sulfur is mostly present in HS^- form (1.7×10^{-4} mol/kg), but the least is in H_2S_{aq}. The normed wt.% of minerals after 76 hours are 94.6 wt.% calcite, 5.38 wt.% pyrite and the amount of produced pyrrhotite is 0.02 wt.% in the model with H_2 (Table 14).

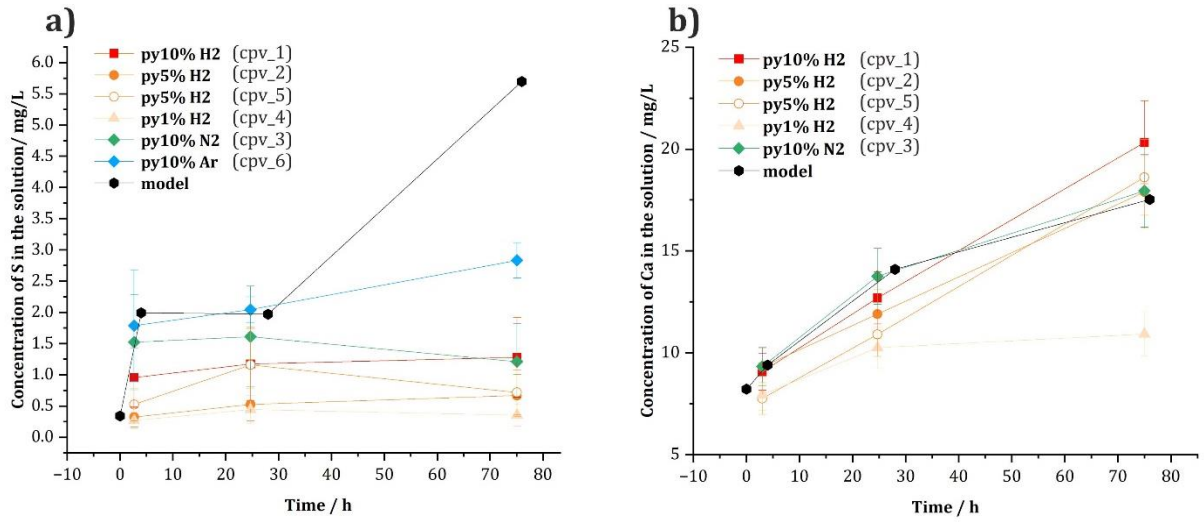

Figure 21. *Comparison of experimental and modeling data of a) S and b) Ca concentration (mg/L) in solution as function of time (h). Black dots indicate the modeled concentrations of 5 wt.% pyrite with H_2 case in the solution*

Table 13. Concentration of Ca and S (mg/L) of solution samples taken during the experiments conducted under 105 °C and 100 bar pressure using hydrogen (H_2), nitrogen (N_2) and argon (Ar). Time expressed as hour, pyrite (py) proportion in wt.%.

ID	**Time (hrs.)**	**Cpv_4**	**(±)**	**Cpv_2**	**(±)**	**Cpv_5**	**(±)**	**Cpv_1**	**(±)**	**Cpv_3**	**(±)**	**Cpv_6**	**(±)**
gas		**H_2**		**H_2**		**H_2**		**H_2**		**N_2**		**Ar**	
py		**1**		**5**		**5**		**10**		**10**		**10**	
Ca	3	8.0	*0.8*	9.3	*0.9*	7.8	*0.8*	9.1	*0.9*	9.3	*0.9*	19.2	*1.9*
	24.7	10.2	*1.0*	11.9	*1.2*	10.9	*1.1*	12.7	*1.3*	13.8	*1.4*	33.8	*3.4*
	75	10.9	*1.1*	17.9	*1.8*	18.6	*1.9*	20.3	*2.0*	17.9	*1.8*	56.1	*5.6*
S	3	0.27	*0.13*	0.32	*0.16*	0.52	*0.26*	0.95	*0.48*	1.52	*0.76*	1.79	*0.89*
	24.7	0.45	*0.22*	0.52	*0.26*	1.16	*0.58*	1.17	*0.59*	1.61	*0.81*	2.04	*0.20*
	75	0.35	*0.18*	0.67	*0.33*	0.72	*0.36*	1.28	*0.64*	1.21	*0.61*	2.83	*0.28*

Table 14. Results of modeling simulations of calcite–pyrite (5 wt.%) - H_2 run. Total dissolved Ca and S are expressed in mg/L whereas solution species and minerals are expressed in mol/kg. The mineral amounts are normed in wt.%.

Time (hrs.)	Ca (mg/L)	S (mg/L)	dissolved HS^- (mol/kg)	dissolved H_2S (mol/kg)	calcite (wt.%)	pyrite (wt.%)	pyrrhotite (wt.%)
0	8.21	0.34	9.05E−06	1.49E−06	94.6	5.40	0.00
4	9.40	1.99	4.84E−05	1.28E−05	94.6	5.40	0.00
28	14.1	1.97	6.00E−05	1.37E−06	94.6	5.40	0.01
76	17.5	5.70	1.72E−04	5.29E−06	94.6	5.38	0.02
152	17.6	5.70	1.72E−04	5.23E−06	94.6	5.38	0.02

Table 15. Results of modeling simulations of calcite–pyrite (5 wt.%) - reference run. Total dissolved Ca and S are expressed in mg/L, whereas solution species and minerals are expressed in mol/kg. The mineral amounts are in normed wt.%.

Time (hrs.)	Ca (mg/L)	S (mg/L)	dissolved HS^- (mol/kg)	dissolved H_2S (mol/kg)	dissolved $CaSO_4$ (mol/kg)	calcite (wt.%)	pyrite (wt.%)	pyrrhotite (wt.%)
0	8.21	3.20	2.21E−05	1.18E−05	7.23E−07	94.6	5.40	5.40E−06
4	9.40	2.34	1.61E−05	4.57E−06	8.22E−07	94.6	5.40	2.58E−03
28	14.0	2.31	1.96E−05	1.44E−06	1.11E−06	94.6	5.40	2.67E−03
76	14.9	2.31	1.96E−05	3.65E−07	1.16E−06	94.6	5.40	2.68E−03
152	14.9	2.31	1.96E−05	3.65E−07	1.16E−06	94.6	5.40	2.68E−03

5.3.4. Integration of experimental and geochemical modeling results for pyrite

The development of sulfur concentration in solution is variable in the experiments. In some cases, S reaches a plateau, in others it starts to decrease over time (Figure 21). This halt of S concentration in the solution samples might originate from technical issues. One limitation is the method of solution sample analyses. Although the solution samples were stored in tightly closed vials, the dissolved sulfur species could evaporate from the solution. Evidence for sulfide evaporation has been observed by the smell of H_2S during solution sampling and after experiments. Another factor of inaccuracy is the reactor material, which can interact with H_2S resulting in thin, black metal (Ni, W, Cr) sulfide layer formation at the surface of the steel. The same phenomenon was noted by Truche *et al.* (2009) and Zhang *et al.* (2021). The wall of the reactor served as nucleation for metal sulfides. Thus, the accurate evaluation of released sulfide was not possible from experiments. However, the evolution of dissolved Ca could be a concomitant indicator of sulfide release because calcite dissolution is pH dependent and attributed to sulfide in the solution lowering the pH. In the case of lowest pyrite concentration (1 wt.%), which is the most representative for reservoir share, the Ca concentration reaches a plateau around 11 mg/L (Figure 21, Table 13), which is supposing the negligible contribution of pyrite dissolution by hydrogen.

The modeling predictions of Ca concentration match the results of the experiments. To compare results presented in this PhD with the previous experimental studies the reductive dissolution of pyrite was investigated by Truche *et al.* (2010) under 8 to 18 bar H_2, 90 to 180 °C and by Spietz *et al.* (2022) under 38 °C. The later study determined the lower limit of H_2 concentration (1.98×10^{-4} M) for the reaction to take place (Spietz *et al.* 2022).

The reference experiments were performed with 10 wt.% pyrite and N_2 (Cpv_3) showing similar Ca and S concentrations as H_2 experiment (Figure 21). In this case, anaerobic pyrite oxidation is expected at neutral pH which can be described by the following reaction (Neculita *et al.* 2007).

$$FeS_{2(s)} + \frac{7}{2}O_2 + H_2O \rightarrow Fe^{2+} + 2SO_4^{2-} + 2H^+ \quad (2)$$

Interestingly, in the Ar-bearing run (Cpv_6), S concentration exceed the hydrogen-bearing experiments by a factor of 2 or 3, and Ca concentration is also elevated compared to the hydrogen-bearing run. In reference experiments, neither reduced sulfur precipitation on reactor wall nor H_2S production was expected; therefore, the measured sulfur concentrations from the solution samples are considered to be accurate.

5.3.5. Discussion on pyrite surface

Those grains that have undergone cleaning procedure are characterized by only sulfide peaks as well as showing clean unoxidized surfaces (Figure 16b) under optical microscope confirming the effectiveness of sample preparation (Figure 16, 18). The pyrite grains after H_2-treatments show alteration in the form of brown patches (Figure 16c), and increased surface roughness. The density and distribution of surface pitting was variable from grain to grain. In general, the greater the proportion of pyrite in the experiments, the more intense the alteration observed on the pyrite surfaces.

Altered patches and clumps have patchy distributions which may suggest that the pyrrhotite can occur on reactive sites of high excess surface energy, e.g., lattice defects, cleavages, and fractures (Figure 15c). Liu *et al.* (2021) proved that on the 2 1 0 surface of pyrite, sulfur can be removed easier than that from other surfaces e.g., (100) (Alonso-Vante *et al.* 1988).

The SEM-EDS measurements on the brown patches (Figure 17) referred to iron and sulfur composition with an average Fe/S atomic ratio of 0.88, suggesting pyrrhotite composition, whereas 0.52 was calculated on the clear pyrite surface (Table 12). These Fe/S ratios are in accordance with those in Truche *et al.* (2010, 2013) and Mosser-Ruck *et al.* (2020), who also used SEM to analyze mineral precipitates after pyrite-H_2 interaction.

Stronger evidence of pyrrhotite appearance is demonstrated by XPS analyses (Figure 18,19b). The angle resolved XPS proved the overlayered nature of pyrrhotite by the decrease in the pyrite-related S- and Fe-signals at higher angles, whereas the pyrrhotite-related bonds are enhanced with tilting angle (Figure 20). Since high angle detection is more sensitive to the surface region, it can be inferred that pyrrhotite is above the pyrite matrix. Model calculation of the pyrrhotite thickness was carried out for 3 observed data series and it resulted in 1.0 nm, 1.6 nm and 3.0 nm values. The relatively large uncertainty of the calculated thickness is attributed to the imperfection of the grain surfaces, which included macroscopic steps as well. With changing the angle, the sheltering effect influences the observed angular dependence. Therefore, it can be concluded that the calculation yielded from the ARXPS measurements of this PhD provides an estimate for the pyrrhotite thickness of 2 +/−1 nm. Projecting this quantity to the total material amount involved in the experiments and assuming spherical pyrite grain with 50 µm diameter the amount of produced pyrrhotite is 0.02 wt.%.

5.3.6. Relevance of results on pyrite for underground hydrogen storage

In reservoir rocks pyrite concentration is typically around 1 wt.% and in caprocks it is usually below 5 wt.% (Table 16). The presence of pyrite has not posed significant problems for hydrocarbon production and natural gas storage (Perera 2023), in the context of underground hydrogen storage, however, the pyrite–H_2 interaction not only changes the solution chemistry and gas composition but could also modify the mineral assemblage of reservoir rock and may affect its structural integrity, porosity and permeability. The main question is the extent of the reaction. The geochemical reactions in the kinetic batch model results of this PhD reach a plateau after 76 hours (Table 14, 15) and the normed wt.% of minerals are changed from the initial 95 wt.% and 5 wt.% to 94.6 wt.% and 5.4 wt.% for calcite and pyrite, respectively (Table 14) as a consequence of H_2 exposure that can be characterized as insignificant modification.

Experimental conditions in this PhD study, which simulate underground hydrogen storage temperature and pressure (under 105 °C and 100 bar) are challenging to compare with the limited previous studies on reductive pyrite dissolution due to the variations in experimental setups. Truche *et al.* (2010) conducted experiments between 90 to 180 °C with hydrogen partial pressure ranging from 0 to 18 bar, where the reductive dissolution of pyrite was remarkable between 120-180 °C and at higher H_2 partial pressure (18 bar). Spietz *et al.* (2022) determined the lower limit of H_2 concentration (1.98×10^{-4} M), at which abiotic pyrite reduction is expected to take place. It can be concluded that in a wide range of temperature (38-180 °C) and pressure (30-100 bar) conditions the pyrite reduction to pyrrhotite by hydrogen is expected to occur in pyrite bearing reservoir rock or caprock. Both XPS and geochemical modeling calculations indicate 0.02 wt.% of pyrrhotite precipitation in a simple calcite dominated system with 5 wt.% pyrite (Table 14). The byproduct H_2S can affect the quality of produced gas, material integrity, safety, and health making gas treatment a necessity even at concentrations of 10-20 ppm (Thiyagarajan *et al.* 2022). The modeling results of this PhD show 0.18 ppm H_2S_{aq} after 76 hours of H_2 exposure (Table 14) and no H_2S appeared in the gas phase. These findings, along with the amount of pyrrhotite, suggests that the impact on the purity of the injected H_2 gas is moderate. Regarding the porosity changes induced by the pyrite-H_2 interaction, the molar conversion from pyrite (24 cm^3/mol) to pyrrhotite (19 cm^3/mol) gives 21% reduction in molar volume. However, the shape and size of newly formed pyrrhotite (Figure 16c, 17) in the experiments of this PhD suggest that it has increased specific surface area, therefore its precipitation could reduce the pore space.

Table 16. Sedimentary rock formations (reservoir sandstones and caprocks) from various locations worldwide and their pyrite content (in wt.%).

Formation	Type	Location	Pyrite content (wt.%)	Reference
Brent Group Etive	sandstone	Statfjord North Sea (Norway, UK)	1.8	(Harris 1992)
Brent Group Ness	sandstone		0.7	
Brent Group Tarbert	sandstone	Hutton North Sea (UK)	0.2	
Brent Group Rannoch	sandstone	Lyell North Sea (UK)	2.0	
Szolnok Sandstone Formation	sandstone	Pannonian basin (Hungary)	<1	(Gelencsér *et al.* 2024a)
Szolnok Sandstone Formation	sandstone	Pannonian basin (Hungary)	0.4	(Laczkó-Dobos *et al.* 2020)
Puchkirchen and Hall formations	sandstone	Molasse basin (Austria)	1	(Hassannayebi *et al.* 2019)
Barnett Shale Formation	shale	Forth Worth Basin TX, US	2-5	(Bernard *et al.* 2012)
Eagle Ford Formation	shale	East Texas Basin TX, US	5	(Mullen 2010)
Callovian– Oxfordian Formation	shale	Paris Basin (France)	1-2	(Truche *et al.* 2013)
Yanchang Formation	shale	Ordos Basin (China)	1.9	(Hou *et al.* 2022)

5.4. Results and discussion of injection simulation on Öcsöd reservoir rock

5.4.1. Petrography of Öcsöd samples

In general, samples from both wells (Öcsöd-1 and OGD-Öcsöd-K-2) are composed of detrital grains such as quartz, mica (muscovite), feldspar. Core sample from Öcsöd-1 is representative of fine and very fine-grained sandstone. Samples contain detrital grains, usually sub-rounded or well-rounded silicates (quartz and feldspar). Quartz is the dominant mineral phase. Muscovite flakes are often oriented. Carbonates occur as individual grains (calcite, dolomite) and cement (Figure 22). Pale green chlorite fragments as individual grains and framboidal pyrite were also identified in subordinate amounts.

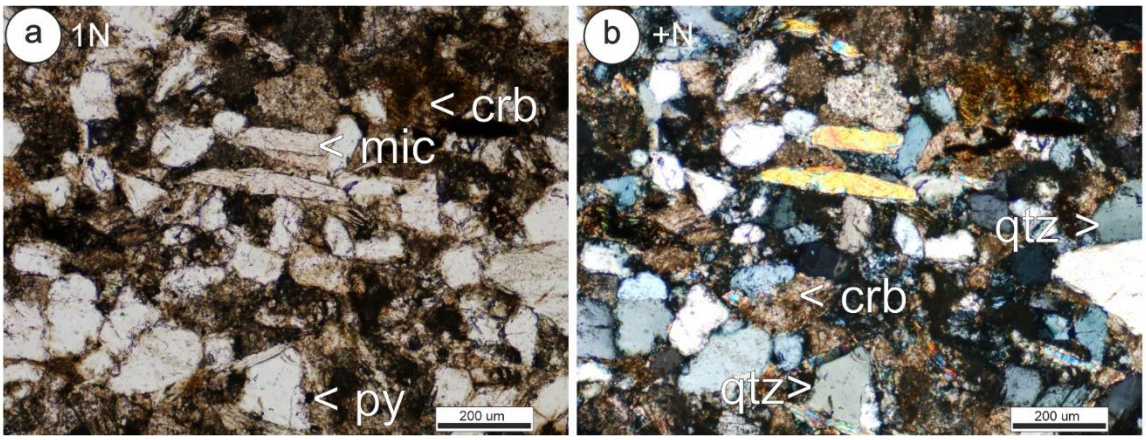

Figure 22. *Textural overview of sandstone sample from Öcsöd-1 drill taken under plane polarized light (a) and cross polarized light (b). crb: carbonate, mic: mica, py: pyrite, qtz: quartz.*

The OGD-Öcsöd-K-2 cutting samples are characterized by coarse to fine-grained sandstones. Generally, both types of sandstones have similar mineralogical composition. They consist of translucent silicates (quartz and feldspars), carbonates (calcite, dolomite) (Figure 23). The secondary carbonate occurs as overgrowth at grain boundaries and enriched in iron, which can be defined as ankerite. Tiny pyrite clusters can be observed in all studied cuttings.

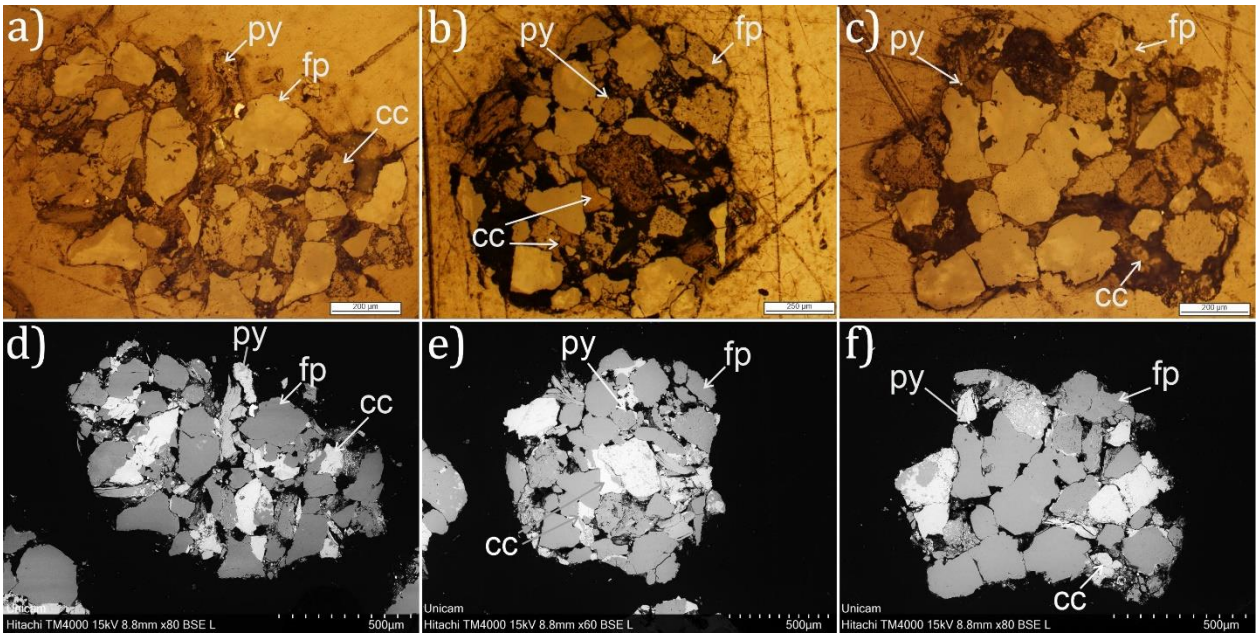

Figure 23. *Photomicrographs and scanning electron microscopic (SEM-EDX) images with backscatter mode) of cuttings samples from OGD-Öcsöd-K-2 well. The upper photos were taken under reflected light. py: pyrite, fp: feldspar, cc: calcite*

5.4.2. Results of X-ray diffraction analysis from Öcsöd-1 and OGD-Öcsöd-K-2 wells

Based on the X-ray diffraction analysis on disoriented sample from Öcsöd-1 well, the most abundant mineral phase is quartz (49 wt.%). Plagioclase, showing albite structure, is the second abundant silicate with 10 wt.%. Carbonates consist of calcite (13 wt.%), dolomite (10 wt.%) and ankerite (3 wt.%). Clay minerals, such as illite/muscovite, chlorite, kaolinite are also present with concentrations of 9 wt.%, 2 wt.%, 4 wt.%, respectively (Figure 24). Cuttings from OGD-Öcsöd-K-2 were also measured with XRD, but since cuttings were mixed with drilling mud and were also washed out, only semi-quantitative result can be presented. The three depth intervals (ranging between 2101 m and 2110 m) are consistent in mineralogy. The most dominant mineral phase (denoted by +++) is quartz followed (denoted by ++ down to +/-) by calcite, dolomite, mica/illite and plagioclase. Additionally, K-feldspar and kaolinite were identified in subordinate amounts (Table 17).

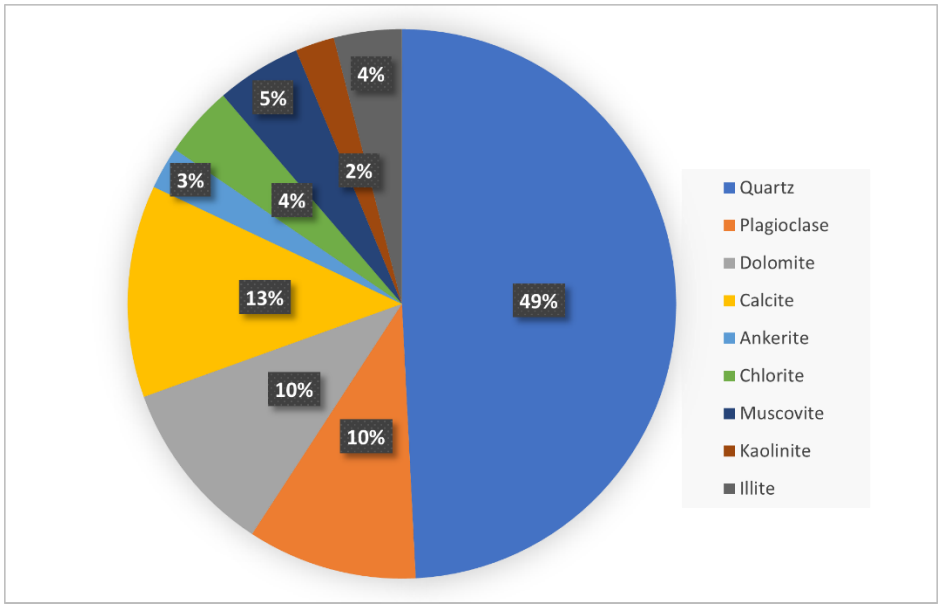

Figure 24. *Results of XRD analysis on Öcsöd-1 drilling core sample in wt.%.*

The minor differences between the depth intervals suggest that they originate from the same reservoir rock and the XRD data provide a solid base for petrographic observations.

Table 17. Qualitative mineral composition of OGD-Öcsöd-K-2 drill cuttings from 3 depth interval covering 2101-2110 m measured depth.

OGD-Öcsöd-K-2	quartz	calcite	dolomite	plagioclase	k-feldspar	chlorite	kaolinite	mica	illite	barite
2101-4 m	+++	++	++	++	+	++	+/-	++	+	+/-
2104-7 m	+++	++	++	++	+	++	+/-	++	+	+/-
2107-10 m	+++	++	++	++	+	++	+/-	++	+	+/-

5.4.3. Results of electron microprobe analyses (EMPA) on carbonates and feldspars

Electron microprobe analyses (EMPA) were carried out on OGD-Öcsöd-K-2 cuttings to reveal detailed chemical composition of carbonates and feldspars of the reservoir rock with the aim to refine geochemical models. Calcite of the reservoir rock is mostly pure $CaCO_3$, some grains having slight (less than 0.5 wt.%) FeO content. Dolomite grains have Fe-free core and they rim is characterized by ankerite composition with varying Fe-content in a wide range (Figure 25a).

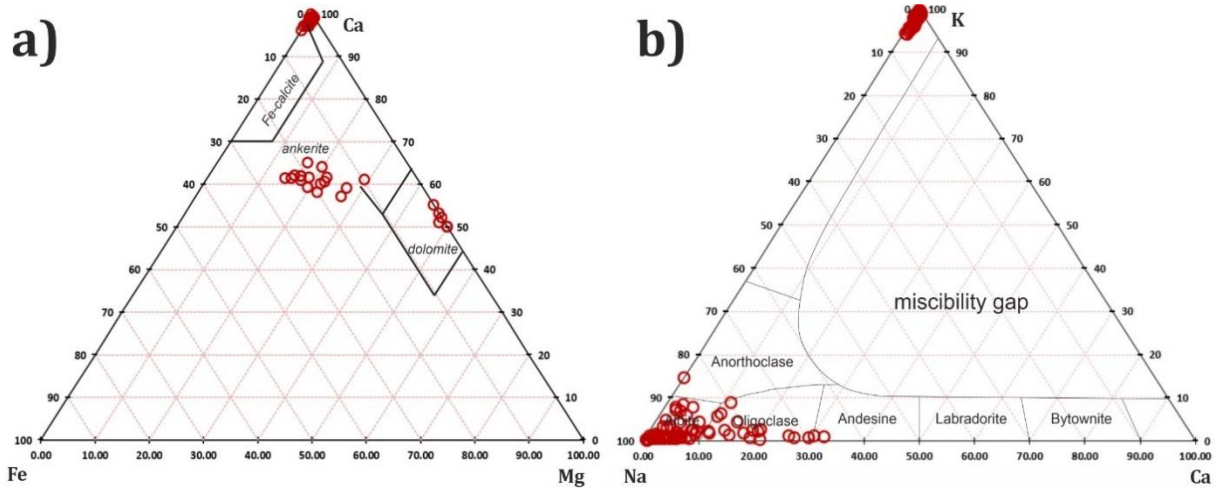

Figure 25. *Chemical composition carbonates and feldspars of the cutting samples studied from the OGD-Öcsöd-K-2 well. a) Chemical composition of carbonate minerals normalized to 100% of the three end-members (calcite, siderite, magnesite). Fields of the diagram are according to Chang et al. 1996). The figure is based on the data in Table A.10.6.1. b) Chemical composition of the feldspars of reservoir rocks. Feldspar composition is normalized to 100% of the three major end-members (orthoclase - K, albite - Na, anorthite - Ca). The figure is based on the data in Table A.10.6.2.*

Feldspars of OGD-Öcsöd-K-2 cuttings were also subjected of chemical analysis to observe the distribution of K-Na and Na-Ca in the second dominant silicate group of the reservoir rock. The albite component of K-feldspar varies within a narrow range (0-7%). The measured plagioclase compositions predominantly fall within the albite field (Ab_{90-100}) but also extend to compositions ranging from anorthoclase to andesine (Figure 25b).

5.4.4. Results and discussion of equilibrium modeling – injection simulation in Öcsöd reservoir

Equilibrium geochemical modeling was applied with the aim to detect long-term geochemical effect of hydrogen injected to the sandstone reservoir – the object of this study. This geochemical model benefited from the experimental part of this study, by the use of modified database.

The most significant changes are related to the pyrite–H_2 interaction (Figure 26). Less important changes are associated with carbonates. Carbonate dissolution could be an indirect consequence of hydrogen injection because carbonates are pH sensitive and pyrite dissolution can lower the pH of the porewater. Overall, the most remarkable effect of hydrogen injection is related to the reductive dissolution of pyrite. Considering the results of combined experimental and kinetic modeling work of this PhD research, the pyrite dissolution and accompanying H_2S production is dependent on the original pyrite content of the rock (Gelencsér *et al.* submitted1).

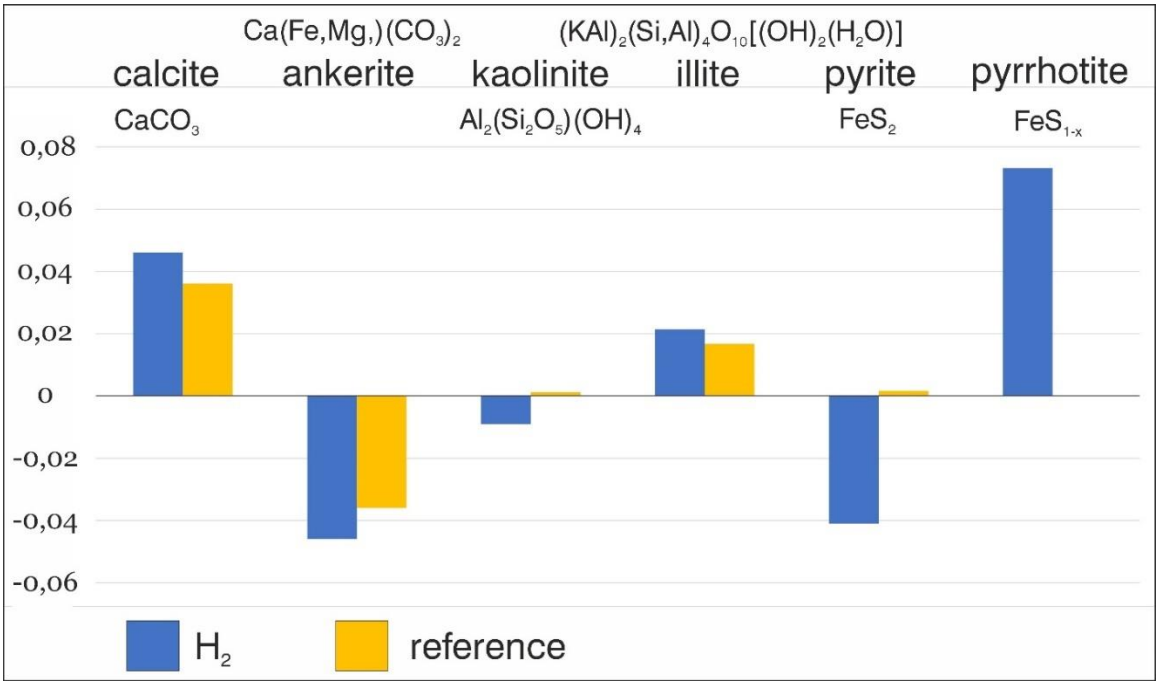

Figure 26. *Results of equilibrium geochemical models with H_2 (blue) and without H_2 (yellow) of Öcsöd reservoir. The positive values represent mineral precipitations whereas negative values indicate the dissolution of the mineral phases.*

5.5. Overview on hydrogen storage potential of the Pannonian basin system

5.5.1. Pannonian basin (central part)

The Pannonian basin system with its geological resources displays a positive potential to the challenges of energy transition. The most promising areas for natural gas storage are already investigated by European projects, which are supported by historic records of successful decades-long natural gas (NG) storage (Cavanagh *et al.* 2023). Preliminary assessment of HyUSPRe report considered 11 storage sites in the central part of the Pannonian basin system as of today which are all depleted gas fields (Figure 27, Table 19).

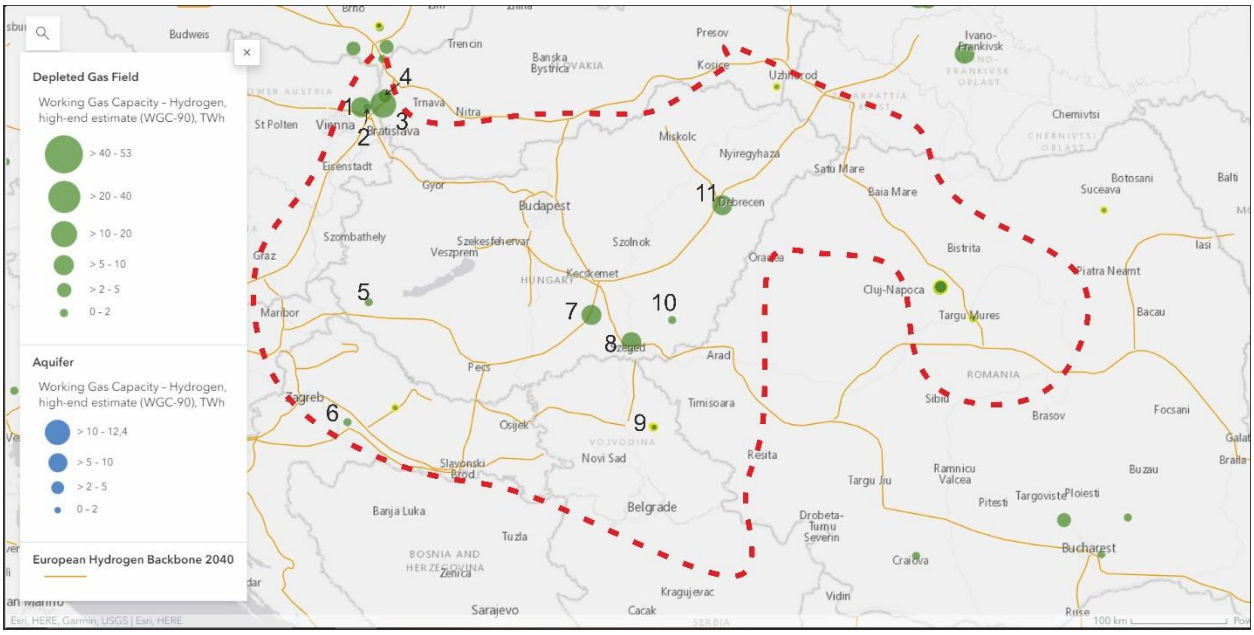

Figure 27. *Existing natural gas storage sites with potential for underground hydrogen storage (UHS) from HyUSPRE report (Yousefi et al. 2022) from the Pannonian basin system (red dashed contour line). The depleted gas fields (DGF) are highlighted in green. Aquifers (AQU) in blue; the circle size shows the hydrogen storage capacity of the reservoirs. The orange pipeline represents the European Hydrogen Backbone initiative predicted for 2040. Planned sites are ringed in yellow. Locations: 1: Schönkirchen Reyersdorf (AT), 2: Tallesbrunn (AT), 3-4: Láb Complex (SK), 5: Pusztaederics (HU), 6: Okoli (HR), 7: Zsana (HU), 8: Szőreg-1 (HU), 9: Banatski Dvor (RS), 10: Kardoskút (HU), 11: Hajdúszoboszló (HU).*

Table 18. Available information about existing gas storage sites of Pannonian basin system, based on HyUSPRe report (Cavanagh *et al.* 2023). Data includes reservoir lithology, porosity (Φ) in %, working gas capacity calculated for natural gas (WGC-NG) and for hydrogen (H_2) in TWh for lower estimate (l.e.) and higher estimate (h.e.).

ID	Location	Rock types	Φ (%)	Year of operation	WGC-NG (TWh)	H_2 capacity (TWh) l.e.	H_2 capacity (TWh) h.e.	Reference
1	Schönkirchen-Reyersdorf (AT)	Dolomite	-	1977	20.72	5.18	6.18	(Welkenhuysen *et al.* 2016)
2	Tallesbrunn (AT)	Turbiditic sandstone	30	1974	4.52	1.13	1.25	(Fuchs and Hamilton 2006)
3 - 4	Láb Complex (SK)	Sandstone beds intercalated with greenish, grayish, and dark-gray micaceous aleuropelites	-	1997	36.5	9.13	10.95	(Kováč *et al.* 2004; Hladik *et al.* 2017)
5	Pusztaederics (HU)	Sandstone bounded with clay marl and marl	-	1979	3.8	0.95	1.08	(Megyery *et al.* 2000)
6	Okoli (HR)	Turbiditic sandstone	13-18	1988	5.22	1.31	1.57	(Baric *et al.* 2000)
7	Zsana (HU)	Limestone with > 98 wt.% calcite	23.5	1996	24.26	6.06	6.63	(Jalalh 2006)
8	Szőreg (HU)	Siltstones, coalified plant fragments, coarse grained yellowish sandstone with lamination or massive structureless development. Syngenetic clay and carbonates	19.23	2009	20.11	5.03	6.03	(Szilágyi and Geiger 2012)

		are also observed. Horizontal bedding, lamination are characteristic sedimentary structures						
9	Banatski Dvor (RS)	Sandstone	-	2024	2.52	0.63	0.76	(Jorovic 2009)
10	Kardoskút (HU)	Turbiditic sandstone formed by gravitational sliding and prograding delta cycles	~30	1978	3.13	0.78	0.92	(Bárány *et al.* 2013)
11	Hajdúszoboszló (HU)	Friable sandstone with significant quartzite content	28.8	1981	18.33	4.58	6.11	(Jalalh 2006)

Most of the depleted gas fields in the central part of the Pannonian basin system such as Tallesbrunn, Láb Complex and Okoli are composed of sandstone (Figure 27, Table 19). Exceptions are the Schönkirchen-Reyersdorf and Zsana sites where dolomite and limestone are the reservoir rocks respectively (Jalalh 2006; Welkenhuysen *et al.* 2016). These reservoirs are seated between 500 and 2500 m depth (Cavanagh *et al.* 2023). The less information is available about Banatski Dvor which is the latest operating storage site (Brikić 2024) (Table 19). Supposing the mineralogy of the siliciclastic storage sites listed above (Table 19) is similar to that of the Öcsöd reservoir (Figure 24), they might be suitable for hydrogen storage from an abiotic reactions' perspective. As for the carbonate hosted reservoirs, the conclusion of calcite experiments of this study is applicable, suggesting that hydrogen should not assume significant reactions with the calcite, however, further detailed experimental and geochemical modeling study is recommended on these reservoirs.

Besides the conventional DGF sites in the Pannonian basin system, based on the recent knowledge about the geological criteria of UHS, there are other rock types, which may also serve as hydrogen

storage sites in the future, for example volcanic sediments. Kiss *et al.* (2019) made extensive research based on potential field data and showed that at the Nyírség area (Northern Hungary) (Figure 4) consist of 5 km thick Miocene volcanic sediments with high porosity (20% in average) are dominant below 1-1.5 km. Alteration of hundreds of meters thick pyroclastic and lava rocks (rhyolite and andesite) overlain by Late Miocene deltaic and fluvial sediments can be found in this area based on seismic profiles and borehole data (Petrik *et al.* 2019). Although there is no detailed information about the traps and the sealing properties of overlying sediments, the large volume porous rocks might be worth taking further consideration for detailed study.

5.5.2. Transylvanian basin

Although Transylvanian rock salt deposits have not been considered as potential storage formation for hydrogen by previous studies (Iordache *et al.* 2014; Caglayan *et al.* 2020), microstructural data (Table A.10.5.1) evaluated in this PhD study make the Praid rock salt comparable to creep studies of cavern convergence. Salt diapirs in Transylvanian basin are in large number along the eastern and western diapir alignments (Figure 6) with identical origin, deformation history (Krézsek and Bally 2006) and rock salt characteristics, which might be suitable to utilize as UHS sites (Gelencsér *et al.* 2024b).

Creep laws defining deformation rate for rock salt provide essential data for modeling salt flow and solution mining of salt caverns and closure of mine cavities and wellbores (Ma *et al.* 2021; Lankof *et al.* 2022). One of the common deformation mechanisms in rock salt is the dislocation creep when the crystal distorts by slip along one or more weak crystallographic directions or slip planes, where the lattice is weakly bonded (Jackson and Hudec 2017). On the other hand, solution precipitation creep was observed under long-term deformation conditions. In naturally deformed salts both dislocation creep and solution precipitation creep should be taken into account as deformation mechanisms.

First assumption on salt deformation in the context of salt cavern mining was made by Allen et al. 1982. For seasonal energy storage, the 10% strain limitation of the rock salt structure is estimated (Allen *et al.* 1982; Matos *et al.* 2019). Measured strain rates as relevant for the ongoing current deformation of the salt in Praid (eastern part of the Transylvanian basin) could be acceptable, but more microstructural analysis is necessary for more robust assessment of the salt diapir.

More recently, a threshold level for pressure solution creep has been applied in cavern models by Van Oosterhout *et al.* (2022). They concluded that the flow stresses in natural rock salt are higher

than the threshold stress derived by them (0.07-0.90 MPa), confirming that pressure solution creep can operate in natural rock salt above the calculated threshold. Below this threshold, the strain rates decrease from ~10^{-13} to 10^{-18} s^{-1} and the dislocation creep remains as operating deformation mechanism. In the Praid rock salt, the calculated differential stress falls between 1.8 and 2 MPa and strain rate calculations (total strain rate between 1.2 and 1.3×10^{-10} s^{-1}) suggest relatively fast movements in the diapir body (Gelencsér *et al.* 2024b). These values are above the threshold defined by Van Oosterhout *et al.* (2022) raising concerns about the safe cavern mining in this area. Above all, there are several protected areas hosting active mining and tourism activities, in these locations underground hydrogen storage is not considered as a realistic project in the near future.

6. Theses of the doctoral study

1. I defined an experimental process suitable for studying the effect of hydrogen on minerals under subsurface storage conditions. I also built kinetic models, which results are comparable with those of experiments. This combination of geochemical modeling and experimental work is a more effective way to predict hydrogen behavior than using only geochemical modeling. I stated that modifications of geochemical model databases backed by experimental results are recommended to better constrain the abiotic carbonate-hydrogen reactions in the models, since underground hydrogen storage should generally not assume significant interactions with carbonates (Gelencsér *et al.* 2023).

2. Through experimental work with calcite, I confirmed that very limited extent of calcite dissolution is expected under high pressure (100 bar) hydrogen at 105 °C. These results contrast with previous studies, which, based solely on geochemical modeling, predicted significant hydrogen loss and mineral dissolution induced by the reaction of carbonate minerals with hydrogen. My results suggest that carbonate-bearing geological formation should not be excluded from consideration for underground hydrogen storage (Gelencsér *et al.* 2023).

3. I conducted a series of experiments and kinetic modeling with K-feldspar mineral representative of real rock-forming constituents to study the significance of K-feldspar in the reservoir rocks in underground hydrogen storage. The experimental work of this PhD revealed limited effect of hydrogen on K-feldspar compared to reference experiments with nitrogen. However, this effect manifested in an increased release of potassium and the formation of aluminum-bearing phase, compared to reference experiments. Based on the changes in the chemical composition of the solution, this process can be explained by an enhanced exchange reaction between hydrogen and alkali ions at the mineral surface. Subsequently, the Al–O bonds and Si–O bonds are also breaking down, which is followed by the formation of Si-rich precursor complex. In the context of a polymineralic subsurface reservoir environment, the results of this PhD may suggest that hydrogen injection can slightly enhance K-feldspar dissolution, hence supplying ions for secondary mineral precipitations (Gelencsér *et al.* 2024c).

4. To better understand the pyrite reactivity under hydrogen storage conditions, I designed a more complex experimental setup, building on the experience I gained from studying the other two minerals (i.e., calcite, K-feldspar). In particular, a mixture of calcite and pyrite (with 1 to 10 wt.% pyrite) was reacted with hydrogen, representing a typical range of pyrite content in sedimentary rocks. Beyond the well-established procedures of optical microscopy and scanning electron microscopy, I successfully utilized X-ray photoelectron spectroscopy (XPS) to study chemical changes on pyrite induced by hydrogen. The XPS measurements on pyrite surface revealed that pyrrhotite forms on the surface of the pyrite due to the hydrogen treatment. In the reference experiments, pyrrhotite formation was not observed. With angle-resolved XPS measurements I determined the thickness of the pyrrhotite growth on pyrite surface. Calculations give an average of 2 nm, with an error margin of +/−1 nm. This result implies that about 0.02 wt.% pyrrhotite precipitation is expected in system with 5 wt.% pyrite content on a 50 µm-size pyrite grain due to 76-hour H_2 exposure Kinetic geochemical modeling was in complete agreement with my experimental results. Regarding the associated production of hydrogen sulfide, geochemical modeling results indicate that it remains in the solution rather than going to the gas phase under reservoir conditions (105 °C, 100 bar) (Gelencsér *et al.* under rev.2).

5. Hydrogen injection simulation with reservoir parameters of Öcsöd hydrocarbon field indicates subordinate effect of hydrogen on mineral dissolution and precipitation in the reservoir (Gelencsér *et al.* 2024a). Considering the high availability of the studied reservoir rock type, the geological characteristics of the Pannonian basin system are favorable for underground hydrogen storage due to the large volume of porous rocks including several depleted gas fields (Gelencsér *et al.* under rev.1). However, further detailed experimental control is necessary for geochemical modeling. Additionally, the Transylvanian basin has hydrogen storage potential in evaporites as well, which are geochemically neutral with hydrogen. However, the structural stability of salt occurrences in the region could be a geological risk, which needs further analysis (Gelencsér *et al.* 2024b).

Epilogue

The major goal of my PhD research was to investigate possible abiotic reactions between rock forming minerals and hydrogen under subsurface storage conditions. This included a combined experimental and geochemical modeling study on three common mineral constituents of sedimentary rocks. Geochemical modeling was also applied to a natural gas reservoir to predict the long-term effects of hydrogen storage on reservoir mineralogy. The result of hydrogen-induced reactions with sedimentary rock constituents and microstructural results on Transylvanian rock salt was also put in the regional geologic context. These results have been published, contributing to scientific and technical reports, and have laid the groundwork for further theoretical and experimental studies evidenced by 32 independent citations. Additionally, a major goal of the PhD research was to build up a hydrogen laboratory facilitating more advanced geo-storage research. My 4-year period resulted in several fruitful cooperations with universities (Budapest University of Technology and Economics, Hungary, Karlsruhe Institute of Technology, Germany, Auburn University, US), research institutes, (HUN-REN Centre for Energy Research, Hungary, GFZ German Research Centre for Geosciences, Germany), and industrial partners (O&GD Central Ltd., Hungary and OMV, Austria).

Overall, I feel fortunate to have been at the forefront of a hydrogen-related environmental research and contributed to the development of new technologies in response to global challenges like energy transition, which are shaping the future of environmental earth sciences.

7. English summary

In the age of energy transition, the Carpathian-Pannonian region can optimistically look forward to utilizing its geologic resources. The application of power-to-gas technology in the region seems to be promising since the major underground hydrogen storage sites are attributed to depleted gas fields in siliciclastic sedimentary rocks. Due to the hitherto little knowledge on rock-water-hydrogen interaction, the basic lab experiments and geochemical modeling hand in hand provide an ultimate step forward in technological advancement.

In this doctoral study rock-forming mineral behavior under high pressure hydrogen in aqueous environment (100 bar, 105 °C) was investigated with several analytical techniques. The geochemical modeling part benefited from the experimental work.

The calcite-water-H_2 experiments concluded the non-reactive behavior of calcite. In the K-feldspar–water–H_2 system, the H_2 injection can slightly increase the release of K and Na and the formation of Al-bearing phases.

Pyrite, the common accessory mineral of sedimentary rock, is the most reactive among the minerals investigated in this study. Pyrite can dissolve in the presence of high pressure H_2 as a result of redox reaction and pyrrhotite forms on pyrite surface. Geochemical modeling predictions and XPS based calculation of the pyrrhotite production led to identical results. Approximately 0.02 wt.% pyrrhotite precipitation is expected as a consequence of H_2 exposure. This study was the first application of XPS on changes taking place on mineral surfaces under subsurface hydrogen storage.

Hydrogen injection simulation in Öcsöd site indicates subordinate effect of hydrogen on mineral dissolution and precipitation in the reservoir. The most remarkable process is the reductive dissolution of pyrite. However, this reaction is insignificant until pyrite is only an accessory (< 1 wt.%) in the bulk rock composition. The knowledge on hydrogen induced geochemical reactions within sedimentary rocks, gained in this PhD, gives a solid base for further, more complex (biotic, reactive transport) studies. As for the Transylvanian rock salt, the available microstructural data suggests a potentially acceptable deformation rate for further hydrogen storage plans, however more detailed study is needed to make decisions. Considering the large and wide distribution of the rock-type of the studied location, the Pannonian basin with its subbasins is a promising place for energy storage by power-to-gas technology.

8. Magyar nyelvű összefoglaló

Korunk energetikai átmenete még sok bizonytalanságot tartogat, azonban a Kárpát-Pannon régió természeti erőforrásait figyelembe véve, a „power-to-gas” technológia alkalmazása ígéretesnek tűnik. A Pannon-medencében jelentős mennyiségű sziliciklasztos üledékes kőzet található, amely alkalmas lehet a felszín alatti gáz tárolásra, így pl. hidrogén tárolásra is. A hidrogén által kiváltott geokémiai reakciók megismerésének a kezdeténél tartunk. Ezért a doktori dolgozatban a kőzet-víz-hidrogén kölcsönhatások megértéséhez laboratóriumi, ún. „áztatásos” kísérleteket és geokémiai modellezést végeztem, amelyekhez számos analitikai módszert alkalmaztam beleértve hagyományos és a nem rutinszerű röntgen-fotoelektron spektroszkópia (XPS) technikát is. A dolgozatban a kőzetalkotó ásványok viselkedését vizsgáltam vizes környezetben felszín alatti hidrogéntárolás körülményei között (100 bar hidrogén, 105 °C). A geokémiai modellezést a kísérletek alapján ellenőriztem és kiegészítettem.

A kalcit–víz–H_2 kísérletekből a kalcit nem reaktív viselkedésére következtettem, amely eredmény cáfolja a korábbi, geokémiai modellezésen alapuló, karbonátos kőzetekre vonatkozó megállapításokat. A káliföldpát esetében a kísérletek és a geokémiai modellezési eredmények azt mutatják, hogy a hidrogén kis mértékben elősegítheti az ásvány oldódását, ezáltal a K és Na felszabadulását, egyúttal feltehetően Al-tartalmú ásványfázis kicsapódását. Az üledékes kőzetekben gyakori járulékos ásvány, a pirit a legreaktívabb a vizsgált ásványok közül. A pirit nagynyomású hidrogén jelenlétében reduktívan oldódhat, amelynek eredményeként a pirit felületén pirrhotin válik ki, valamint kénhidrogén képződik. Geokémiai modellezési eredményeim és az XPS vizsgálatra alapozott számításaim azonos eredményre vezettek a kivált pirrhotin mennyiségét illetően, azaz 95 m/m.% kalcit és 5 m/m.% pirit keverékben a H_2 hatására mintegy 0,02 m/m.% pirrhotin képződése várható.

Az ásványok reaktivitásának vizsgálati eredménye alapján elmondható, hogy a Pannon-medence fő tárolókőzetének ásványai nem lépnek reakcióba, vagy reakcióba lépésük a hidrogénnel csak kismértékű változást okoz a rezervoár ásványos összetételében. Ezek bíztató eredmények a térségre nézve a geológiai formációk hasznosításának tekintetében. Az Erdélyi-medence sókőzeteinek mikroszerkezet vizsgálatát a sókavernák kialakításához szükséges kritériumokkal összevetve elmondható, hogy a deformációs ráta elfogadható lehet a rövid távú (néhány száz év) hasznosításához, azonban pontosabb következtetésekhez további vizsgálatok javasoltak a jelentősen deformált kőzettesten.

9. References

Adamuszek, M., Tămaş, D.M., Barabasch, J. and Urai, J.L. 2021. Rheological stratification in impure rock salt during long-term creep: Morphology, microstructure, and numerical models of multilayer folds in the Ocnele Mari salt mine, Romania. *Solid Earth*, **12**, 2041–2065, https://doi.org/10.5194/se-12-2041-2021.

Allen, R.D., Doherty, T.J. and Thoms, R.L. 1982. *Geotechnical factors and guidlines for storage of compressed air in solution-mined salt cavities*, United States, https://doi.org/10.2172/5234728.

Alonso-Vante, N., Chatzitheodorou, G., Fiechter, S., Mgoduka, N., Poulios, I. and Tributsch, H. 1988. Interfacial behavior of hydrogen-treated sulphur deficient pyrite (FeS2-x). *Solar Energy Materials*, **18**, 9–21, https://doi.org/10.1016/0165-1633(88)90041-X.

Amid, A., Mignard, D. and Wilkinson, M. 2016. Seasonal storage of hydrogen in a depleted natural gas reservoir. *International Journal of Hydrogen Energy*, **41**, 5549–5558, https://doi.org/10.1016/j.ijhydene.2016.02.036.

Armstrong, J. T. 1991. Quantitative elemental analysis of individual microparticles with electron beam instruments. In: Electron Probe Quantitation. Springer US, Boston, MA, 261–315. http://dx.doi.org/10.1007/978-1-4899-2617-3_15.

Arvidson, R.S., Ertan, I.E., Amonette, J.E. and Luttge, A. 2003. Variation in calcite dissolution rates: A fundamental problem? *Geochimica et Cosmochimica Acta*, **67**, 1623–1634, https://doi.org/10.1016/S0016-7037(02)01177-8.

Badics, B. and Vető, I. 2012. Source rocks and petroleum systems in the Hungarian part of the Pannonian Basin: The potential for shale gas and shale oil plays. *Marine and Petroleum Geology*, **31**, 53–69, https://doi.org/10.1016/j.marpetgeo.2011.08.015.

Balázs, A., Matenco, L., Vogt, K., Cloetingh, S. and Gerya, T. 2018. Extensional Polarity Change in Continental Rifts: Inferences From 3-D Numerical Modeling and Observations. *Solid Earth*, **123**, 8073–8094, https://doi.org/10.1029/2018JB015643.

Báldi, K., Velledits, F., Corić, S., Lemberkovics, V., Lőrincz, K. and Shevelev, M. 2017. Discovery of the Badenian evaporites inside the Carpathian Arc: Implications for global climate change and Paratethys salinity. *Geologica Carpathica*, **68**, 193–206, https://doi.org/10.1515/geoca-2017-0015.

Bancroft, G.M., Brown, J.R. and Fyfe, W.S. 1979. Advances in, and applications of, X-ray

photoelectron spectroscopy (ESCA) in mineralogy and geochemistry. *Chemical Geology*, **25**, 227-243, https://doi.org/10.1016/0009-2541(79)90144-X.

Baric, G., Ivkovic, Z. and Perica, R. 2000. The Miocene petroleum system of the Sava Depression, Croatia. *Petroleum Geoscience*, **6**, 165–173, https://doi.org/10.1144/petgeo.6.2.165.

Bauer, S. 2017. *Underground Sun Storage. Final Report*. Accessed 19 October 2024, https://www.underground-sun-storage.at/fileadmin/bilder/03_NEU_SUNSTORAGE/Downloads/Underground_Sun.Storage_Publizierbarer_Endbericht_English.pdf.

Baumann, J., Buhmann, D., Dreybrodt, W. and Schulz, H.D. 1985. Calcite dissolution kinetics in porous media. *Chemical Geology*, **53**, 219–228, https://doi.org/10.1016/0009-2541(85)90071-3.

Bernard, S., Wirth, R., Schreiber, A., Schulz, H.-M. and Horsfield, B. 2012. Formation of nanoporous pyrobitumen residues during maturation of the Barnett Shale (Fort Worth Basin). *International Journal of Coal Geology*, **103**, 3–11, https://doi.org/10.1016/j.coal.2012.04.010.

Bo, Z., Zeng, L., Chen, Y. and Xie, Q. 2021. Geochemical reactions-induced hydrogen loss during underground hydrogen storage in sandstone reservoirs. *International Journal of Hydrogen Energy*, **46**, 19998–20009, https://doi.org/10.1016/j.ijhydene.2021.03.116.

Breunese, J.N., Van Eijs, R.M.H.E., De Meer, S. and Kroon, I.C. 2003. Observation and prediction of the relation between salt creep and land subsudence in solution mining. The Barradeel case. Proceedings SMRI Fall Meeting, Cester 2003, 38–57. Accessed 19 October 19, 2024, https://smri.memberclicks.net/assets/docs/Abstracts/2003/Fall/MP2003F_Breunese.pdf.

Brkić, D. 2024. Serbian Energy Sector in a Gap Between East and West. *Energy Exploration & Exploitation*, **42**, 330-340, https://doi.org/0.1177/01445987231215445.

Bukowski, K. 2013. Chapter 2 . Salt sources and salt springs in the Carpathian zone. *In*: *Archaeolingua*. 9. ISBN 978-963-9911-44-4.

Caglayan, D.G., Weber, N., Heinrichs, H.U., Linßen, J., Robinius, M., Kukla, P.A. and Stolten, D. 2020. Technical potential of salt caverns for hydrogen storage in Europe. *International Journal of Hydrogen Energy*, **45**, 6793–6805, https://doi.org/10.1016/j.ijhydene.2019.12.161.

Carden, P.O. and Paterson, L. 1979. Physical, chemical and energy aspects of underground hydrogen storage. *International Journal of Hydrogen Energy*, **4**, 559–569, https://doi.org/10.1016/0360-3199(79)90083-1.

Carothers, W.W. and Kharaka, Y.K. 1978. Aliphatic Acid Anions in Oil-Field Waters - Implications for Origin of Natural Gas. *AAPG Bulletin*, **62**, 2441–2453, https://doi.org/10.1306/c1ea5521-16c9-11d7-8645000102c1865d.

Cavanagh, A., Yousefi, H., Wilkinson, M. and Groenenberg, R. 2023. *Classifying Hydrogen Storage Potential in Porous Reservoirs as an Aid to European Site Selection. H2020 HyUSPRe Project Report*. Accessed 19 October 2024, https://www.hyuspre.eu/wp-content/uploads/2023/04/HyUSPRe_D1.5_Classifying-hydrogen-storage-potential_incl.-Supplement_2023.03.31.pdf.

Chang, L.L.Y., Howie, R.A. and Zussman, J. 1996. *Rock-Forming Minerals, Volume 5B: Non-Silicates, Sulphates, Carbonates, Phosphates and Halides*, 5th ed. https://doi.org/10.1180/minmag.1996.060.400.20.

Chanthakett, A., Arif, M.T., Khan, M.M.K. and Subhani, M. 2023. *Hydrogen Production from Municipal Solid Waste Using Gasification Method*, https://doi.org/10.1016/B978-0-443-15329-7.00012-0.

Chen, D., Rojas, M., Samset, B.H., Cobb, K. Diongue Niang A., Edwards, P., Emori, S., Faria, S.H., Hawkins, E., Hope, P., Huybrechts, P., Meinhausen, M., Mustafa, S.K., Plattner, G.-K. and Tréguier, A.-M. 2021. Framing, Context, and Methods. *In*: Masson-Delmotte, V., Zhai, P., Pirani, A., Connors, S.L., Péan, C., Berger, S., Caud, N., Chen, Y., Goldfarb, L., Gomis, M.I., Huang, M., Leitzell, K., Lonnoy, E., Matthews, J.B.R., Maycock, T.K., Waterfield, T., Yelekçi, O., Yu, R. and Zhou, B. (eds) *Climate Change 2021: The Physical Science Basis. Contribution of Working Group I to the Sixth Assessment Report of the Intergovernmental Panel on Climate Change*. 147–286, https://doi.org/10.1017/9781009157896.003.

Chou, L. and Wollast, R. 1984. Study of the weathering of albite at room temperature and pressure with a fluidized bed reactor. *Geochimica et Cosmochimica Acta*, **48**, 2205–2217, https://doi.org/10.1016/0016-7037(84)90217-5.

Cihlar, J., Mavins, D. and Van der Leun, K. 2021. *Picturing the Value of Underground Gas Storage to the European Hydrogen System*. Accessed 19 October 2024,

https://www.gie.eu/wp-content/uploads/filr/3517/Picturing%20the%20value%20of%20gas%20storage%20to%20the%20European%20hydrogen%20system_FINAL_140621.pdf.

Commission, 'Report from the commission to the european parliamant and the council on certain aspects concerning gas storage based on Regulation (EU) 2017/1938 of the European Parliament and of the Council' COM (2023) 182 final.

Correns, C.W. and von Engelhardt, W. 1938. Neue Untersuchungen fiber die Verwitterung. *Naturwissenschaften*, **230**, 137–138, https://doi.org/10.1007/BF01772798.

Crotogino, F., Schneider, G.S. and Evans, D.J. 2018. Renewable energy storage in geological formations. *Proceedings of the Institution of Mechanical Engineers, Part A: Journal of Power and Energy*, **232**, 100–114, https://doi.org/10.1177/0957650917731181.

Cyran, K. 2020. Insight into a shape of salt storage caverns. *Archives of Mining Sciences*, **65**, 363–398, https://doi.org/10.24425/ams.2020.133198.

De Las Cuevas, C. 1997. Pore structure characterization in rock salt. *Engineering Geology*, **47**, 17–30, https://doi.org/10.1016/s0013-7952(96)00116-0.

Dopffel, N., Jansen, S. and Gerritse, J. 2021. Microbial side effects of underground hydrogen storage – Knowledge gaps, risks and opportunities for successful implementation. *International Journal of Hydrogen Energy*, **46**, 8594–8606, https://doi.org/10.1016/j.ijhydene.2020.12.058.

Draskóczy, I. 2014. A kősó bányászat átalakulása Erdélyben az Árpád-korban. *In*: Bárány, A., Dreska, G. and Szovák, K. (eds) *Arcana Tabularii: Tanulmányok Solymosi László Tiszteletére I-II*. 825–835. ISBN 978-963-473-760-5ö

Ebrahimiyekta, A. 2017. Characterization of geochemical interactions and migration of hydrogen in sandstone sedimentary formations : Application to geological storage. *Thesis*, 190. Available 19 October 2024, https://theses.hal.science/tel-01713106v1.

Emmel, B., Bjørkvik, B., Frøyen, T.L., Cerasi, P. and Stroisz, A. 2023. Evaluating the hydrogen storage potential of shut down oil and gas fields along the Norwegian continental shelf. *International Journal of Hydrogen Energy*, **48**, 24385–24400, https://doi.org/10.1016/j.ijhydene.2023.03.138.

Farkas, B., Köller, L. and Kövesdi, I. 2024. Issues for the Introduction of Hydrogen-Powered Rail Vehicles on Hungarian Reional Railway Lines Through an Example from Germany. *Transportation Research Procedia*, **77**, 35–42, https://doi.org/10.1016/j.trpro.2024.01.005.

Flesch, S., Pudlo, D., Albrecht, D., Jacob, A. and Enzmann, F. 2018. Hydrogen underground storage—Petrographic and petrophysical variations in reservoir sandstones from laboratory experiments under simulated reservoir conditions. *International Journal of Hydrogen Energy*, **43**, 20822–20835, https://doi.org/10.1016/j.ijhydene.2018.09.112.

Foh, S., Novil, M., Rockar, E. and Randolph, P. 1979. *Underground Hydrogen Storage. Final Report [Salt Caverns, Excavated Caverns, Aquifers and Depleted Fields]*, https://doi.org/10.2172/6536941.

Fuchs, R. and Hamilton, W. 2006. New Depositional Architecture for an Old Giant: The Matzen Field, Austria. *In*: Golonka, J. and Picha, F. J. (eds) *The Carpathians and Their Foreland: Geology and Hydrocarbon Resources: AAPG Memoir*. 205–219., https://doi.org/10.1306/985609m843069.

Gelencsér, O., Árvai, C., Mika, L. T., Breitner, D., LeClair, D., Szabó, C., Falus, G. and Szabó-Krausz, Zs. 2023. Effect of hydrogen on calcite reactivity in sandstone reservoirs: Experimental results compared to geochemical modeling predictions. *Journal of Energy Storage*, **61**, 106737, https://doi.org/10.1016/j.est.2023.106737.

Gelencsér, O., Tóth, P., Németh, T., Szabó-Krausz, Z. and Falus, G. 2024a. A felszín alatti hidrogéntárolás kőzetalkotó ásványokra gyakorolt hatása a Pannon-medencében. *Scientia et Securitas*, **4**, 1–9, https://doi.org/10.1556/112.2023.00182.

Gelencsér, O., Szakács, A., Gál, Á., Szabó, Á., Dankházi, Z., Tóth, T. Breitner, D., Szabó-Krausz, Z., Szabó, C. and Falus, G. 2024b. Microstructural study of the Praid Salt Diapir (Transylvanian basin, Romania) and its implication on deformation history and hydrogen storage potential. *Acta Geodaetica et Geophysica*, **59**, 343–365 https://doi.org/10.1007/s40328-024-00436-z.

Gelencsér, O., Szabó-Krausz, Z., Németh, T., Árvai, Cs., Mika, L.T., Kővágó, Á. Breitner, D. Tóth, P. and Falus, G. 2024c. K-feldspar – H_2 interaction in the context of underground hydrogen storage. *Földtani Közlöny*, **154**, 267–276, https://doi.org/10.23928/foldt.kozl.2024.154.3.267.

Gelencsér, O., Sulyok, A., Árvai, Cs., Mika, L.T., Breitner, D., Szabó, Cs., Szabó-Krausz, Z. and Falus, G. under rev.1. Pyrite reactivity under subsurface hydrogen storage conditions – experimental and modeling study. *Journal of Energy Storage*.

Gelencsér, O., Cseresznyés, D., Szamosfalvi, Á., Breitner, D., Kővágó, Á., Szabó, C. and Falus, G. under rev.2. Geological potential of hydrogen storage in the Pannonian Basin complex. under rev.2. *Geological Society Special Publication*.

Ghanbarzadeh, S., Hesse, M.A., Prodanović, M. and Gardner, J.E. 2015. Deformation-assisted fluid percolation in rock salt. *Science*, **350**, 1069–1072, https://doi.org/10.1126/science.aac8747.

Ghergari, L., Mészáros, N., Hosu, A., Filipescu, S. and Chira, C. 1991. The gypsiferous formation at Cheia (Cluj County). *Studia Univ. Babes-Bolyai, Geologia*, **36**, 13–28.

Gillhaus, A. and Horváth, P.L. 2008. Compilation of geological and geotechnical data of worldwide domal salt deposits and domal salt cavern fields. SMRI research report 2007-SMRI, 2008. Accessed 19 October 2024, https://smri.memberclicks.net/assets/docs/Historical_Conferences_Summaries/2000s/SummaryRR2007_01_SMRI_Gillhaus_p1of5.pdf.

Gunter, W.D., Bachu, S. and Benson, S. 2004. The role of hydrogeological and geochemical trapping in sedimentary basins for secure geological storage of carbon dioxide. *Geological Society Special Publication*, **233**, 129–145, https://doi.org/10.1144/GSL.SP.2004.233.01.09.

Guo, L., Su, J., Wang, Z., Shi, J., Guan, X., Cao, W. and Ou, Z. 2023. Hydrogen safety: An obstacle that must be overcome on the road towards future hydrogen economy. *International Journal of Hydrogen Energy*, https://doi.org/10.1016/j.ijhydene.2023.08.248.

Hall, A.J. 1986. Pyrite-pyrrhotine redox reactions in nature. *Mineralogical Magazine*, **50**, 223–229, https://doi.org/10.1180/minmag.1986.050.356.05.

Harris, N.B. 1992. Burial diagenesis of Brent sandstones : A study of Statfjord , Hutton and Lyell fields. *Geological Society Special Publication*, **61**, 351–375, https://doi.org/10.1144/GSL.SP.1992.061.01.18.

Hashemi, L., Blunt, M. and Hajibeygi, H. 2021. Pore-scale modelling and sensitivity analyses of hydrogen-brine multiphase flow in geological porous media. *Scientific Reports*, **11**, 1–13, https://doi.org/10.1038/s41598-021-87490-7.

Hassannayebi, N., Azizmohammadi, S., De Lucia, M. and Ott, H. 2019. Underground hydrogen storage: application of geochemical modelling in a case study in the Molasse Basin, Upper Austria. *Environmental Earth Sciences*, **78**, 1–14, https://doi.org/10.1007/s12665-019-8184-5.

Hassanpouryouzband, A., Joonaki, E., Edlmann, K. and Haszeldine, R.S. 2021. Offshore Geological Storage of Hydrogen: Is This Our Best Option to Achieve Net-Zero? *ACS Energy Letters*, **6**, 2181–2186, https://doi.org/10.1021/acsenergylett.1c00845.

Heinemann, N., Booth, M.G., Haszeldine, R.S., Wilkinson, M., Scafidi, J. and Edlmann, K. 2018. Hydrogen storage in porous geological formations – onshore play opportunities in the midland valley (Scotland, UK). *International Journal of Hydrogen Energy*, **43**, 20861–20874, https://doi.org/10.1016/j.ijhydene.2018.09.149.

Heinemann, N., Alcalde, J., Miocic, J.M., Hangx, S.J.T., Kallmeyer, J., Ostertag-Henning, C., Hassanpouryouzband, A., Thaysen, E.M., Strobel, G.J., Schmidt-Hattenberger, C., Edlmann, K., Wilkinson, M., Bentham, M., Haszeldine, R.S., Carbonell, R. and Rudolff, A. 2021. Enabling large-scale hydrogen storage in porous media-the scientific challenges. *Energy and Environmental Science*, **14**, 853–864, https://doi.org/10.1039/d0ee03536j.

Heinrich, E.W., Salotti, C.A. and Giardini, A.A. 1978. Hydrogen-mineral reactions and their application to the removal of iron from spodumene. *Energy*, **3**, 273–279, https://doi.org/10.1016/0360-5442(78)90023-3.

Hematpur, H., Abdollahi, R., Rostami, S., Haghighi, M. and Blunt, M.J. 2023. Review of underground hydrogen storage: Concepts and challenges. *Geo-Energy Research*, **7**, 111–131, https://doi.org/10.46690/ager.2023.02.05.

Hemme, C. and van Berk, W. 2017. Potential risk of H_2S generation and release in salt cavern gas storage. *Journal of Natural Gas Science and Engineering*, **47**, 114–123, https://doi.org/10.1016/j.jngse.2017.09.007.

Henkel, S., Pudlo, D., Werner, L., Enzmann, F., Reitenbach, V., Albrecht, D., Würdemann, H., Heister, K., Ganzer, L. and Gaupp, R. 2014. Mineral reactions in the geological underground induced by H_2 and CO_2 injections. *Energy Procedia*, **63**, 8026–8035, https://doi.org/10.1016/j.egypro.2014.11.839.

Hibbard, L. and Gilfillan, S.M. V. 2024. Constraining the hydrogen storage capacity of natural gas storage sites in the United States. *International Journal of Hydrogen Energy*, **68**, 74–84, https://doi.org/10.1016/j.ijhydene.2024.03.342.

Horváth, F. and Royden, L. 1981. Mechanism for the formation of the Intra-Carpathian basins: a review. *Earth Evol. Sciences*, **1**, 307–316.

Horváth, F. and Cloetingh, S. 1996. Stress-induced late-stage subsidence anomalies in the

Pannonian basin. *Tectonophysics*, **266**, 287–300, https://doi.org/10.1016/S0040-1951(96)00194-1.

Horváth, F., Bada G., Windhoffer, G., Csontos, L., Dombrádi, E., Dövényi, P., Fodor, L., Grenerczy, G., Síkhegyi, F., Szafián, P., Székely, B., Tímár, G., Tóth, L. and Tóth, T. 2006a. Atlas of the present-day geodynamics of the Pannonian basin. Euroconform maps with explanatory text. *Hungarian Geophysics*, **47**, 133–137, Accessed 19 October 2024, http://geophysics.elte.hu/atlas/geodin_atlas.htm.

Horváth, F., Bada, G., Szafián, P., Tari, G., Ádám, A. and Cloetingh, S. 2006b. Formation and deformation of the Pannonian Basin: constraints from observational data. — IN: Gee, D. G. and Stephenson, R. A. (eds): European Lithosphere Dynamics. Geological Society, London. Memoirs 32, 191–206. ISBN 978-1-86239-212-0.

Hou, L., Yu, Z., Luo, X. and Wu, S. 2022. Self-sealing of caprocks during CO_2 geological sequestration. *Energy*, **252**, 124064, https://doi.org/10.1016/j.energy.2022.124064.

IEA. 2019. *The Future of Hydrogen. Seizing Today's Opportunities*. ISBN 978-8-49668-020-3

Iordache, I., Schitea, D., Gheorghe, A. V. and Iordache, M. 2014. Hydrogen underground storage in Romania, potential directions of development, stakeholders and general aspects. *International Journal of Hydrogen Energy*, **39**, 11071–11081, https://doi.org/10.1016/j.ijhydene.2014.05.067.

Jackson, M.P.A. and Hudec, M.R. 2017. *Salt Tectonics: Principles and Practice*. https://doi.org/10.1017/9781139003988.

Jalalh, A.A. 2006. Compressibility of porous rocks: Part I. Measurements of Hungarian reservoir rock samples. *Acta Geophysica*, **54**, 319–332, https://doi.org/10.2478/s11600-006-0025-8.

Jorovic, N. V. 2009. Reservoir characterization of the underground gas storage " Banatski Dvor". *In*: *In EGU General Assembly Conference Abstracts*, 16. https://meetingorganizer.copernicus.org/EGU2009/EGU2009-16.pdf.

Juhász, G. 1994. Comparison of the sedimentary sequences in Late Neogene subbasins in the Pannonian Basin, Hungary (*in Hungarian*). *Bulletin of the Hungarian Geological Society*, **124**, 341–365, Accessed 20 October 2024, https://real-j.mtak.hu/8936/4/Foldtani_Kozlony_1994_124_4.pdf.

Kanaani, M., Sedaee, B. and Asadian-Pakfar, M. 2022. Role of Cushion Gas on Underground Hydrogen Storage in Depleted Oil Reservoirs. *Journal of Energy Storage*, **45**, 103783,

https://doi.org/10.1016/j.est.2021.103783.

Kantorowicz, J.D., Bryant, I.D. and Dawns, J.M. 1987. Controls on the geometry and distribution of carbonate cements in Jurassic sandstones: Bridport Sands, southern England and Viking Group, Toll Field, Norway. *Geological Society Special Publication*, **36**, 103–118, https://doi.org/10.1144/gsl.sp.1987.036.01.09.

Kázmér, M. 1990. Birth, life and death of the Pannonian Lake. *Palaeogeography, Palaeoclimatology, Palaeoecology*, **79**, 171–188, https://doi.org/10.1016/0031-0182(90)90111-J.

Kuhlemann, J., Frisch, W., Dunkl, I. and Székely, B., 2001. Quantifying tectonic versus erosive denudation by the sediment budget: The Miocene core complexes of the Alps. *Tectonophysics*, **330**, 1–23, https://doi.org/10.1016/S0040-1951(00)00209-2.

Király, A., Milota, K., Magyar, I. and Kiss, K. 2010. Tight gas exploration in the Pannonian Basin. *Petroleum Geology Conference Proceedings*, **7**, 1125–1129, https://doi.org/10.1144/0071125.

Kiss, J., Vértesy, L., Takács, E. and Gulyás, Á. 2019. Geophysical research of Nyírség area (*in Hungarian)*. *Hungarian Geophysics*, **60**, 103–130, Accessed 20 October 2024, https://real.mtak.hu/105382/1/KissJ_etal_MaGeof_60-3.pdf

Kováč, M., Baráth, I., Harzhauser, M., Hlavatý, I. and Hudáčková, N. 2004. Miocene depositional systems and sequence stratigraphy of the Vienna Basin. *CFS Courier Forschungsinstitut Senckenberg*, **246**, 187–212, Accessed 20 October 2024, https://www.researchgate.net/publication/285878992_Miocene_depositional_systems_and_sequence_stratigraphy_of_the_Vienna_Basin.

Kovács, Z. 2018. Hydrocarbon geological introduction to the description of Hungarian sub-basins. *In*: Kovács, Z. (eds) *Hydrocarbons in Hungary: Results and opportunities*. 31-37, ISBN 978-615-00-2316-8.

Krézsek, C. and Bally, A.W. 2006. The Transylvanian Basin (Romania) and its relation to the Carpathian fold and thrust belt: Insights in gravitational salt tectonics. *Marine and Petroleum Geology*, **23**, 405–442, https://doi.org/10.1016/j.marpetgeo.2006.03.003.

Krézsek, C. and Filipescu, S. 2005. Middle to late Miocene sequence stratigraphy of the Transylvanian Basin (Romania). *Tectonophysics*, **410**, 437–463, https://doi.org/10.1016/j.tecto.2005.02.018.

Krézsek, C., Filipescu, S., Silye, L., Maţenco, L. and Doust, H. 2010. Miocene facies associations and sedimentary evolution of the Southern Transylvanian Basin (Romania): Implications for hydrocarbon exploration. *Marine and Petroleum Geology*, **27**, 191–214, https://doi.org/10.1016/j.marpetgeo.2009.07.009.

Kruck, O., Crotogino, F., Prelicz, R. and Rudolph, T. 2013. *Overview on All Known Underground Storage Technologies for Hydrogen (H2020 Project HyUnder - Grant Agreement N. 303417)*. Accessed 20 October 2024, http://hyunder.eu/wp-content/uploads/2016/01/D3.1_Overview-of-all-known-underground-storage-technologies.pdf.

Kuhlemann, J. and Kempf, O. 2002. Post-Eocene evolution of the North Alpine Foreland Basin and its response to Alpine tectonics. *Sedimentary Geology*, **152**, 45–78, https://doi.org/10.1016/S0037-0738(01)00285-8.

Laczkó-Dobos, E., Gier, S., Sztanó, O., Milovský, R. and Hips, K. 2020. Porosity Development Controlled by Deep-Burial Diagenetic Process in Lacustrine Sandstones Deposited in a Back-Arc Basin (Makó Trough, Pannonian Basin, Hungary). *Geofluids*, **2020**, 9020684, https://doi.org/10.1155/2020/9020684.

Lankof, L. and Tarkowski, R. 2020. Assessment of the potential for underground hydrogen storage in bedded salt formation. *International Journal of Hydrogen Energy*, **45**, 19479–19492, https://doi.org/10.1016/j.ijhydene.2020.05.024.

Lankof, L., Urbańczyk, K. and Tarkowski, R. 2022. Assessment of the potential for underground hydrogen storage in salt domes. *Renewable and Sustainable Energy Reviews*, **160**, https://doi.org/10.1016/j.rser.2022.112309.

Lara, R.H., Monroy, M.G., Mallet, M., Dossot, M., González, M.A. and Cruz, R. 2015. An experimental study of iron sulfides weathering under simulated calcareous soil conditions. *Environmental Earth Sciences*, **73**, 1849–1869, https://doi.org/10.1007/s12665-014-3540-y.

Lasaga, A.C. 1984. Chemical Kinetics of Water-Rock Interactions. *Journal of Geophysical Research*, **89**, 4009–4025, https://doi.org/10.1029/JB089iB06p04009.

Lehner, M., Tichler, R., Steinmüller, H. and Koppe, M. 2014. *Power-to-Gas: Technology and Business Models*, https://doi.org/10.1007/978-3-319-03995-4.

Lenkey, L., Dövényi, P., Horváth, F. and Cloetingh, S.A.P.L. 2001. Geothermics of the Pannonian basin and its bearing on the neotectonics. *Stephan Mueller Special Publication*

Series, **3**, 29–40, https://doi.org/10.5194/smsps-3-29-2002.

Liu, J., Yang, T., Peng, Q., Yang, Y., Li, Y.W. and Wen, X.D. 2021. Theoretical exploration of the interaction between hydrogen and pyrite-type FeS_2 surfaces. *Applied Surface Science*, **537**, 147900, https://doi.org/10.1016/j.apsusc.2020.147900.

Liu, S. and Zhai, Y. 2021. Degree of Al-Si order in K-feldspar and its effect on K-feldspar's dissolution. *Periodico di Mineralogia*, **90**, 359–369, https://doi.org/10.13133/2239-1002/17479.

Liu, S.K., Han, C., Liu, J.M. and Li, H. 2015. Hydrothermal decomposition of potassium feldspar under alkaline condition. *RSC Advances*, **5**, 93301–93309, https://doi.org/10.1039/C5RA17212H.

Lord, A.S., Kobos, P.H. and Borns, D.J. 2014. Geologic storage of hydrogen: Scaling up to meet city transportation demands. *International Journal of Hydrogen Energy*, **39**, 15570–15582, https://doi.org/10.1016/j.ijhydene.2014.07.121.

Lowenstein, T.K. and Spencer, R.J. 1990. Syndepositional origin of potash evaporites: Petrographic and fluid inclusion evidence. *American Journal of Sciencedo*, **290**, 1–42, https://doi.org/10.2475/ajs.290.1.1.

Lux, S., Baldauf-Sommerbauer, G. and Siebenhofer, M. 2018. Hydrogenation of Inorganic Metal Carbonates: A Review on Its Potential for Carbon Dioxide Utilization and Emission Reduction. *ChemSusChem*, **11**, 3357–3375, https://doi.org/10.1002/cssc.201801356.

Ma, X., Xu, Z., Chen, L. and Shi, X. 2021. Creep deformation analysis of gas storage in salt caverns. *International Journal of Rock Mechanics and Mining Sciences*, **139**, 104635, https://doi.org/10.1016/j.ijrmms.2021.104635.

Magyar, I., Radivojević, D., Sztanó, O., Synak, R., Ujszászi, K. and Pócsik, M. 2013. Progradation of the paleo-Danube shelf margin across the Pannonian Basin during the Late Miocene and Early Pliocene. *Global and Planetary Change*, **103**, 168–173, https://doi.org/10.1016/j.gloplacha.2012.06.007.

Małachowska, A., Łukasik, N., Mioduska, J. and Gębicki, J. 2022. Hydrogen Storage in Geological Formations—The Potential of Salt Caverns. *Energies*, **15**, 1–19, https://doi.org/10.3390/en15145038.

Mason, P.R.D., Seghedi, I., Szakács, A. and Downes, H. 1998. Magmatic constraints on geodynamic models of subduction in the East Carpathians, Romania. *Tectonophysics*, **297**,

157–176, https://doi.org/10.1016/S0040-1951(98)00167-X.

Masoudi, M., Hassanpouryouzband, A., Hellevang, H. and Haszeldine, R.S. 2024. Lined rock caverns: A hydrogen storage solution. *Journal of Energy Storage*, **84**, 110927, https://doi.org/10.1016/j.est.2024.110927.

Matos, C.R., Carneiro, J.F. and Silva, P.P. 2019. Overview of Large-Scale Underground Energy Storage Technologies for Integration of Renewable Energies and Criteria for Reservoir Identification. *Journal of Energy Storage*, **21**, 241–258, https://doi.org/10.1016/j.est.2018.11.023.

McBride, E.F., Milliken, K.L., Cavazza, W., Cibin, U., Fontana, D., Picard, D.M. and Zuffa, G.G. 1995. Heterogenous Distribution of Calcite Cement at the Outcrop Scale in Tertiary Sandstones, Northern Appennines, Italy.pdf. *AAPG Bulletin*, **79**, 1044–1062, https://doi.org/10.1306/8D2B21C3-171E-11D7-8645000102C1865D.

McCollom, T.M. and Bach, W. 2009. Thermodynamic constraints on hydrogen generation during serpentinization of ultramafic rocks. *Geochimica et Cosmochimica Acta*, **73**, 856–875, https://doi.org/10.1016/j.gca.2008.10.032.

Megyery, M., Miklos, T., Segesdi, J. and Toth, Z. 2000. Monitoring the solids in well streams of underground gas storage facilities. *Proceedings - SPE International Symposium on Formation Damage Control*, 411–417, https://doi.org/10.2118/58753-ms.

Ministry of Innovation and Technology oh Hungary 2021. *Hungary's National Hydrogen Strategy*. Accessed 19 October 2024, https://kormany.hu/dokumentumtar/magyarorszag-nemzeti-hidrogenstrategiaja.

Miocic, J., Heinemann, N., Edlmann, K., Scafidi, J., Molaei, F. and Alcalde, J. 2023. Underground hydrogen storage: a review. *Geological Society Special Publication*, **528**, 73–86, https://doi.org/10.1144/SP528-2022-88.

Miocic, J.M., Alcalde, J., Heinemann, N., Marzan, I. and Hangx, S. 2022. Toward Energy-Independence and Net-Zero: The Inevitability of Subsurface Storage in Europe. *ACS Energy Letters*, **7**, 2486–2489, https://doi.org/10.1021/acsenergylett.2c01303.

Mullen, J. 2010. Petrophysical characterization of the Eagle Ford shale in South Texas. *Society of Petroleum Engineers - Canadian Unconventional Resources and International Petroleum Conference 2010*, **4**, 2762–2780, https://doi.org/10.2118/138145-ms.

Neculita, C.-M., Zagury, G.J. and Bussiére, B. 2007. Passive Treatment of Acid Mine Drainage

in Bioreactors using Sulfate-Reducing Bacteria: Critical Review and Research Needs. *Journal of Environmental Quality*, **36**, 1–16, https://doi.org/10.2134/jeq2006.0066.

Nesbitt, H.W. Bancroft, G.M., Pratt, A.R. and Scaini, M.J. 1998. Sulfur and iron surface states on fractured pyrite surfaces. *American Mineralogist*, **83**, 1067–1076, https://doi.org/10.2138/am-1998-9-1015.

Oelkers, E.H. and Schott, J. 1995. Experimental study of anorthite dissolution and the relative mechanism of feldspar hydrolysis. *Geochimica et Cosmochimica Acta*, **59**, 5039–5053, https://doi.org/10.1016/0016-7037(95)00326-6.

Oelkers, E.H., Schott, J., Gauthier, J.M. and Herrero-Roncal, T. 2008. An experimental study of the dissolution mechanism and rates of muscovite. *Geochimica et Cosmochimica Acta*, **72**, 4948–4961, https://doi.org/10.1016/j.gca.2008.01.040.

Ozarslan, A. 2012. Large-scale hydrogen energy storage in salt caverns. *International Journal of Hydrogen Energy*, **37**, 14265–14277, https://doi.org/10.1016/j.ijhydene.2012.07.111.

Palandri, J.L. and Kharaka, Y.K. 2004. A compilation of rate parameters of water-mineral interaction kinetics for application to geochemical modeling. *USGS Open File Report*, **2004**–**1068**, 71, https://doi.org/10.3133/ofr20041068.

Panfilov, M. 2010. Underground Storage of Hydrogen : In Situ Self-Organisation and Methane Generation. *Transport in Porous Media*, **85**, 841–865, https://doi.org/10.1007/s11242-010-9595-7.

Parkhurst, D.L. and Appelo, C.A.J. 2013. *Description of Input and Examples for PHREEQC Version 3: A Computer Program for Speciation, Batch-Reaction, One-Dimensional Transport, and Inverse Geochemical Calculations*, https://doi.org/10.3133/tm6A43.

Peach, C.J. and Spiers, C.J. 1996. Influence of crystal plastic deformation on dilatancy and permeability development in synthetic salt rock. *Tectonophysics*, **256**, 101–128, https://doi.org/10.1016/0040-1951(95)00170-0.

Perera, M.S.A. 2023. A review of underground hydrogen storage in depleted gas reservoirs: Insights into various rock-fluid interaction mechanisms and their impact on the process integrity. *Fuel*, **334**, 126677, https://doi.org/10.1016/j.fuel.2022.126677.

Peryt, T.M. 2006. The beginning, development and termination of the Middle Miocene Badenian salinity crisis in Central Paratethys. *Sedimentary Geology*, **188**–**189**, 379–396, https://doi.org/10.1016/j.sedgeo.2006.03.014.

Petrik, A., Fodor, L., Bereczki, L., Klembala, Z., Lukács, R., Baranyi, V., Beke, B. and Harangi, S. 2019. Variation in style of magmatism and emplacement mechanism induced by changes in basin environments and stress fields (Pannonian Basin, Central Europe). *Basin Research*, **31**, 380–404, https://doi.org/10.1111/bre.12326.

Pfeiffer, W.T. and Bauer, S. 2015. Subsurface Porous Media Hydrogen Storage - Scenario Development and Simulation. *Energy Procedia*, **76**, 565–572, https://doi.org/10.1016/j.egypro.2015.07.872.

Plummer, L.N., Wigley, T.M.L. and Parkhurst, D.L. 1978. The kinetics of calcite dissolution in CO_2-water systems at 5 °C to 60 °C and 0. 0 to 1.0 atm CO_2. *American Journal of Science*, **278**, 179–216, https://doi.org/10.2475/ajs.278.2.179.

Porkoláb, K., Broerse, T., Kenyeres, A., Békési, E., Tóth, S., Magyar, B. and Wesztergom, V. 2023. Active tectonics of the Circum-Pannonian region in the light of updated GNSS network data. *Acta Geodaetica et Geophysica*, **58**, 149–173, https://doi.org/10.1007/s40328-023-00409-8.

Royden, L.H. 1988. Late Cenozoic Tectonics of the Pannonian Basin System. In: L.H. Royden and F. Horvath (Eds.): The Pannonian Basin, a study in basin evolution. American Association of Petroleum Geologists Memoir **45**, 27–48, https://doi.org/10.1306/M45474C3.

Rögl, F. 1998. Palaeogeographic Considerations for Mediterranean and Paratethys Seaways (Oligocene to Miocene). *Annalen des Naturhistorischen Museums in Wien*, **99A**, 279–310, https://api.semanticscholar.org/CorpusID:131588774.

Ruszkiczay-Rüdiger, Z., Balázs, A., Csillag, G., Drijkoningen, G. and Fodor, L. 2020. Uplift of the Transdanubian Range, Pannonian Basin: How fast and why? *Global and Planetary Change*, **192**, 103263, https://doi.org/10.1016/j.gloplacha.2020.103263.

Saftić, B., Velić, J., Sztanó, O., Juhász, Gy. and Ivanković, Z. 2003. Tertiary Subsurface Facies, Source Rocks and Hydrocarbon Reservoirs in the SW Part of the Pannonian Basin (North Croatia and Sout-Western Hungary). *Geologica Croatica*, **56**, 101–122, https://doi.org/10.4154/232.

Schreiber, B.C. and El Tabakh, M. 2000. Deposition and early alteration of evaporites. *Sedimentology*, **47**, 215–238, https://doi.org/10.1046/j.1365-3091.2000.00002.x.

Seah, M.P. 1983. Quantification of AES and XPS. *In*: Briggs, D. and Seah, M. (eds) *Practical*

Surface Analysis by Auger and X-Ray Photoelectron Spectroscopy. 181–216, https://doi.org/10.1002/sia.740060611.

Shahriar, M.F., Khanal, A., Khan, M.I. and Pandey, R. 2024. Current status of underground hydrogen storage: Perspective from storage loss, infrastructure, economic aspects, and hydrogen economy targets. *Journal of Energy Storage*, **97**, 112773, https://doi.org/10.1016/j.est.2024.112773.

Shotyk, W. and Nesbitt, H.W. 1992. Incongruent and congruent dissolution of plagioclase feldspar: effect of feldspar composition and ligand complexation. *Geoderma*, **55**, 55–78, https://doi.org/10.1016/0016-7061(92)90005-R.

Simon, J., Ferriz, A.M. and Correas, L.C. 2015. HyUnder - Hydrogen underground storage at large scale: Case study Spain. *Energy Procedia*, **73**, 136–144, https://doi.org/10.1016/j.egypro.2015.07.661.

Spietz, R.L., Payne, D., Kulkarni, G., Metcalf, W.W., Roden, E.E. and Boyd, E.S. 2022. Investigating Abiotic and Biotic Mechanisms of Pyrite Reduction. *Frontiers in Microbiology*, **13**, 1–17, https://doi.org/10.3389/fmicb.2022.878387.

Stillings, L.L. and Brantley, S.L. 1995. Feldspar dissolution at 25°C and pH 3: Reaction stoichiometry and the effect of cations. *Geochimica et Cosmochimica Acta*, **59**, 1483–1496, https://doi.org/10.1016/0016-7037(95)00057-7.

Stillings, L.L., Brantley, S.L. and Machesky, M.L. 1995. Proton adsorption at an adularia feldspar surface. *Geochimica et Cosmochimica Acta*, **59**, 1473–1482, https://doi.org/10.1016/0016-7037(95)00056-6.

Sverjensky, D.A., Hemley, J.J. and D'angelo, W.M. 1991. Thermodynamic assessment of hydrothermal alkali feldspar-mica-aluminosilicate equilibria. *Geochimica et Cosmochimica Acta*, **55**, 989–1004, https://doi.org/10.1016/0016-7037(91)90157-Z.

Szabó, Z., Gál, N.E., Kun, É., Szőcs, T. and Falus, G. 2017. Geochemical modeling possibilities of CO_2 and brine inflow to freshwater aquifers. *Central European Geology*, **60**, 289–298, https://doi.org/10.1556/24.60.2017.014.

Szabó, Z., Gál, N.E., Kun, É., Szőcs, T. and Falus, G. 2018. Accessing effects and signals of leakage from a CO_2 reservoir to a shallow freshwater aquifer by reactive transport modelling. *Environmental Earth Sciences*, **77**, 460, https://doi.org/10.1007/s12665-018-7637-6.

Szakács, A. and Krézsek, C. 2006. Volcano-basement interaction in the Eastern Carpathians: Explaining unusual tectonic features in the Eastern Transylvanian Basin, Romania. *Journal of Volcanology and Geothermal Research*, **158**, 6–20, https://doi.org/10.1016/j.jvolgeores.2006.04.012.

Szilágyi, S.S. and Geiger, J. 2012. Sedimentological study of the Szőreg-1 reservoir (Algyő Field, Hungary): A combination of traditional and 3D sedimentological approaches. *Geologia Croatica*, **65**, 77–90, https://doi.org/10.4154/GC.2012.06.

Sztanó, O., Szafián, P., Magyar, I., Horányi, A., Bada, G., Hughes, D.W., Hoyer, D.L. and Wallis, R.J. 2013. Aggradation and progradation controlled clinothems and deep-water sand delivery model in the Neogene lake pannon, Makó Trough, Pannonian Basin, SE Hungary. *Global and Planetary Change*, **103**, 149–167, https://doi.org/10.1016/j.gloplacha.2012.05.026.

Tari, G., Bada, G., Boote, D.R.D., Krézsek, C., Koroknai, B., Kovács, G., Lemberkovics, V., Sachsenhofer, R.F. and Tóth, T. 2023. The Pannonian Super Basin: A brief overview. *AAPG Bulletin*, **107**, 1391–1417, https://doi.org/10.1306/02172322098.

Tarkowski, R. 2017. Perspectives of using the geological subsurface for hydrogen storage in Poland. *International Journal of Hydrogen Energy*, **42**, 347–355, https://doi.org/10.1016/j.ijhydene.2016.10.136.

Tarkowski, R. 2019. Underground hydrogen storage: Characteristics and prospects. *Renewable and Sustainable Energy Reviews*, **105**, 86–94, https://doi.org/10.1016/j.rser.2019.01.051.

Thiyagarajan, S.R., Emadi, H., Hussain, A., Patange, P. and Watson, M. 2022. A comprehensive review of the mechanisms and efficiency of underground hydrogen storage. *Journal of Energy Storage*, **51**, 104490, https://doi.org/10.1016/j.est.2022.104490.

Tiliță, M., Scheck-Wenderoth, M., Maţenco, L. and Cloetingh, S. 2015. Modelling the coupling between salt kinematics and subsidence evolution: Inferences for the Miocene evolution of the Transylvanian Basin. *Tectonophysics*, **658**, 169–185, https://doi.org/10.1016/j.tecto.2015.07.021.

Tiliță, M., Lenkey, L., Maţenco, L., Horváth, F., Surányi, G. and Cloetingh, S. 2018. Heat flow modelling in the Transylvanian basin: Implications for the evolution of the intra-Carpathians area. *Global and Planetary Change*, **171**, 148–166, https://doi.org/10.1016/j.gloplacha.2018.07.007.

Truche, L., Berger, G., Destrigneville, C., Pages, A., Guillaume, D., Giffaut, E. and Jacquot, E. 2009. Experimental reduction of aqueous sulphate by hydrogen under hydrothermal conditions: Implication for the nuclear waste storage. *Geochimica et Cosmochimica Acta*, **73**, 4824–4835, https://doi.org/10.1016/j.gca.2009.05.043.

Truche, L., Berger, G., Destrigneville, C., Guillaume, D. and Giffaut, E. 2010. Kinetics of pyrite to pyrrhotite reduction by hydrogen in calcite buffered solutions between 90 and 180°C: Implications for nuclear waste disposal. *Geochimica et Cosmochimica Acta*, **74**, 2894–2914, https://doi.org/10.1016/j.gca.2010.02.027.

Truche, L., Jodin-Caumon, M.C., Lerouge, C., Berger, G., Mosser-Ruck, R., Giffaut, E. and Michau, N. 2013. Sulphide mineral reactions in clay-rich rock induced by high hydrogen pressure. Application to disturbed or natural settings up to 250°C and 30bar. *Chemical Geology*, **351**, 217–228, https://doi.org/10.1016/j.chemgeo.2013.05.025.

Tutolo, B.M., Luhmann, A.J., Kong, X.Z., Saar, M.O. and Seyfried, W.E. 2015. CO2 sequestration in feldspar-rich sandstone: Coupled evolution of fluid chemistry, mineral reaction rates, and hydrogeochemical properties. *Geochimica et Cosmochimica Acta*, **160**, 132–154, https://doi.org/10.1016/j.gca.2015.04.002.

Ustaszewski, K., Herak, M., Tomljenović, B., Herak, D. and Matej, S. 2014. Neotectonics of the Dinarides-Pannonian Basin transition and possible earthquake sources in the Banja Luka epicentral area. *Journal of Geodynamics*, **82**, 52–68, https://doi.org/10.1016/j.jog.2014.04.006.

Van Oosterhout, B.G.A., Hangx, S.J.T. and Spiers, C.J. 2022. A threshold stress for pressure solution creep in rock salt: Model predictions vs. observations. *The Mechanical Behavior of Salt X*, 57–67, https://doi.org/10.1201/9781003295808-6.

Vialle, S. and Wolff-Boenisch, D. 2024. Thermodynamic and kinetic considerations of the link between underground hydrogen storage and reductive carbonate dissolution and methane production. Are limestone reservoirs unsuitable for UHS? *Chemical Geology*, **665**, 122304, https://doi.org/10.1016/j.chemgeo.2024.122304.

Welkenhuysen, K., Brüstle, A.-K., Bottig, M., Ramírez, A., Swennen, R. and Piessens, K. 2016. A techno-economic approach for capacity assessment and ranking of potential options for geological storage of CO_2 in Austria. *Geologica Belgica*, **19**, 237–249, https://doi.org/10.20341/gb.2016.012.

Wollast, R. 1967. Kinetics of the alteration of K-feldspar in buffered solutions at low temperature. *Geochimica et Cosmochimica Acta*, **31**, 635–648, https://doi.org/10.1016/0016-7037(67)90040-3.

Wollast, R. and Chou, L. 1992. Surface reactions during the early stages of weathering of albite. *Geochimica et Cosmochimica Acta*, **56**, 3113–3121, https://doi.org/10.1016/0016-7037(92)90292-Q.

Yekta, A.E., Pichavant, M. and Audigane, P. 2018. Evaluation of geochemical reactivity of hydrogen in sandstone: Application to geological storage. *Applied Geochemistry*, **95**, 182–194, https://doi.org/10.1016/j.apgeochem.2018.05.021.

Yousefi, H., Groenenberg, R., Cavanagh, A. and Wilkinson, M. 2022. *Interactive GIS Story Map of Hydrogen Storage Potential in Porous Reservoirs in Europe, H2020 HyUSPRe Project Report*. Accessed 19 October 2024, https://www.hyuspre.eu/wp-content/uploads/2022/10/HyUSPRe_D1.4_GIS-story-map-of-H2-storage-potential-in-porous-reservoirs-in-Europe_2022.09.30.pdf.

Yuan, G., Cao, Y., Schulz, H.M., Hao, F., Gluyas, J., Liu, K., Yang, T., Wang, Y., Xi, K. and Li, F. 2019. A review of feldspar alteration and its geological significance in sedimentary basins: From shallow aquifers to deep hydrocarbon reservoirs. *Earth-Science Reviews*, **191**, 114–140, https://doi.org/10.1016/j.earscirev.2019.02.004.

Zeng, L., Keshavarz, A., Xie, Q. and Iglauer, S. 2022. Hydrogen storage in Majiagou carbonate reservoir in China: Geochemical modelling on carbonate dissolution and hydrogen loss. *International Journal of Hydrogen Energy*, **47**, 24861–24870, https://doi.org/10.1016/j.ijhydene.2022.05.247.

Zgonnik, V. 2020. The occurrence and geoscience of natural hydrogen: A comprehensive review. *Earth-Science Reviews*, **203**, 103140, https://doi.org/10.1016/j.earscirev.2020.103140.

Zhang, J., Li, B., Li, Y., Lu, J., Wang, K. and Zhang, H. 2021. Effect of sulfide on corrosion behavior of stainless steel 316SS and Hastelloy C276 in sub/supercritical water. *International Journal of Hydrogen Energy*, **46**, 22222–22233, https://doi.org/10.1016/j.ijhydene.2021.04.031.

Zhu, C. 2005. In situ feldspar dissolution rates in an aquifer. *Geochimica et Cosmochimica Acta*, **69**, 1435–1453, https://doi.org/10.1016/j.gca.2004.09.005.

Zhu, C. and Lu, P. 2009. Alkali feldspar dissolution and secondary mineral precipitation in batch systems: 3. Saturation states of product minerals and reaction paths. *Geochimica et Cosmochimica Acta*, **73**, 3171–3200, https://doi.org/10.1016/j.gca.2009.03.015.

Zivar, D., Kumar, S. and Foroozesh, J. 2021. Underground hydrogen storage: A comprehensive review. *International Journal of Hydrogen Energy*, **46**, 23436–23462, https://doi.org/10.1016/j.ijhydene.2020.08.138.

10. Appendices

Appendix 10.1. Development of hydrogen experimental laboratory

It was one of the major aims to build an experimental lab dedicated to geochemical research for underground hydrogen storage in the frame of PhD research. One of such laboratory in Hungary is operating at the Department of Chemical and Environmental Process Engineering, Faculty of Chemical Technology and Biotechnology, Budapest University of Technology and Economics (BME), where ongoing experimental work with high pressure and temperature conditions takes place. The experimental work of the PhD started in this lab which evolved to a long-term successful cooperation including the planning of the hydrogen lab at ELTE. First, a pressure vessel was procured from Parr®, with mostly similar parameters to those of instrument at BME (e.g., volume, material, stirring, controller type) except for some specifications related to pressure and temperature range and solution sampling.

The laboratory was emplaced in a Mott fume hood at the Institute of Geography and Earth Sciences at ELTE. Two fixed and staged gas lines were created ensuring the safe use of high-pressure gases (Figure A.10.1.1). A wood board was installed on the back of the fume hood and the gas line infrastructure stabilized on this board with custom-made fixings (Figure A.10.1.2).

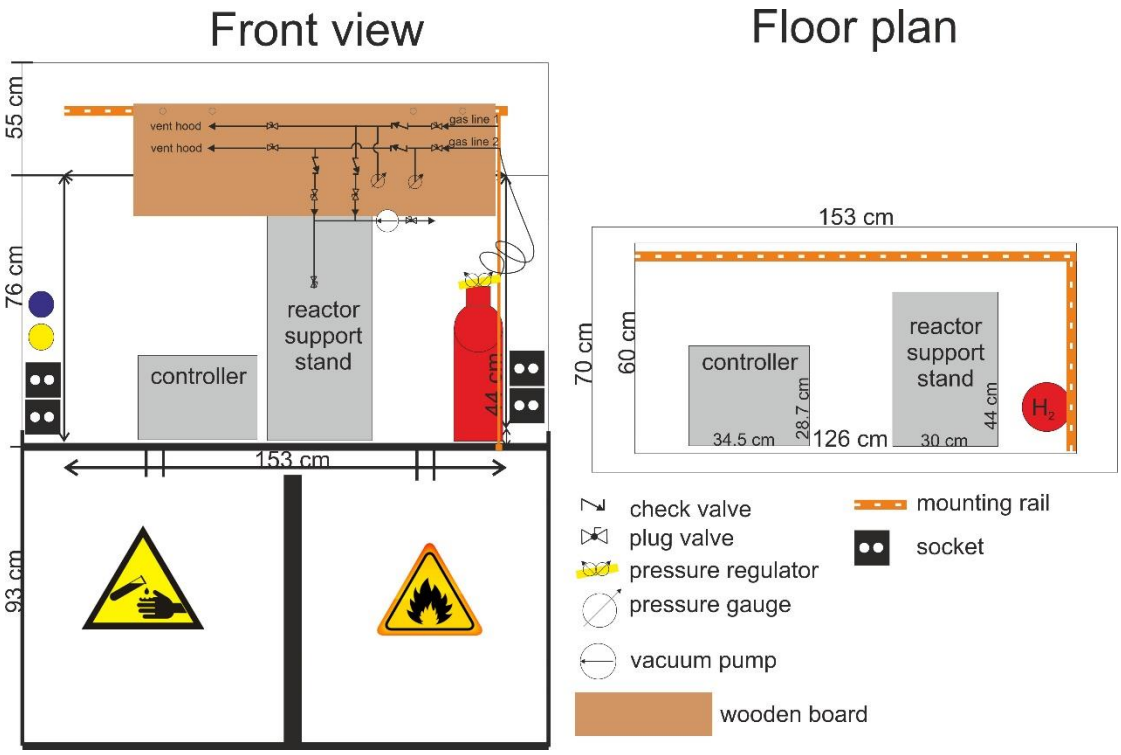

Figure A.10.1.1. *Front view and floor plan of the hydrogen experimental lab.*

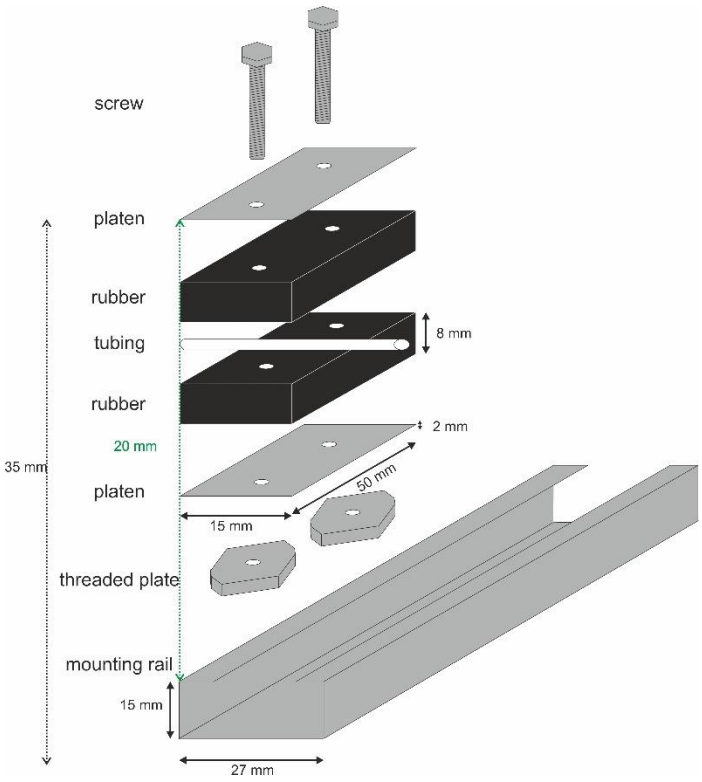

Figure A.10.1.2. *Schematic figure about the custom-made fixing of gas lines (tubes).*

The reactor vessel is connected to the gas line with 1/8 in. tubing made of 304 stainless steel. The parts which are exposed to H_2, such as plug valves, union tees, pressure gauges, connectors, check valves and proportional relief valves are distributed by Swagelok®. Custom made gas bottles were used as gas sources of H_2, N_2 and Ar.

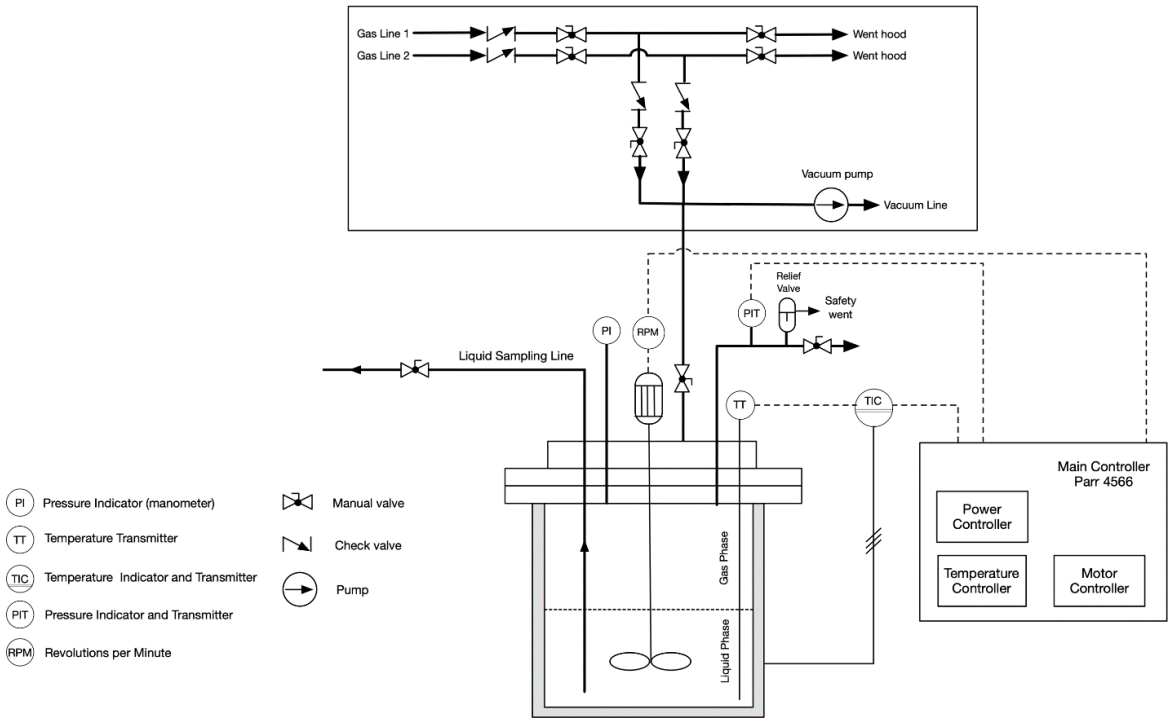

Figure A.10.1.3 *Schematic of the mineral-water-gas experimental setup. Figure courtesy of L.T. Mika.*

Appendix 10.2. Additional information for minerals used in experiment

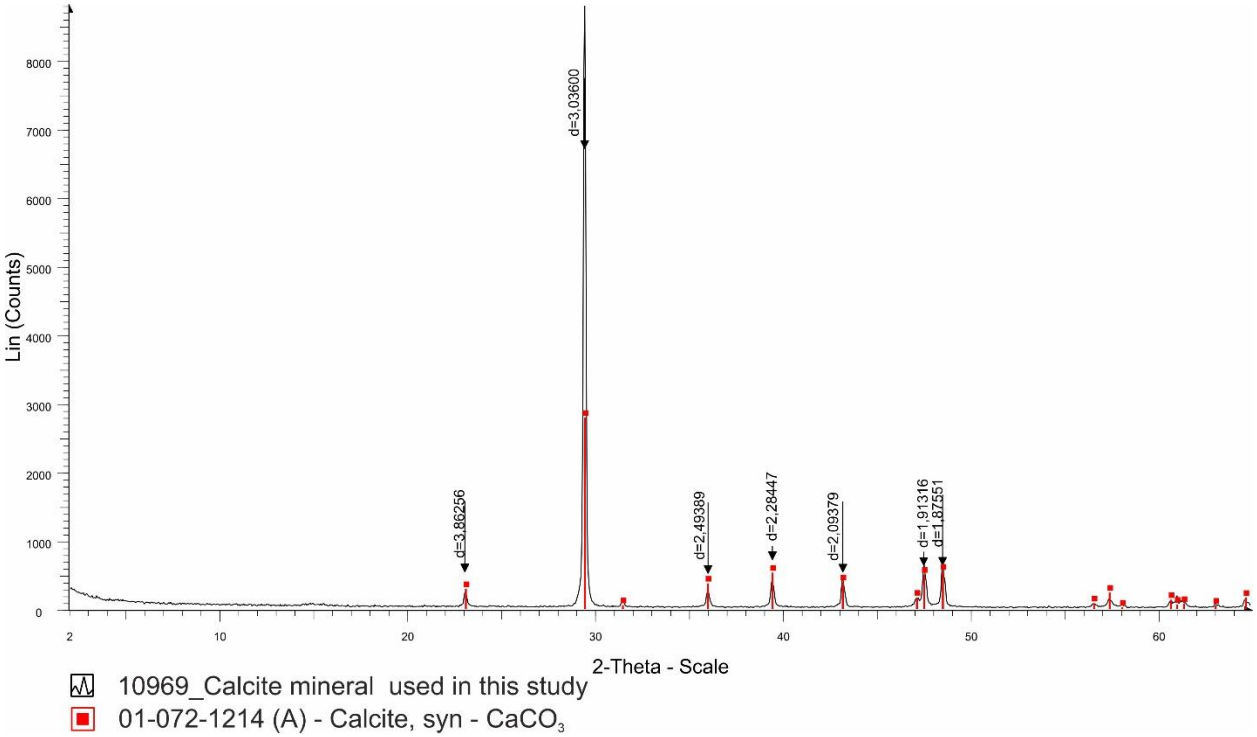

Figure A.10.2.1. *Diffractogram (black) of calcite BE24569 used in calcite experiments made by X-ray powder diffraction (XRD) method and a standard calcite peak position (with red) are also shown for comparison.*

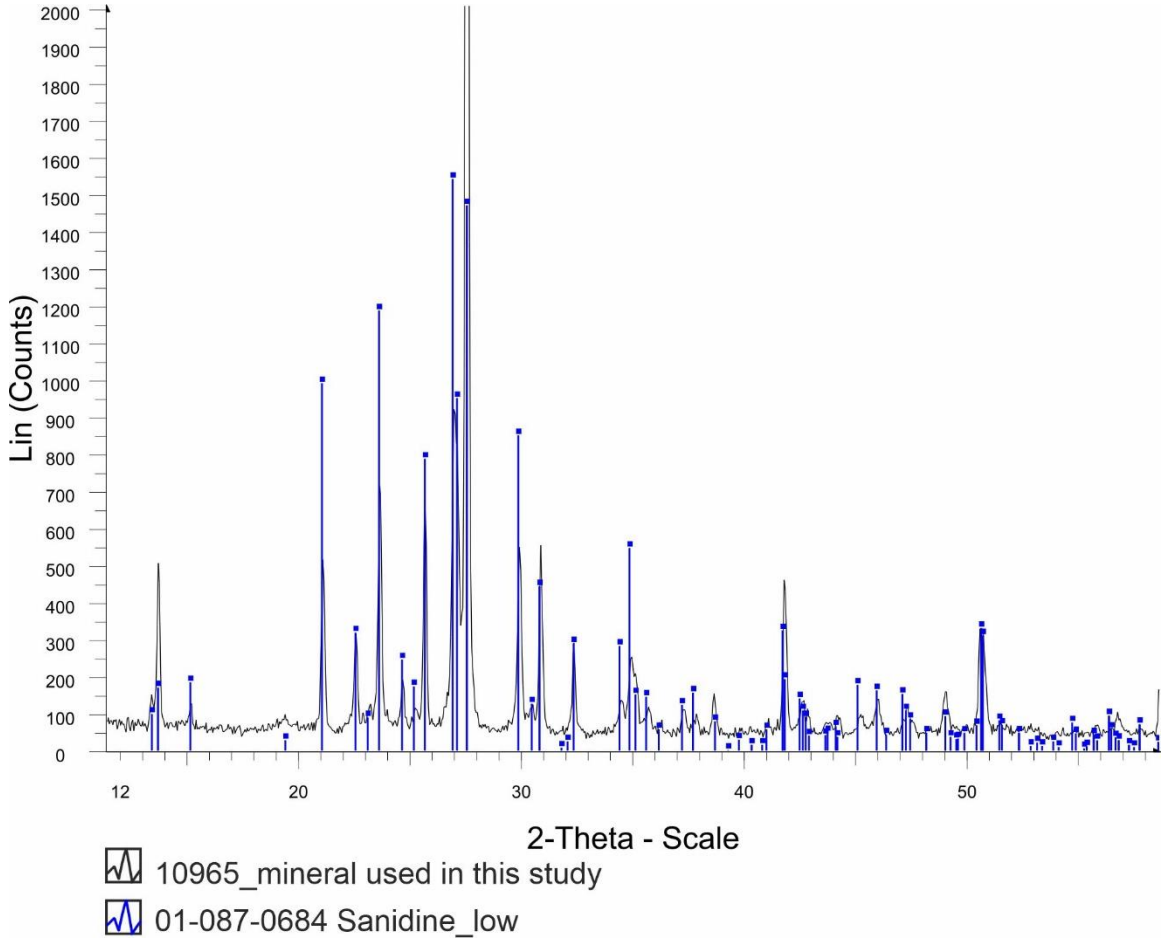

Figure A.10.2.2. *Diffractogram (black) of feldspar BE40767 used in K-feldspar experiments made by X-ray powder diffraction (XRD) method and standard sanidine peak positions (with blue) are also shown for comparison.*

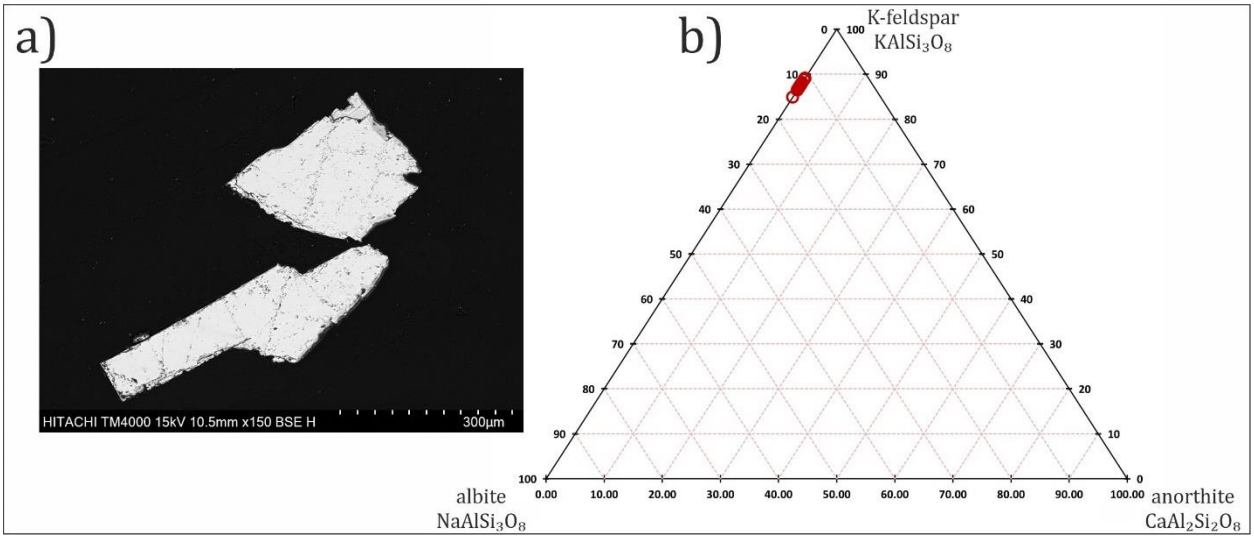

Figure A.10.2.3. *Backscattered electron image and chemical composition of K-feldspar used in experiments. The result of EDS measurements gives a range betweeen Ab_{11}-Ab_{18} content with an average of Ab_{13}.*

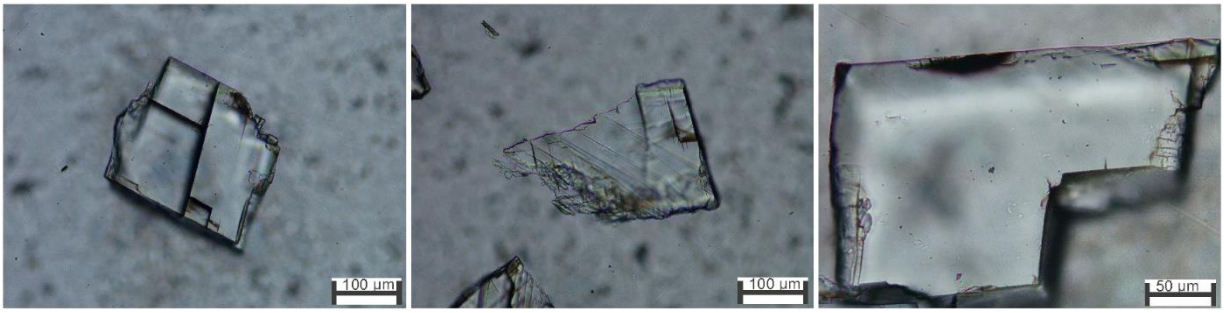

Figure A.10.2.4. *Photomicrographs of calcite grains (BE24569) in thin section under transmitted light. This calcite was used for calcite-H_2 experiments.*

Appendix 10.3. The estimation of pyrrhotite thickness formed on pyrite surface after experimental treatment

The calculation of pyrrhotite thickness on pyrite surface modeled as an ideal sphere, the following steps were performed. The studied grain is assumed to have sphere shape (with a radius of 30 µm) and consists of pyrite and homogeneous pyrrhotite layer on the top (0.2 µm thick layer was calculated by XPS). The volume of the pyrrhotite layer was found by subtracting the original sphere volume from the total volume of the sphere with the pyrrhotite layer. The mass of pyrite and pyrrhotite layer were calculated using the known density of the minerals (4840 kg/m^3 and

4600 kg/m^3 for pyrite and pyrrhotite, respectively). The weight percent (wt.%) of pyrrhotite was determined by dividing the mass of pyrrhotite by the total mass (pyrite and pyrrhotite) of the sphere and then multiplying by 100.

Table A.10.3.1. Fe, Mg and Sr concentrations (mg/L) in solution samples measured by ICP-OES in calcite experiments, (bdl: below detection limit).

	Time (h)	P1H2	*P1H2 (±)*	P5H2_1	*P5H2_1 (±)*	P5H2_2	*P5H2_2 (±)*	P10H2	*P10H2 (±)*	P10N2	*P10N2 (±)*	P10Ar	*P10Ar (±)*
gas type		H_2		H_2		H_2		H_2		N_2		Ar	
py (wt.%)		1		5		5		10		10		10	
Fe	3	bdl		bdl		bdl		bdl		bdl		bdl	
	24.7	bdl		0.03	*0.02*	bdl		0.05	*0.03*	bdl		0.12	*0.03*
	75	bdl		0.17	*0.02*	bdl		0.23	*0.02*	0.04	*0.04*	0.37	*0.04*
Mg	3	0.02	*0.01*	0.07	*0.03*	0.04	*0.02*	0.08	*0.04*	0.09	*0.04*	0.29	*0.03*
	24.7	0.09	*0.05*	0.13	*0.06*	0.06	*0.03*	0.12	*0.06*	0.10	*0.05*	0.32	*0.03*
	75	0.07	*0.04*	0.14	*0.03*	1.29	*0.13*	0.19	*0.04*	0.14	*0.03*	0.43	*0.04*
Sr	3	0.004	*0.002*	0.005	*0.003*	0.003	*0.001*	0.005	*0.003*	0.006	*0.003*	0.006	*0.003*
	24.7	0.006	*0.003*	0.007	*0.003*	0.004	*0.002*	0.007	*0.003*	0.008	*0.004*	0.008	*0.004*
	75	0.006	*0.003*	0.010	*0.005*	0.011	*0.005*	0.009	*0.005*	0.011	*0.005*	0.013	*0.006*

Table A.10.3.2. The Fe, Mg and Sr concentrations (mg/L) in solution samples measured by ICP-OES, (bdl: below detection limit) in calcite–pyrite experiments.

	Time (h)	P1H2	*P1H2 (±)*	P5H2_1	*P5H2_1 (±)*	P5H2_2	*P5H2_2 (±)*	P10H2	*P10H2 (±)*	P10N2	*P10N2 (±)*	P10Ar	*P10Ar (±)*
gas type		**H_2**		**H_2**		**H_2**		**H_2**		**N_2**		**Ar**	
py (wt.%)		**1**		**5**		**5**		**10**		**10**		**10**	
Fe	3	bdl		bdl		bdl		bdl		bdl		bdl	
	24.7	bdl		0.03	*0.02*	bdl		0.05	*0.03*	bdl		0.12	*0.03*
	75	bdl		0.17	*0.02*	bdl		0.23	*0.02*	0.04	*0.04*	0.37	*0.04*
Mg	3	0.02	*0.01*	0.07	*0.03*	0.04	*0.02*	0.08	*0.04*	0.09	*0.04*	0.29	*0.03*
	24.7	0.09	*0.05*	0.13	*0.06*	0.06	*0.03*	0.12	*0.06*	0.10	*0.05*	0.32	*0.03*
	75	0.07	*0.04*	0.14	*0.03*	1.29	*0.13*	0.19	*0.04*	0.14	*0.03*	0.43	*0.04*
Sr	3	0.004	*0.002*	0.005	*0.003*	0.003	*0.001*	0.005	*0.003*	0.006	*0.003*	0.006	*0.003*
	24.7	0.006	*0.003*	0.007	*0.003*	0.004	*0.002*	0.007	*0.003*	0.008	*0.004*	0.008	*0.004*
	75	0.006	*0.003*	0.010	*0.005*	0.011	*0.005*	0.009	*0.005*	0.011	*0.005*	0.013	*0.006*

Appendix 10.4. The detection limit for elements in ICP-OES

Table A.10.4.1. List of detection limit, lower limit, measuring range and relative error ranges of elements measured in this study by ICP-OES.

					Relative error		
Element	**unit**	**Detection limit**	**Lower limit**	**Measuring range**	***>20%***	***20%-10%***	***<10%***
Calcium	mg/L	0.01	0.05	0.05-500	*<0.05*	*0.05-0.25*	*>0.25*
Magnesium	mg/L	0.02	0.05	0.05-100	*<0.05*	*0.05-0.10*	*>0.10*
Strontium	µg/L	0.1	0.5	0.5-1000	*<0.5*	*0.50-5.0*	*>5.0*
Potassium	mg/L	0.25	0.50	0.50-100	*<0.50*	*0.50-0.25*	*>0.75*
Sodium	mg/L	0.10	0.25	0.25-200	*<0.25*	*0.25-0.50*	*>0.50*
Sulfur	SO_4 mg/L	0.30	0.75	0.75-500	*<0.75*	*0.75-1.5*	*>1.5*
Iron	mg/L	0.005	0.025	0.025-1.0	*<0.025*	*0.025-0.050*	*>0.050*
Silicon	mg/L	0.06	0.30	0.30-50	*<0.30*	*0.30-0.75*	*>0.75*
Aluminum	µg/L	10	50	50-10000	*<50*	*50-100*	*>100*

Appendix 10.5. Microstructural data of Transylvanian rock salt.

Table A.10.5.1. Calculated differential stress (MPa) and strain rates (s^{-1}) from Gelencsér *et al.* (2024b). The higher strain rate belongs to the solution precipitation creep in both rock types.

Rock type	**Differential stress (MPa)**	**Flow Laws**	
		Dislocation creep (s^{-1})	**Solution-precipitation creep (s^{-1})**
Layered salt	1.8	$5.1*10^{-12}$	$1.3*10^{-10}$
Massive salt	2.0	$8.8*10^{-12}$	$1.2*10^{-10}$

Appendix 10.6. The results of EMPA measurements

Table A.10.6.1. Major element composition of carbonate minerals of OGD-Öcsöd-K-2 cutting samples measured by electron microprobe analysis. Compositions are expressed in wt.%.

Point ID	FeO	MnO	MgO	CaO	$CO_{2corrected}$	Total
A1_001	0.75	0.17	0.24	55.49	43.35	100.00
A1_002	0.89	0.27	0.25	54.81	43.78	100.01
A1_003	0.87	0.28	0.26	55.15	43.44	100.01
A1_004	0.85	0.30	0.28	54.13	44.44	100.00
A1_005	0.78	0.26	0.24	54.73	43.98	100.00
A1_006	0.04	0.04	0.02	56.58	43.31	99.99
A1_007	0.54	0.16	0.15	54.98	44.17	100.00
A1_008	0.92	0.26	0.26	53.65	44.92	100.00
A1_009	0.91	0.25	0.23	54.90	43.71	100.01
A1_010	0.18	0.09	0.56	56.28	42.90	100.00
A1_011	0.07	0.00	0.38	57.91	41.64	100.00
A1_012	0.00	0.00	0.40	56.89	42.71	100.00
A2_001	1.02	0.25	0.33	54.28	44.11	100.00
A2_002	1.01	0.25	0.26	54.22	44.26	100.00
A2_003	1.01	0.31	0.26	54.66	43.77	100.00
A2_004	0.88	0.30	0.25	54.37	44.20	99.99
A2_005	0.91	0.26	0.25	54.88	43.70	100.00
A2_006	0.98	0.24	0.28	55.04	43.47	100.01
A2_007	0.90	0.34	0.27	54.28	44.20	100.00
A3_001	0.00	0.00	0.54	56.60	42.86	100.00
A3_002	0.91	0.25	0.29	42.21	56.34	100.01
A3_003	0.51	0.16	0.26	55.71	43.38	100.01
A3_004_c	7.78	0.65	10.81	29.51	51.24	99.99
A3_004_r	6.78	0.57	6.82	20.55	65.28	100.00
A3_005_c	7.83	0.75	11.60	32.19	47.63	100.00
A3_005_r	5.82	0.59	5.93	22.89	64.77	100.00
A4_001	1.72	0.38	0.89	53.24	43.77	100.00
A4_002	1.52	0.36	0.83	52.87	44.42	100.00
A4_003	0.95	0.04	0.38	55.17	43.46	100.00
A4_004	0.88	0.25	0.25	54.17	44.45	100.01
A4_005	0.56	0.06	0.29	55.94	43.15	100.00
A4_006	0.90	0.20	0.24	54.60	44.07	100.00
A4_007	0.02	0.04	0.46	57.03	42.45	100.00
A4_008	0.08	0.01	0.48	56.43	43.00	100.01
A4_009	1.11	0.11	0.28	47.06	51.44	100.00
A5_001	0.84	0.08	0.99	54.42	43.67	100.00
A5_002	0.97	0.24	0.30	54.70	43.79	100.00
A5_003	0.72	0.38	0.21	55.42	43.28	100.00
A5_004	0.06	0.04	0.13	56.88	42.90	100.00

Point ID	FeO	MnO	MgO	CaO	$CO_{2corrected}$	Total
A5_007	6.79	0.53	8.68	24.06	59.94	100.00
A5_008	1.24	0.08	0.99	53.63	44.06	100.00
A5_009	11.59	1.12	8.62	33.92	44.75	100.00
A5_010	0.02	0.02	0.44	57.18	42.35	100.01
A5_011	0.01	0.00	0.41	58.18	41.39	100.00
B1_001	0.86	0.22	0.27	55.29	43.36	100.00
B1_002	0.83	0.28	0.22	54.84	43.83	100.00
B1_003	0.87	0.22	0.29	54.89	43.73	100.00
B1_004	0.96	0.31	0.31	54.90	43.52	100.00
B1_005	0.97	0.19	0.29	54.93	43.62	100.00
B1_006	0.90	0.24	0.26	54.55	44.05	100.00
B1_007	0.87	0.20	0.23	54.52	44.18	100.00
B1_008	1.22	0.30	0.32	54.45	43.70	100.00
B1_009	1.00	0.21	0.27	55.10	43.41	100.00
B2_001	1.52	0.55	0.28	54.11	43.55	100.00
B2_002	1.17	0.46	0.30	43.79	54.28	99.99
B2_003	1.26	0.60	0.26	54.54	43.33	100.00
B2_004	1.30	0.45	0.25	52.24	45.75	99.99
B2_005	1.22	0.52	0.29	53.83	44.14	100.00
B2_006	0.83	0.14	0.26	55.00	43.76	100.00
B2_007	1.11	0.46	0.25	54.68	43.50	99.99
B2_008	1.27	0.41	0.31	52.92	45.09	100.00
B2_009	1.47	0.57	0.35	53.33	44.29	100.01
B2_010	1.25	0.59	0.29	44.26	53.59	99.99
B2_011	0.89	0.31	0.26	53.70	44.84	100.00
B2_012	1.31	0.56	0.29	49.36	48.49	100.01
B2_013	1.40	0.65	0.33	53.82	43.81	100.01
B2_014	0.91	0.06	0.37	54.78	43.87	99.99
B2_016	0.81	0.28	0.62	53.34	44.95	100.00
B2_017	1.00	0.25	0.83	53.90	44.02	100.00
B5_001	1.56	0.65	0.35	53.39	44.04	99.99
B5_003	1.57	0.56	0.38	53.49	44.01	100.01
B5_004	1.19	0.50	0.22	48.50	49.59	100.00
B5_005	1.38	0.65	0.36	53.85	43.76	100.00
B5_007	1.41	0.64	0.31	53.93	43.71	100.01
B5_008	1.48	0.58	0.31	53.78	43.86	100.00
B5_009	1.30	0.46	2.22	51.70	44.33	100.01
B5_010	2.18	0.53	0.47	51.53	45.28	99.99
B5_011	1.36	0.52	0.29	53.88	43.94	99.99
B5_012	1.32	0.52	0.29	53.76	44.11	100.00
B5_013	1.19	0.53	0.30	49.64	48.34	100.01
B5_015	1.51	0.52	0.50	43.05	54.42	100.00
B5_016	1.15	0.46	0.72	54.01	43.66	100.00

Point ID	FeO	MnO	MgO	CaO	$CO_{2corrected}$	Total
B5_018_r	0.30	0.07	2.31	52.41	44.91	100.00
B6_001	0.62	0.04	0.20	55.36	43.78	100.00
B6_002	0.00	0.04	0.52	57.05	42.39	100.01
B6_003	1.19	0.26	0.37	53.51	44.67	100.00
B6_004	0.52	0.15	0.09	55.71	43.52	100.00
B6_005	5.23	0.53	5.52	18.00	70.72	100.00
B6_006	10.34	1.26	9.38	33.90	45.12	100.00
B6_007	10.12	1.19	9.16	33.18	46.34	99.99
B6_008	0.56	0.20	0.24	55.71	43.29	100.00
B7_001	0.89	0.31	0.26	54.90	43.65	100.01
B7_002	0.71	0.25	0.21	55.41	43.42	100.00
B7_003	0.27	0.06	0.44	56.24	42.99	100.00
B7_004	0.25	0.09	0.56	55.84	43.26	100.00
B7_005	0.89	0.26	0.27	54.60	43.99	100.01
B7_006	0.90	0.30	0.24	54.88	43.68	100.00
B7_007	0.89	0.26	0.22	54.58	44.04	99.99
B7_008	11.46	0.79	8.85	34.32	44.58	100.00
B7_009	0.53	0.05	0.35	54.95	44.13	100.01
C7_001	3.00	0.30	8.27	29.38	59.06	100.01
C7_002	1.91	0.45	0.44	52.92	44.29	100.00
C7_003	12.25	1.10	7.99	33.76	44.91	100.01
C7_004	1.49	0.34	0.33	42.68	55.16	100.01
C7_006_c	1.68	0.43	0.42	53.27	44.20	100.00
C7_006_r	1.48	0.38	0.34	45.31	52.49	100.00
C7_007	1.80	0.46	0.49	52.97	44.27	99.99
C7_008	2.02	0.46	0.45	52.74	44.32	99.99
C7_009	1.82	0.47	0.46	50.25	47.00	100.00
E4_001	0.28	0.14	0.13	55.98	43.47	100.00
E4_002	1.23	0.41	0.28	53.37	44.71	100.00
E4_003	1.29	0.29	0.30	54.30	43.82	99.99
E4_004	1.15	0.29	0.25	54.71	43.60	100.00
E4_005	1.03	0.19	0.23	54.11	44.44	100.00
E4_006	0.06	0.00	0.17	57.59	42.18	100.00
E4_007	0.05	0.00	0.46	56.59	42.89	100.00
E4_008	1.29	0.32	0.25	54.06	44.08	100.00
E4_009	1.22	0.48	0.24	54.39	43.67	100.00
E4_010	1.18	0.36	0.26	53.17	45.03	99.99
F4_001	0.36	0.09	0.22	56.04	43.29	100.00
F4_003	0.91	0.30	0.29	54.66	43.83	100.00
F4_004	0.87	0.16	0.74	54.62	43.62	100.00
F4_005	1.04	0.22	0.43	53.81	44.50	100.00
F8_001	0.22	0.04	0.10	56.09	43.55	100.00
F8_002	1.44	0.35	0.33	54.01	43.87	100.00

Point ID	FeO	MnO	MgO	CaO	$CO_{2corrected}$	Total
F8_005	0.72	0.13	0.16	55.31	43.68	100.00
F8_006	0.58	0.04	0.28	55.25	43.84	100.00
F8_007	0.93	0.29	0.24	55.23	43.31	100.00
F8_008	0.76	0.24	0.21	54.97	43.82	100.00
F8_009	0.87	0.26	0.24	54.87	43.77	100.01
F8_010	0.91	0.27	0.26	54.13	44.43	100.00
F8_011	0.80	0.21	0.20	55.16	43.63	100.00
F8_012	0.87	0.29	0.25	53.44	45.15	100.00
F8_013	0.95	0.25	0.27	54.12	44.40	99.99
G6_001	0.92	0.21	0.28	54.43	44.16	100.00
G6_002	0.87	0.16	0.24	54.87	43.87	100.00
G6_003	1.00	0.20	0.27	54.73	43.81	100.00
G6_004	0.95	0.17	0.30	54.48	44.10	100.00
G6_005	0.84	0.26	0.23	54.99	43.69	100.00
G6_006	11.25	0.64	9.72	33.61	44.78	100.00
G6_007	7.88	0.76	10.76	34.44	46.16	100.00
G6_008	0.09	0.04	0.64	56.07	43.16	100.00
G6_009	0.16	0.05	0.53	56.00	43.26	100.00
G6_010	1.10	0.18	0.88	53.77	44.07	100.00
G6_011	0.04	0.04	0.71	55.47	43.74	100.00
G8_001	0.08	0.00	0.11	57.68	42.13	100.00
G8_002	0.89	0.14	0.40	54.80	43.77	100.00
G8_003	0.73	0.15	0.36	55.00	43.75	99.99
G8_004	1.36	0.37	0.40	53.91	43.95	99.99
G8_005	0.72	0.10	0.35	55.24	43.59	99.99
H5_001	0.80	0.14	0.42	55.28	43.35	100.00
H5_002	1.59	0.79	0.34	53.85	43.43	100.00
H5_003	1.29	0.63	0.29	53.87	43.92	100.00
H5_004	1.50	0.60	0.36	53.06	44.48	100.00
H5_005	2.35	0.71	6.29	44.47	46.18	100.00
H5_006	0.12	0.05	0.39	57.23	42.20	100.00
H5_007	1.79	0.81	0.41	52.32	44.67	100.00

Table A.10.6.2. Major element composition of feldspar minerals of OGD-Öcsöd-K-2 cutting samples measured by electron microprobe analysis. Compositions are expressed in wt.%.

Point ID	SiO_2	TiO_2	Al_2O_3	FeO	MnO	MgO	CaO	Na_2O	K_2O	Total
A4_001	65.46	0.02	18.87	0.05	0.00	0.00	0.02	0.35	17.03	101.81
A4_002	64.51	0.00	18.45	0.02	0.00	0.00	0.00	0.26	17.01	100.25
A4_003	64.18	0.01	18.50	0.03	0.01	0.01	0.01	0.21	17.10	100.07
A4_004	64.09	0.00	18.54	0.07	0.01	0.02	0.05	0.23	17.08	100.08
A4_005	64.51	0.03	18.53	0.02	0.00	0.00	0.01	0.22	17.27	100.58
A4_007	65.27	0.01	18.71	0.04	0.01	0.00	0.04	0.42	16.86	101.38
A4_009	64.31	0.00	18.56	0.02	0.00	0.00	0.01	0.21	16.97	100.07
A6_001	63.56	0.00	18.49	0.05	0.02	0.00	0.18	0.33	16.69	99.32
A6_002	64.97	0.01	18.70	0.03	0.03	0.00	0.02	0.35	16.81	100.92
B1_001	65.00	0.01	18.83	0.03	0.02	0.00	0.11	0.26	16.89	101.15
B1_004	65.22	0.00	18.78	0.03	0.01	0.00	0.10	0.28	17.10	101.52
B2_001	65.04	0.01	18.80	0.03	0.00	0.00	0.19	0.25	16.92	101.23
B2_002	65.41	0.00	19.04	0.03	0.00	0.00	0.15	0.30	16.89	101.83
B2_004	65.07	0.00	18.82	0.01	0.01	0.00	0.13	0.56	16.72	101.32
B2_006	64.52	0.00	18.50	0.20	0.00	0.01	0.16	0.27	16.71	100.38
B5_001	65.15	0.03	18.91	0.04	0.02	0.00	0.03	0.39	16.91	101.48
B5_002	65.12	0.00	18.98	0.05	0.00	0.02	0.07	0.48	16.84	101.55
B5_003	64.51	0.02	18.73	0.08	0.01	0.02	0.16	0.37	16.24	100.14
B5_005	64.16	0.04	18.71	0.07	0.00	0.02	0.13	0.83	15.92	99.87
B5_006	65.17	0.00	18.77	0.05	0.00	0.00	0.05	0.24	17.06	101.34
B5_007	65.00	0.01	18.98	0.05	0.02	0.00	0.09	0.23	16.99	101.36
B6_001	63.34	0.00	18.01	0.02	0.02	0.00	0.04	0.59	16.13	98.15
B6_002	63.39	0.01	18.36	0.03	0.00	0.00	0.04	0.53	16.56	98.92
C7_001	64.90	0.01	18.82	0.06	0.00	0.01	0.06	0.49	16.83	101.18
C7_002	64.64	0.00	18.79	0.07	0.03	0.00	0.07	0.41	16.83	100.84
C7_003	64.53	0.00	18.76	0.08	0.00	0.00	0.16	0.77	16.29	100.59
C7_004	64.59	0.00	18.83	0.10	0.02	0.00	0.08	0.63	16.18	100.44
C7_005	63.52	0.01	18.44	0.08	0.02	0.00	0.12	0.60	16.18	98.97
C7_006	64.48	0.01	18.88	0.09	0.03	0.00	0.08	0.73	16.11	100.40
C7_007	64.40	0.01	18.82	0.08	0.00	0.00	0.14	0.69	16.07	100.21
C7_008	63.96	0.00	18.63	0.07	0.00	0.01	0.18	0.44	16.32	99.61
F4_001	64.78	0.01	18.89	0.04	0.02	0.00	0.01	0.49	16.40	100.64
F4_002	65.02	0.01	18.93	0.03	0.02	0.00	0.00	0.42	16.65	101.08
F4_003	64.85	0.00	18.75	0.08	0.01	0.00	0.01	0.44	16.96	101.10
F4_004	64.83	0.00	18.82	0.02	0.02	0.00	0.03	0.46	16.76	100.94
F4_005	65.60	0.01	18.86	0.04	0.02	0.01	0.01	0.60	16.42	101.56
F4_006	65.28	0.00	18.94	0.03	0.02	0.00	0.04	0.32	16.97	101.60
H5_001	69.39	0.02	16.89	0.13	0.00	0.08	0.08	0.38	14.69	101.65

Appendix 10.7. Details of analytical programs used in EMPA measurements

Table A.10.7.1. Standards, spectrometers and analytical crystals used, and counting times on peak and background on each side of peak for alkali feldspar analyses.

Element	Spec.	Crystal	Standard	Peak (sec)	Background (sec)
Si	1	TAP	Anorthoclase (NMNH 133868)	30	15
Ti	2	PETJ	Hornblende (Kakanui) (NMNH 143965)	40	40
Al	1	TAP	Anorthite (NMNH 137041)	40	20
Fe	3	LIFH	Hornblende (Kakanui) (NMNH 143965)	40	20
Mn	3	LIFH	Bustamite (Astimex Standards Ltd.)	40	40
Mg	5	TAP	Hornblende (Kakanui) (NMNH 143965)	40	40
Ca	2	PETJ	Anorthite (NMNH 137041)	40	20
Na	5	TAP	Anorthoclase (NMNH 133868)	20	10
K	4	PETL	Microcline (NMNH 143966)	30	20

Table A.10.7.2. Standards, spectrometers and analytical crystals used, and counting times on peak and background on each side of peak for plagioclase analyses.

Element	Spec.	Crystal	Standard	Peak (sec)	Background (sec)
Si	1	TAP	Plagioclase (NMNH 115900)	40	20
Ti	2	PETJ	Hornblende (Kakanui) (NMNH 143965)	40	40
Al	1	TAP	Anorthite (NMNH 137041)	40	20
Fe	3	LIFH	Hornblende (Kakanui) (NMNH 143965)	40	20
Mn	3	LIFH	Bustamite (Astimex Standards Ltd.)	40	40
Mg	5	TAP	Hornblende (Kakanui) (NMNH 143965)	40	40
Ca	2	PETJ	Anorthite (NMNH 137041)	40	20
Na	5	TAP	Anorthoclase (NMNH 133868)	30	15
K	4	PETL	Microcline (NMNH 143966)	40	20

Table A.10.7.3. Standards, spectrometers and analytical crystals used, and counting times on peak and background on each side of peak for carbonate analyses.

Element	Spec	Crystal	Standard	Peak (sec)	Background (sec)
Fe	3	LIFH	Siderite (NMNH R2460)	40	40
Mn	4	LIFL	Bustamite (Astimex Standards Ltd.)	40	40
Mg	5	TAP	Dolomite (NMNH R10057)	40	40
Ca	2	PETJ	Calcite (NMNH 136321)	20	10